



HAL
open science

Colloidal nanocrystals for optoelectronic devices optically controlled at the nanometric scale

Mahima Chaudhary

► **To cite this version:**

Mahima Chaudhary. Colloidal nanocrystals for optoelectronic devices optically controlled at the nanometric scale. Micro and nanotechnologies/Microelectronics. Université Paris sciences et lettres, 2022. English. NNT: 2022UPSLS072 . tel-04317031

HAL Id: tel-04317031

<https://pastel.hal.science/tel-04317031>

Submitted on 1 Dec 2023

HAL is a multi-disciplinary open access archive for the deposit and dissemination of scientific research documents, whether they are published or not. The documents may come from teaching and research institutions in France or abroad, or from public or private research centers.

L'archive ouverte pluridisciplinaire **HAL**, est destinée au dépôt et à la diffusion de documents scientifiques de niveau recherche, publiés ou non, émanant des établissements d'enseignement et de recherche français ou étrangers, des laboratoires publics ou privés.



THÈSE DE DOCTORAT

DE L'UNIVERSITÉ PSL

Préparée à l'École supérieure de physique et de chimie
industrielles de la Ville de Paris (ESPCI Paris) UMR 8213-LPEM

**Nanocristaux colloïdaux pour dispositifs
optoélectroniques contrôlés optiquement à l'échelle
nanométrique**

**Colloidal nanocrystals for optoelectronic devices
optically controlled at the nanometric scale**

Soutenue par

Mahima CHAUDHARY

Le 1st December 2022

Ecole doctorale n° 397

**Physique et chimie des
matériaux**

Spécialité

**Physique et chimie des
matériaux**

Composition du jury :

Dr. Mr. Jérôme Tignon Professor, LPENS/PSL, France	<i>President</i>
Dr. Mme. Ni Zhao Professor, Chinese University of Hong Kong China	<i>Examineur</i>
Dr. Mr. Dinesh Kabra Professor, IIT Bombay, India	<i>Examineur</i>
Dr. Mr. Philippe lang CNRS Research Director	<i>Examineur</i>
Dr. Mr. George Deligeorgis Researcher, IESL - FORTH, Greece	<i>Rapporteur</i>
Dr. Mr. Zhenhua Sun Associate professor, Shenzhen University, China	<i>Rapporteur</i>
Dr. Mme. Charlotte Tripon-Canseliet Associate Professor, LPEM, ESPCI Paris	<i>Directrice de thèse</i>
Dr. Mme. Zhuoying Chen CNRS Researcher, LPEM, ESPCI Paris	<i>co-directrice de thèse</i>

“This thesis work is dedicated to my Grandfather”

Table Of Content

General introduction

Chapter I. Introduction

1.1	Introduction to photoresponsive nanoparticles	2
	1.1.1 Upconversion nanoparticles	2
	1.1.2 Carbon dots	11
1.2	State of art of optoelectronic device	23
	1.2.1. Microwave photoconductive switch	23
	1.2.2. Transistors	29
	1.2.3. Graphene based transistor	42
1.3	1.3 Objective of the thesis	52
1.4	References	53

Chapter 2. Experimental Methods and Characterizations

2.1	Graphene transfer mechanism	70
2.2	Deposition techniques	72
2.3	Characterization section	73
2.4	Device Measurement	82
2.5	References	84

Chapter 3. Synthesis and Nanoparticles

3.1	Introduction	86
3.2	Experimental section	86
	3.2.1 Method and Chemistry	86
	3.2.2. Synthesis of Nanoparticles NaYF ₄ :Er ³⁺	89
	3.2.3 Synthesis of carbon dots	91
	3.2.4 Summary	100
3.3	References	101

Chapter 4.	Colloidal upconversion nanocrystals enable low-temperature-grown GaAs photoconductive switch operating at $\lambda = 1.55 \mu\text{m}$	
4.1	Introduction	104
4.2	Experimental	106
4.3	Result and discussion	107
4.4	Conclusion	115
4.5	References	116
Chapter 5.	N-Doped Carbon Quantum Dots on Graphene for Field-Effect Transistor Optoelectronic Memories	
5.1	Introduction	120
5.2	Experimental	122
5.3	Result and discussion	124
5.4	Conclusion	133
5.5	References	134
Chapter 6.	General conclusion and perspectives	139
	Appendix	143

General Introduction

Due to their small size, high sensitivity, dependability, portability, and low cost, optically controlled semiconductor device applications have gained prominence in recent decades. There are two types of optoelectronic devices: light-sensitive devices and light-generating devices. Examples include photoswitches, phototransistors, light-sensitive resistors, and photovoltaic cells, among others. To operate efficiently throughout the entire process, the materials used for each step must be sensibly optimized. Numerous metal oxides or chalcogenides, such as "TiO₂, ZnO, Fe₂O₃, WO₃, Bi₂S₃, Sb₂S₃, CdS, and Cu₂ZnSnS₄" etc., have been investigated in the literature.

For optoelectronic applications of microwave photoconductive switches, there is a particular interest to innovative devices capable to operate in the SWIR spectrum. For this purpose, whether there exist suitable nanomaterial candidates which can provide trade-offs between the ease of fabrication and device properties, is still an ongoing open question. On the other hand, for optoelectronic memories based on field-effect transistors, continuous research efforts are needed to provide a better and longer memory capacity without increasing their lower energy consumption or augmenting fabrication costs. Towards the two above-mentioned applications, novel device solutions can be engineered by proposing innovative materials. In particular, colloidal semiconducting nanocrystals are advantageous due to their solution-processability, size-tunable spectral absorption, and compatibility with different substrates. The combination of colloidal nanomaterials with more conventional semiconductors can allow one to achieve hybrid devices that take advantages on both the high carrier mobility of conventional semiconducting materials and the tunability (from the synthesis) of the optical and electronic properties of colloidal nanocrystals.

The structure of my PhD thesis manuscript is organized as follows: In total, there will be six chapters presented. The focus of the first chapter is an introduction to the field of optoelectronic technologies, the current state-of-the-art, and the technological outlooks for some of the optoelectronic devices. Following that, the second chapter is devoted to present the experimental details used in this thesis. Instrumental information's used for the characterization and fabrication of materials and devices are described in this chapter. The third chapter focuses on colloidal synthesis. It contains the synthesis details and results on

the size-tunable solution-processed colloidal $\text{NaYF}_4:\text{Er}^{3+}$ nanocrystals and carbon quantum dots (CQDs). The fourth chapter presents the principal results of the microwave photoconductive switches on which I applied the upconverting $\text{NaYF}_4:\text{Er}^{3+}$ nanocrystals synthesized in chapter 3 in this thesis in order to enable a sensitivity to SWIR photons such as those with a wavelength of $1.5 \mu\text{m}$. The fifth chapter presents the principal results of the field-effect transistor (FET)-based optoelectronic memories where the CQDs synthesized in chapter 3 was applied.

Chapter 1: This section provides an overview of the two primary components of this thesis: (1) Colloidal nanocrystals and (2) Optoelectronic devices. Upconversion nanomaterials and CQDs, their optical properties, and their applications. In part (1), the colloidal synthesis for $\text{NaYF}_4:\text{Er}^{3+}$ nanocrystals and CQDs, and the state-of-the-art are described. In part (2), microwave photoconductive switches and optoelectronic memories are introduced. This is followed by a discussion of their figures of merit and the various physical parameters involved.

Chapter 2: This chapter describes the fabrication procedures for the two types of devices mentioned above as well as the characterization techniques used for these materials and devices. In addition, the procedure for thin-film deposition and the working principle of a few major characterization techniques used in this thesis, including XRD, SEM, TEM, PL, and UV-Vis spectrum, are presented.

Chapter 3: This chapter presents mainly colloidal synthesis and the results obtained. First, the synthesis methods and the results of the obtained upconverting $\text{NaYF}_4:\text{Er}^{3+}$ nanocrystals and Carbon Quantum Dots (CQDs) are described together with their optical properties. In particular, when excited by SWIR photons with a $\lambda = 1.5 \mu\text{m}$, the colloidal $\text{NaYF}_4:\text{Er}^{3+}$ nanocrystals exhibit a multi-peak fluorescence spectrum located in the visible spectrum. This upconversion optical property will be harnessed to fabricate SWIR-active photoconductive switches in chapter 4. For CQDs, different doping can be exercised from the synthesis. Under UV excitation, fluorescence in the visible spectrum can be obtained. The charge-trapping properties (associated with the doping conditions) will be harnessed for the fabrication of FET-based optoelectronic memories in chapter 5. Results in terms of

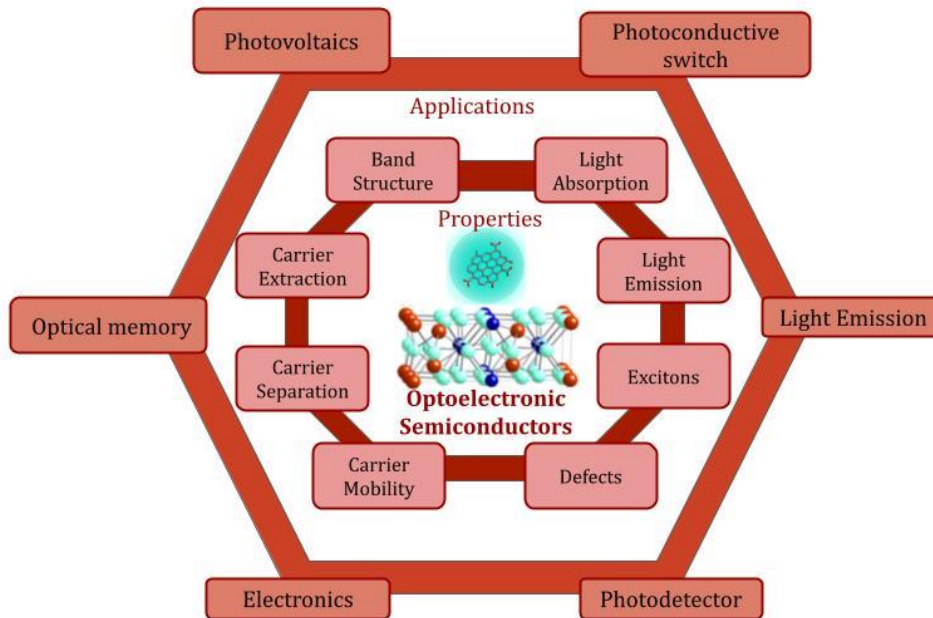
material characterizations, by techniques such as UV-Vis, XRD, PL, and Raman, are also presented in this chapter.

In Chapter 4, the synthesized upconversion nanocrystals ($\text{NaYF}_4:\text{Er}^{3+}$) are used in conjunction with the low-temperature-grown gallium arsenide (LT-GaAs) photoconductive switch to improve the ON/OFF ratio in the SWIR spectrum in order to obtain GHz-frequency signals. A hybrid nanocrystal/GaAs device was manufactured by depositing the nanocrystal solution directly onto a LT-GaAs device with a 1 μm gap between two electrodes. SEM measurements confirmed well that the existence of the nanocrystals inside the active area (the gap) of the device. A $\lambda = 1.55 \mu\text{m}$ laser light was applied when I compared the performance of the device with and without upconversion nanocrystals. At an input signal frequency of 20 MHz, the nanocrystal/LT-GaAs hybrid device exhibited a maximum ON/OFF ratio of 20.6 dB. Due to the upconversion energy transfer from the nanocrystals, the ON/OFF ratio of the hybrid nanocrystal/LT-GaAs device was measured to be more than twofold higher in decibel than that of the control device without upconversion nanoparticles.

Chapter 5 discusses how highly luminescent nanoparticles of carbon, one of most abundant elements, could be excellent candidates for optoelectronic memories. Here, for the first time, I fabricated functional UV-enable and visible-blind optoelectronic memories with multilevel writing capabilities by coupling a graphene FET and the unique charge-trapping and retention properties of nitrogen-doped (N-doped) CQDs. After UV-programming, prolonged charge retention of > 96% of its initial programmed photocurrent value can be obtained for a period of 10 hours and can be erased with a positive gate bias. Together with their simple colloidal synthesis, abundant nature, environmentally friendly compositions, and excellent memory functionalities, these fully carbon-based non-volatile optoelectronic memories offer promising prospects for the field's future development.

Chapter 1

Introduction



Resume

En raison de leur petite taille, de leur grande sensibilité, de leur fiabilité, de leur portabilité et de leur faible coût, les applications des dispositifs semi-conducteurs à commande optique ont gagné en importance au cours des dernières décennies. Il existe deux types de dispositifs optoélectroniques : les dispositifs sensibles à la lumière et les dispositifs générateurs de lumière. Parmi les exemples, citons les photocommutateurs, les phototransistors, les résistances sensibles à la lumière et les cellules photovoltaïques, entre autres. Pour fonctionner efficacement tout au long du processus, les matériaux utilisés à chaque étape doivent être judicieusement optimisés. De nombreux oxydes ou chalcogénures métalliques, tels que "TiO₂, ZnO, Fe₂O₃, WO₃, Bi₂S₃, Sb₂S₃, CdS, et Cu₂ZnSnS₄" etc. ont été étudiés dans la littérature.

Pour les applications optoélectroniques des commutateurs photoconducteurs à micro-ondes, il est particulièrement intéressant de disposer de dispositifs innovants capables de

fonctionner dans le spectre SWIR. À cette fin, la question de savoir s'il existe des nanomatériaux candidats appropriés qui peuvent offrir un compromis entre la facilité de fabrication et les propriétés du dispositif est toujours ouverte. D'autre part, pour les mémoires optoélectroniques basées sur des transistors à effet de champ, des efforts de recherche continus sont nécessaires pour fournir une meilleure et plus longue capacité de mémoire sans augmenter leur faible consommation d'énergie ou augmenter les coûts de fabrication. Pour les deux applications susmentionnées, de nouvelles solutions de dispositifs peuvent être conçues en proposant des matériaux innovants. En particulier, les nanocristaux semi-conducteurs colloïdaux sont avantageux en raison de leur facilité de mise en solution, de leur absorption spectrale réglable en taille et de leur compatibilité avec différents substrats. La combinaison de nanomatériaux colloïdaux avec des semi-conducteurs plus conventionnels peut permettre de réaliser des dispositifs hybrides qui tirent parti à la fois de la mobilité élevée des porteurs de charge des matériaux semi-conducteurs conventionnels et de la possibilité d'accorder (dès la synthèse) les propriétés optiques et électroniques des nanocristaux colloïdaux.

1.1 Introduction to Photoresponsive nanoparticles

1.1.1. Upconversion nanoparticles

1.1.1.1. Introduction

Upconversion nanocrystals (UCNPs) are fluorescent nanomaterials that use lanthanide (Ln-doping) to convert a near-infrared excitation into a variety of visible emissions with very distinct optical properties.¹ Due to their large anti-stokes shifts (up to 500 nm) that separate discrete emission peaks from infrared excitation, as well as their high photochemical stability and broad emission bandwidth, upconversion nanocrystals are used in a variety of applications. **Figure 1** depicts recent selective breakthroughs in the multifunctionalization of upconversion nanoparticles for novel applications. These applications are prevalent in a wide range of fields, including imaging, cancer therapy, volumetric displays, and photonic switching.²

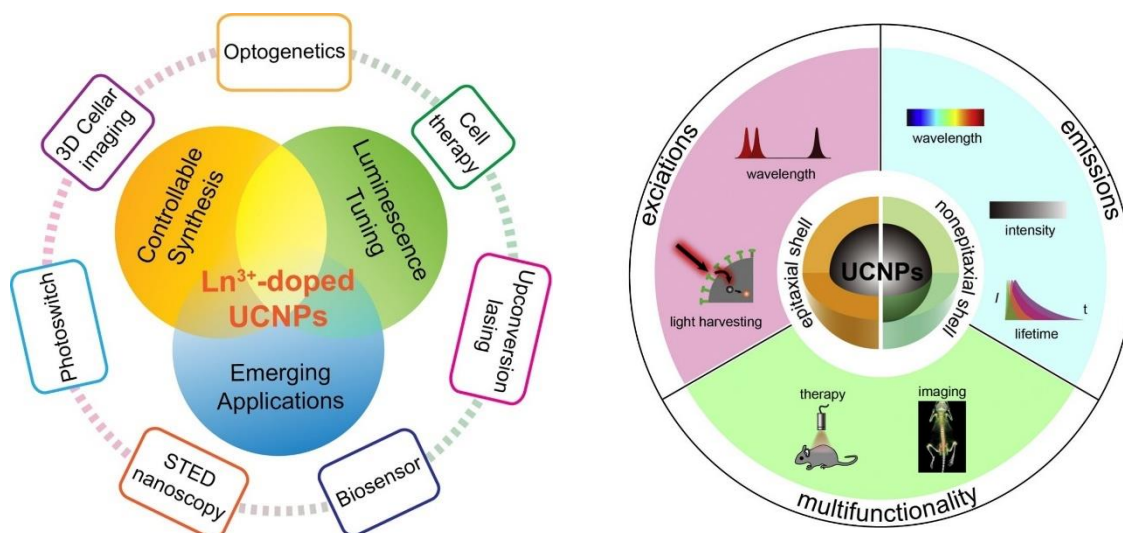


Figure 1: Recent advances in upconversion nanocrystals for emerging applications.^{3,4}

UCNPs in particular, can convert unutilized sub-bandgap NIR photons into visible photons for photovoltaic devices such as dye-sensitized solar cells (DSSCs) as shown in **figure 2**.⁵ Lanthanide-doped upconversion nanoparticles contribute to upconversion of nanocrystals from infrared band of 800 nm, 1000 nm, 1200 nm, and 1500 nm, respectively, because the rich metastable energy levels are formed by 4f electrons of rare-earth ions that contribute to upconversion process of Ln-doped nanocrystals⁶. Rare earth (RE) ions, particularly erbium (Er^{3+}) ions commonly used as UC luminescence activators. The luminescence of UCNPs was reported to improve with the doping of 2 kinds of ions, one of which is known as a sensitizer (absorb energy) and the other as an activator (emits energy as photon). Some other ions that show 10-time higher absorption cross-section at 980 nm than Er^{3+} is Ytterbium ions (Yb^{3+}). These best sensitizer-activator combinations are Yb^{3+} - Er^{3+} , Yb^{3+} - Ho^{3+} , Yb^{3+} - Tm^{3+} respectively⁷. These combinations can easily convert incident near infrared (NIR) radiations to visible radiations also specially with SWIR to visible using Er^{3+} shown in figure below. According to specific applications, host matrices are primarily investigated in order to provide high-efficiency UC luminescence.⁸

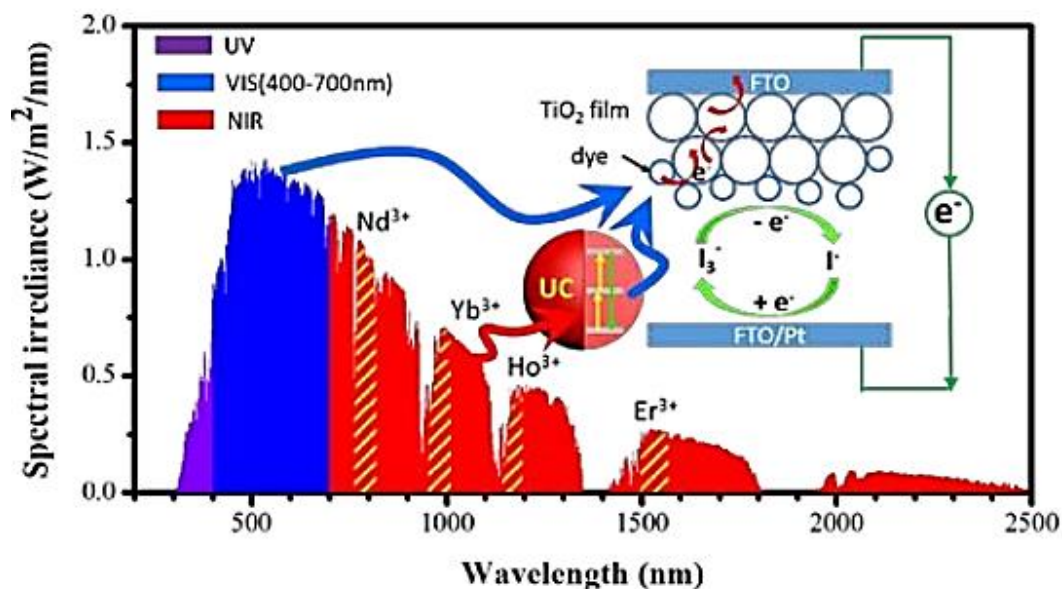


Figure 2: A image shows the harvesting of infrared sunlight (700-2500 nm) by upconverting it to visible light (400-700 nm).⁵

The efficiency of upconversion materials is generally determined by the following key parameters: (a) rare-earth ion concentration, (b) host lattice, and (c) surface-related quenching mechanisms. Where the energies (cm^{-1}) correspond to the highest energy lattice phonons for each halide as tabulated by Gamelin and Gudel.^{9,10} Halides, on other hand, are hygroscopic in nature, which limits their ability to be widely used in a variety of applications. Fluorides, on the other hand, are halides that are less sensitive to moisture than their bulk counterparts, when low phonon energy is responsible for the UC process. These characteristics make the RE doped fluorides host material appealing for UC applications. Many RE doped heavy fluorides, including LaF_3 , GdF_3 , YF_3 , SrF_3 , NaGdF_3 and other exhibit UC luminescence.⁸

Because of its high absorption properties and low phonon energy, NaYF_4 is considered the luminescent host material for UC in all RE fluorides. NaYF_4 has two stable lattice structures at room temperature: cubic phase and hexagonal phase.¹¹ Because the NaYF_4 crystalline lattice is multisite in nature, RE ions can comprise a variety of non-equivalent states in the crystalline lattice, limiting the efficiency of the UC process.¹² Dopant ions affect fluoride NC crystal nucleation, phase clarity, and UC efficiency.^{13,14}

1.1.1.2. Design and synthesis of lanthanide-doped upconversion nanoparticles

Till date, many syntheses technique have been developed in order to synthesize Ln^{3+} doped UC nanocrystals with controlled shape, size and structures using SEM technique shown in **table 1** and **figure 3**.

Synthesis strategy	HOST	Advantage & disadvantages
Hydro(solvo)thermal synthesis	$\text{Na}(\text{Y}, \text{Gd}, \text{Yb}, \text{Lu})\text{F}_4$, LiYF_4 , $\text{La}_2(\text{MoO}_4)_3$, $(\text{La}, \text{Y})_2\text{O}_3$, $(\text{La}, \text{Y}, \text{Gd}, \text{Lu})\text{F}_3$, $\text{Ba}(\text{Y}, \text{Gd})\text{F}_5$, BaY_2F_5 , Ba_2GdF_7 , $(\text{Ca}, \text{Sr})\text{F}_2$,	Formation of highly crystalline phases at much lower temperature. Excellent control over particle size and shape. Specialized autoclaves required. Impossibility of observing the crystal as it grows.
Coprecipitation	$\text{Na}(\text{La}, \text{Y}, \text{Gd}, \text{Yb}, \text{Lu}, \text{Sc}, \text{Tb})\text{F}_4$, $(\text{La}, \text{Y}, \text{Gd}, \text{Lu})\text{F}_3$, $\text{Li}(\text{Y}, \text{Gd}, \text{Yb}, \text{Lu})\text{F}_4$, $(\text{Ca}, \text{Sr})\text{F}_2$, BaYF_5 , GdOF , $(\text{La}, \text{Y}, \text{Yb}, \text{Lu})\text{PO}_4$, ZrO_2 ,	Simple and rapid preparation. Fast growth rate. Easy control of particle size and composition. Low product yield. Particle aggregation. Post-heat treatment typically needs.
Thermal decomposition	LaF_3 , $\text{Na}(\text{Y}, \text{Gd}, \text{Yb}, \text{Lu})\text{F}_4$, $\text{Li}(\text{Y}, \text{Lu})\text{F}_4$, $(\text{La}, \text{Y}, \text{Tb}, \text{Ho}, \text{Er}, \text{Tm}, \text{Yb}, \text{Lu})_2\text{O}_3$, $\text{Ba}(\text{Y}, \text{Gd}, \text{Lu})\text{F}_5$,	High quality, monodisperse nanocrystals. Rigorous and harsh synthesis condition. Hydrophobic resultants. Toxic by-products
Sol-gel	$(\text{La}, \text{Y})\text{F}_3$, CaF_2 , LaOF , $(\text{Y}, \text{Gd})_2\text{O}_3$, TiO_2 , ZnO , Ta_2O_5 , GeO_2 , Al_2O_3 , BaTiO_3 , LaPO_4 , $(\text{Gd}, \text{Lu})_3\text{Ga}_5\text{O}_{12}$, YVO_4 , ZrO_2 , Y_2SiO_5 , $\text{Y}_2\text{Ti}_2\text{O}_7$,	Simple and cost-effective accessories. Versatile. Better homogeneity. Less energy consumption. Cost of precursors. High-temperature

		post-heat treatment required.
Ionic liquid-based synthesis	Na (Y, Gd, Yb) F ₄ , (La, Y) F ₃ , CaF ₂ , BaMgF ₄ , etc.	Easy processing. Low solvent toxicity. Relatively expensive. Poorly biodegradable
Microwave-assisted synthesis	(La, Gd) F ₃ , Na (Y, Gd) F ₄ , CaF ₂ , BaYF ₅ , LaPO ₄ , (Ca, Sr, Ba) MoO ₄ , Ca (La, Gd) ₂ (MoO ₄) ₄ ,	Uniform heating. Rapid synthesis. Higher product yields. Specialized microwave reactor required.

Table 1: Typical synthetic strategies to lanthanide-doped upconversion nanocrystals.²

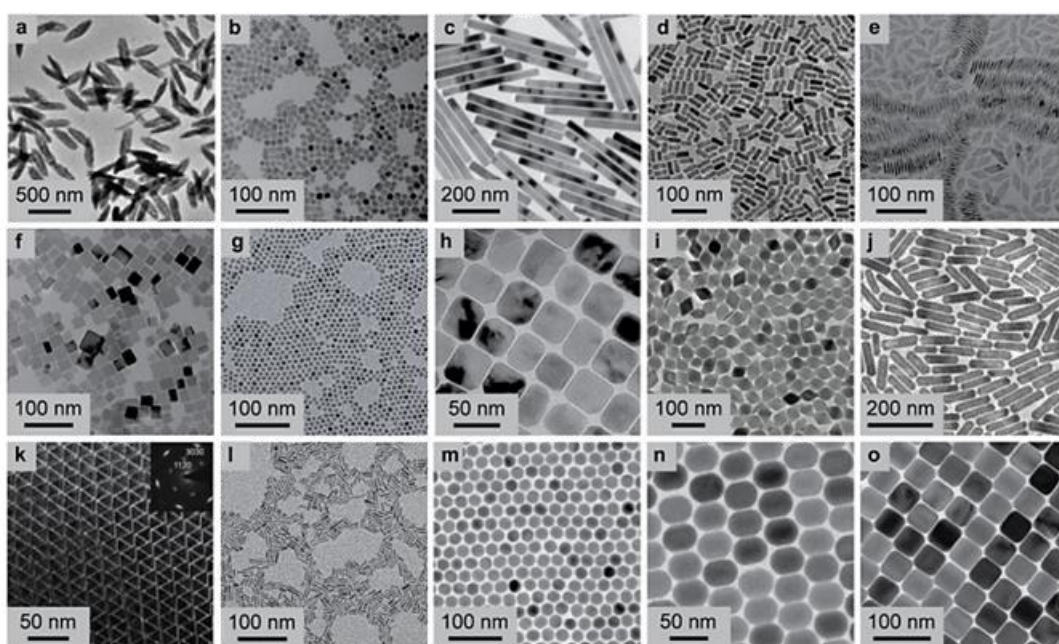


Figure 3: Illustration of Ln-doped TEM images of (a) YF₃, (b,c) NaYF₄ and (d) NaGdF₄ nanocrystals synthesis via hydro/solvothermal method. (e) GadF₃ via microwave irradiation method. (f) KMnF₃, (g) CaF₂, (h) NaScF₄, (i) LiYF₄ and KYb₂F₇ nanoparticles synthesis via coprecipitation method. (k) LaF₃, (l) SrF₂ and (m-o) NaYF₄ via thermal decomposition route.²

1.1.1.3. Rare earth doped fluoride materials:

Rare earth doped (RE) ions inorganic materials play a significant role in UC phenomenon, because compared to other hosts, halide-hosted phosphors have lower phonon energies. Lower phonon energies are important for reducing non-radiative (multiphonon) losses and

increasing metastable energy overall lifetime. Generally, phonon energies decrease across the halides of increasing atomic number i.e., shown in **figure 4**.

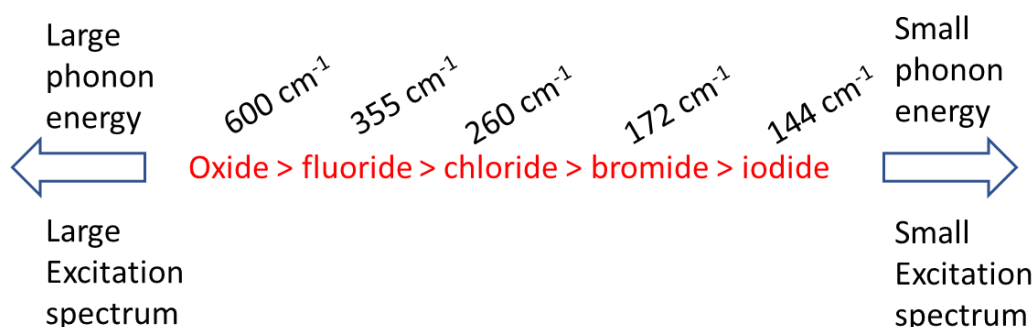


Figure 4: Schematic of different halides matrix used for UC process.¹⁰

1.1.1.4. Upconversion luminescence mechanisms

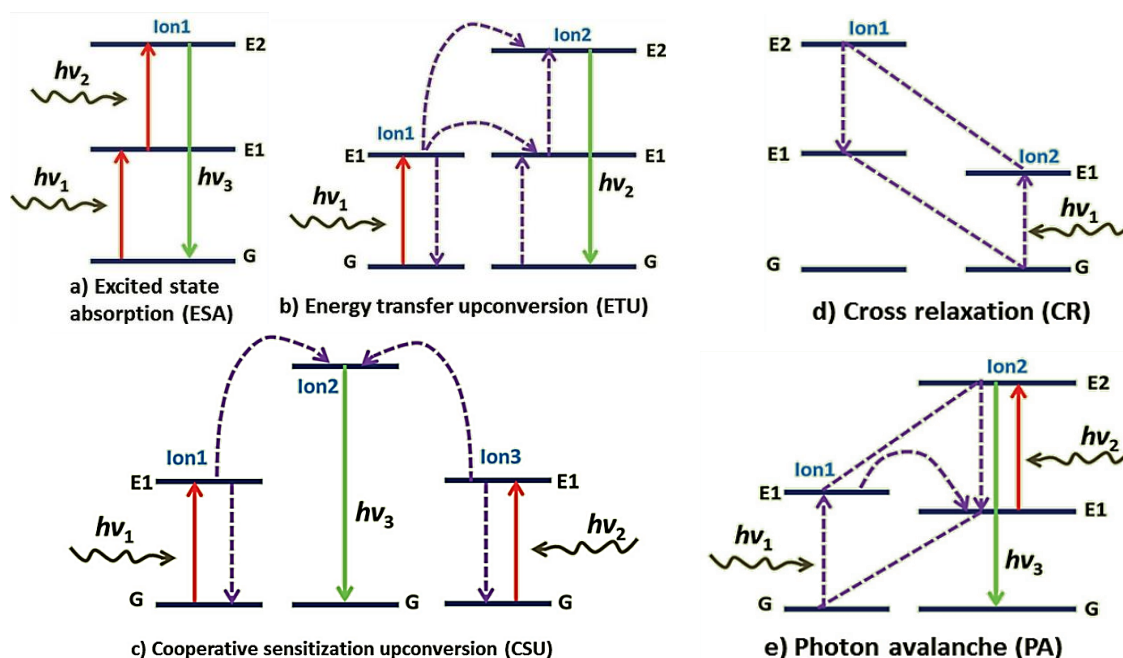


Figure 5: Principal UC process of Ln-doped UCNP, a) excited state absorption (ESA), b) energy transfer upconversion (ETU), c) cooperative sensitization upconversion (CSU), d) cross relaxation (CR), and e) photon avalanche (PA).¹⁵

Bloembergen *et al.*,¹⁶ first reported UC luminescence in 1959, using RE ions doped host materials as IR quantum counters. Around the 1960s,¹⁷ some primary research articles were published in conjunction with the development of laser systems that provide power density

and local confinement. These findings allow us to show that energy diffusion in these materials is based on energy transfer (ET) between identical ions. The following mechanisms (**Figure 5**) have received the most attention: (a) cooperative sensitization and (b) photon avalanche. Extensive research on UC mechanisms in glasses and inorganic crystals leads to an understanding of the complex interplay between various UC mechanisms.^{1,8,13,18}

1.1.1.5. Tuning of upconversion luminescence

Much attention has been paid to core/shell UCNPs that rely on separate lattices to harvest the more properties of UCNPs because their properties differ significantly from their bulk counterpart.¹⁹ The main reason for using a core/shell structure is to increase the intensity of the emission by shielding the host NPs in the center from non-radiative transitions caused by surface imperfections, as well as vibrational deexcitation caused by solvent particles and other functional groups absorbed at the surface of nanocrystals (NCs). When compared to core-only NPs, the intensity of UC luminescence from NaYF₄/NaYF₄:Yb³⁺/Er³⁺ core/shell nanostructures were increased 16 times.²⁰ This is due to the formation of external protective layers that shield Er³⁺ ions from water, reducing the toxic effect of water on luminescence. In any case, the main issue is that such NCs have a low emission and absorption efficiency. These types of problems can be solved by interacting the electromagnetic field and free electrons on the metal surface, which interact directly with the incident light, causing collective oscillations shown in **figure 6**. SPR is the abbreviation for the procedure (surface plasmonic resonance). It has also been discovered that the UC emission of core/shell NaYF₄:Yb³⁺/Er³⁺@SiO₂@Ag nanophosphors is approximately 14 times greater than that of NaYF₄:Yb³⁺/Er³⁺@SiO₂ core/shell nanophosphors.^{21,22}

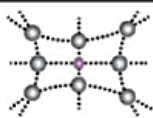
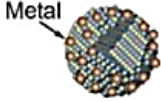
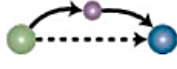
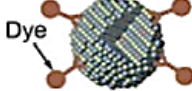
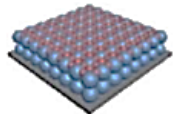
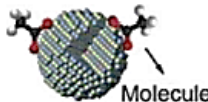
Strategy	Scheme
Host Lattice Manipulation	
Surface Passivation	
Surface Plasmon Coupling	
Energy Transfer Modulation	
Broadband Sensitization	
Photonic Crystal Engineering	
Inorganic-organic Hybrid	

Figure 6: Various strategies for enhancing/tuning photon upconversion in lanthanide-doped nanocrystals.²

1.1.1.6. Application

Bio-imaging, solar cells, optical thermometry, displays and anti-counterfeiting technologies, thermal photodetector, and photoconductive switch are all applications for upconversion materials. When these materials are synthesized as nanoparticles, their optical emissions are highly dependent on their size, providing new opportunities for innovation. Furthermore, achieving easily processable upconversion materials for direct applications or the fabrication of optoelectronic devices remains a challenge.

Optoelectronic Device Thermal Response: Using the size-dependent thermal properties of UCNPs, two approaches were considered: the first was to use AuNSs, which have a remarkable photothermal conversion efficiency due to the thermoplasmonic effect, and the

second was to use a conductive network of AgNWs, which can act as nanoheaters when a DC current was applied. These hybrid BHJ/UCNP photodetectors are emerging as a promising candidate for the next generation of low-cost, high-performance SWIR photodetectors due to numerous advantages such as solution-processability, flexibility, and non-toxicity, as well as fast processing speed and good photoresponsivity.²³

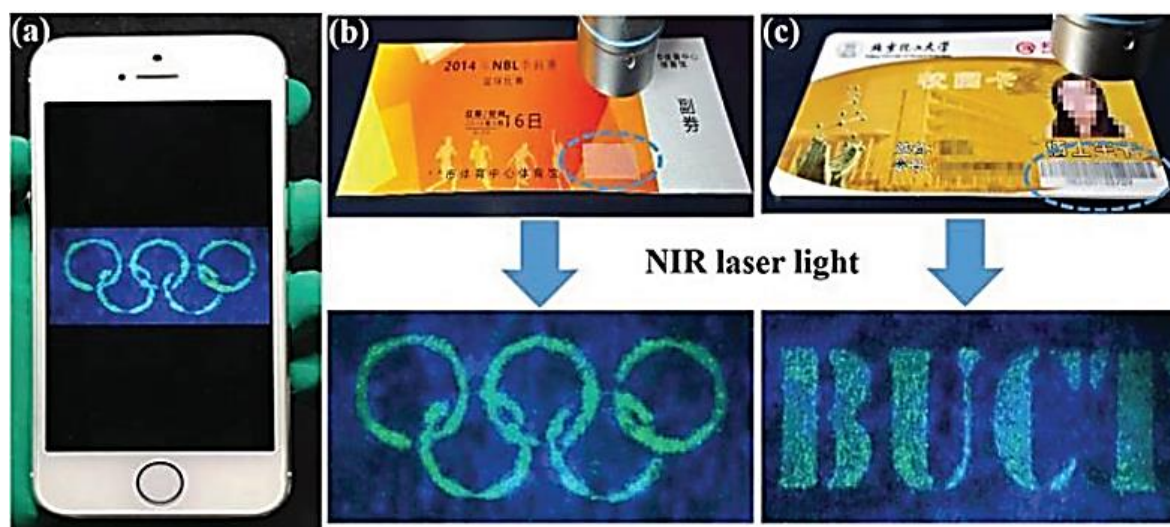


Figure 7: a) Pattern image identification with a portable apparatus consisting of a cell phone and a $\times 20$ objective; b) five interlocked rings; and c) “BUCT” letters of two-colored luminescence patterns images²⁴

Earlier Yan *et al.* in 2014¹² created a novel composite film using both β -NaYF₄:Yb³⁺, Er³⁺ upconversion inorganic nanocrystals and photochromic diarylethene organic species using simple “bottom-up” approach. This composite film is having rewritable optical storage capabilities. By using near IR light on UC nanoparticles create multilevel data storage flash memories. These photonic flash memories with UC have a high ON/OFF ratio, long retention time and excellent rewritability²⁵. Also, in Upconversion of modulated visible light for luminescence patterns in liquid crystal polymer networks nanoparticles for upconversion.

1.1.2 Carbon Dots

1.1.2.1. Introduction of Carbon Quantum dots

Carbon dots (CDs) are the rising star of the fluorescent nanomaterials world which were accidentally discovered in the mid-2000s²⁶ by Xu *et al.* during electrophoretic purification of single walled carbon nanotubes (SWCNTs) using the arc discharge method. CDs are typically less than 10 nm in size.²⁷ The core of CDs resembles a sphere and is created by stacking multiple graphene fragments in ordered and disordered forms; the second component is the distribution of numerous rich functional groups on the surface of CDs.^{28,29} Since then, luminous CDs have gotten a lot of attention because of their exceptional properties, as shown in **figure 8**. In reality, the potential of CDs is clear from the rapid growth of studies, which now number in the hundreds each year. In practice, the optical properties of CDs are similar to, if not competitive with, those of fluorescent semiconductor quantum dots (QDs).³⁰ Fluorescence CDs outperform semiconductor QDs in terms of water solubility and photobleaching resistance. Furthermore, they do not exhibit blinking effects, and also, they exhibit strong absorption in the blue and UV ranges, as a result of the on-going development of the synthesis processes continuous increase in the quantum yield (QY) is reported.

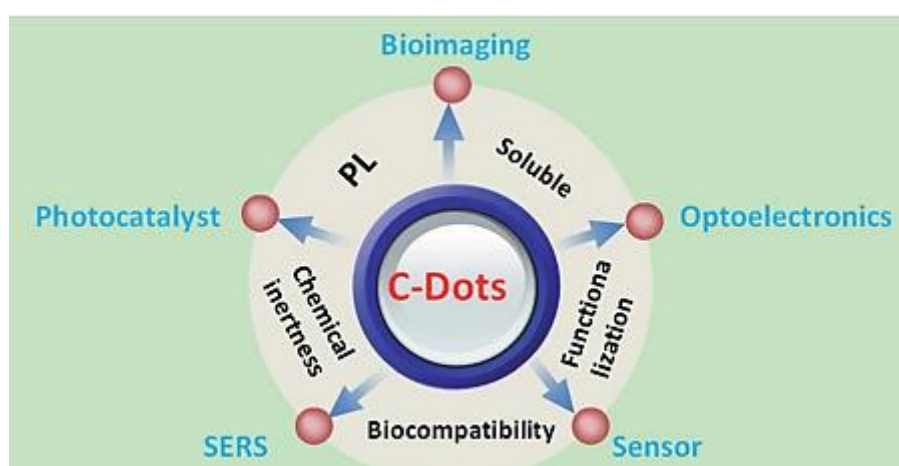


Figure 8: C-dots with unique properties have great potential applications in bioimaging, optoelectronics, sensor, SERS, and photocatalysis.^{31–33}

From a structural standpoint, CDs are a relatively diverse family of nanomaterials with a wide range of possible structures and optical properties. CDs have a generally quasi-

spherical morphology, and their structure can be graphitic, amorphous^{34,35}, or characterized by a C_3N_4 crystalline core.^{36,37} It can be visualized in graphene quantum dots, as previously stated. External agents³⁸ passivate the surface of CDs (during or after synthesis) by forming a layer of functional groups or molecules that bind to the carbonaceous core in all synthesis methods. The passivation layer, which can be a few nanometres thick in some cases, is an important part of the structure and function of CDs.³⁹ As a result, depending on the surface structure, CDs can be either hydrophilic or hydrophobic.⁴⁰ In terms of optical properties, different synthesis techniques produce CDs subtypes that can emit fluorescence at different wavelengths. CDs can thus emit blue,⁴¹ green, or red⁴² light, and their fluorescence can be either independent of excitation or "tunable," with the emission peak shifting continuously as a function of excitation wavelength.^{43,44} Their fluorescence intensities are sensitive to a variety of system interactions.

CDs are classified into several sub-types, each with its own core and surface structure, stoichiometry (C content ranging from 50% to 80%), and special optical properties. Small size (10nm) and a surface functionalization layer are two important characteristics for obtaining photoluminescence with high emission.⁴⁵ Several studies discovered that a passivating layer is important for photoluminescence, despite the fact that surface groups are not fluorescent on their own. Without regard for structural complexity, photoluminescence is the most intriguing and enigmatic feature of carbon dots. CDs are extremely powerful, tunable, and sensitive to local environmental factors such as solvents, ions, and pH.⁴⁶ In fact, when metal cations (Hg^{2+} , Cu^{2+} , Fe^{3+} , Ag^+) are present, their fluorescence can be quenched or strongly increased depending on the structure of the CDs.⁴⁷

Thousands of studies on carbon dots have been published, but research is still in its early stages. A number of scientific questions remain unanswered about carbon dots' optical behaviour, the nature of their electronic states in general, the main factors that determine their bright fluorescence, and the relationship between emission and structure.^{35,48-50}

1.1.2.2. Synthesis of CDs



Figure 9: shows a proposed synthesis procedure for preparing carbon dots.^{51,52}

The literature has documented a variety of ways to make CDs. Top-down and bottom-up approaches are the two families into which they are traditionally divided as shown in (**Figure 9**).

Top-down techniques involve the breakdown of nanomaterials or bulk carbon precursors with higher dimensions than CDs (which are considered zero-dimensional), such as carbon nanotubes or graphite (in bulk) (1D material). Bottom-up techniques rely on the carbonization of various chemical precursors, such as citric acid⁵³ or sucrose. Bottom-up synthesis typically involves the carbonization (to varying degrees) of various chemical precursors such as citric acid or sucrose. These compounds, which are frequently chosen due to their low melting points, can be carbonized at relatively low temperatures to produce CDs, the properties of which are greatly influenced by the reaction conditions. In addition to "pure" carbon-core CDs, the structure of CDs can be doped with nitrogen, sulphur, or other heteroatoms by combining the carbon sources with other chemical precursors such as urea⁵⁴ and thiourea. One significant advantage of top-down synthesis methods is that the resulting CDs typically have simple, well-defined structures (such as graphitic nanospheres) that eliminate structural ambiguity. Bottom-up approaches, on the other hand, can be far more difficult to manage: many additional products (such as tiny fluorescent compounds) can occur alongside CDs, necessitating careful purification after synthesis. Bottom-up synthesis techniques, on the other hand, have their own advantages. On the one hand, they are quite simple, and surface passivation is typically accomplished

without the need for post-synthesis chemical processing, using a "one pot." Aside from these benefits, bottom-up approaches are more adaptable and provide a wider range of CD structures, particularly when combined with doping techniques.⁵⁵

1.1.2.3. Physical and chemical properties

Structure and composition: CDs are quasi-spherical carbon nanoparticles that are typically less than 10 nm in diameter, whereas GQDs have lateral dimensions that are similar to single- or few-layered graphene a few nanometres, despite the fact that the largest measurement ever made is approximately 60 nm.⁵⁶ The shape of CDs is consistently identified using transmission electron microscopy (TEM)(a) and atomic force microscopy (AFM) (b), as shown in **figure 10**.

figure 10 shows X-ray diffraction (XRD) patterns (c), Raman spectroscopy (d), are used to determine the crystalline structure of CDs (HRTEM). CDs may have a broad XRD peak due to highly disordered carbon atoms, as opposed to graphene's sharp peak. There are two large peaks on the Raman spectra of the CDs at around 1300 cm^{-1} and 1580 cm^{-1} that are attributable to the disordered D band associated with sp^3 defects and the crystalline G band verifying the sp^2 carbon's in-plane vibration, respectively. When determining the degree of graphitization and crystallization for the inner of CDs, the relative intensity (I_D/I_G) of the characteristic bands for the CDs that are correlated to the in-plane crystal domain size is frequently used.⁵⁰

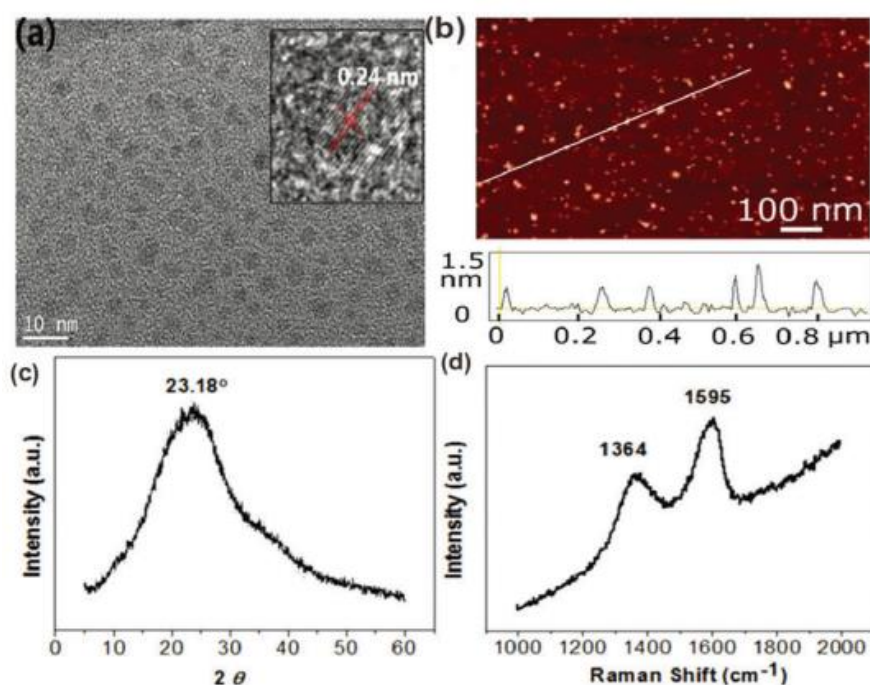


Figure 10: Structure characterization of CDs. (a) TEM and HRTEM (inset) (b) AFM image and height distribution (c) XRD (d) Raman.⁵⁷

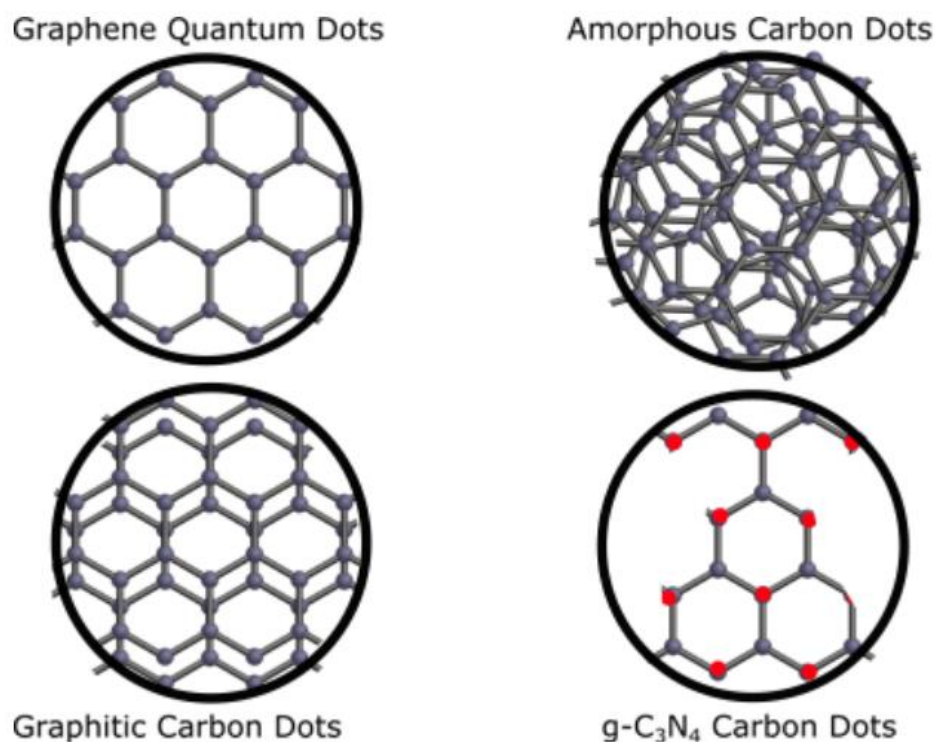


Figure 11: shows a schematic depiction of frequently mentioned CD architectures. Atoms of carbon and nitrogen are depicted by black and red dots.⁵⁸

Due to the presence of carboxylic acid moieties, carbon dots composed of few elements such as C, H, and O which promise greater solubility and further functionalization with other species. Heteroatoms introduce a variety of CD compositions and tune the conduction/valence band position. The technique of doping is used to alter the composition of CDs, which confers unexpected functions can be seen in **figure 11**.

1.1.2.4. Optical properties

Figure 12 shows some optical properties in following:

(a) Absorption: Due to the p-p* transition of the CQC bonds, which has a tail that extends into the visible range, CDs frequently exhibit strong optical absorption in the UV region (260-320nm).⁵⁹ Notably, the wavelength of absorption increases with the wavelength of emission, indicating red shift due to doping and surface passivation, which is a common

phenomenon for multi-emission CDs. A strong emission is typically caused by posterior absorptions trapping excited-state energy by the surface states.

(b) Photoluminescence: PL emission from CDs that includes excitation-dependent and excitation-independent PL and is caused by core-related and surface-state emissions.^{60,61} The maximum emission band, which has a higher Stokes shift and a narrow full width half maximum, is mirror symmetric to the maximum excitation band, indicating a weak self-absorption effect and low energy loss.⁶² QY is an important metric for describing the PL of CDs. Because the QY of naked CDs is frequently quite low, numerous fundamental studies have been conducted to increase the QYs, including modifying reaction conditions and procedures,⁶³ to metal-enhanced fluorescence⁶⁴ and element doping, including surface modification and passivation.⁶⁵ Yang *et al.* also improved the fluorescence of GQDs by reducing hydrazine hydrate.⁶⁶ As a result, a large number of CDs with a high QY of 83% have been manufactured. CDs have a significant advantage over traditional organic and inorganic fluorophores in terms of non-blinking PL and excellent photostability. Furthermore, the CDs PL intensity remains constant after several hours of continuous excitation with a Xe lamp. Organic fluorophores, on the other hand, photo bleach quickly.

(c) Up-conversion Photoluminescence: UCPL refers to the multiphoton activation process (**figure 13**), in which the simultaneous absorption of two or more photons results in the emission of light at shorter wavelength than the excitation wavelength. UCPL property of CDs opens new possibilities for different applications like cell imaging as well as highly efficient catalyst design for bioscience and energy applications.

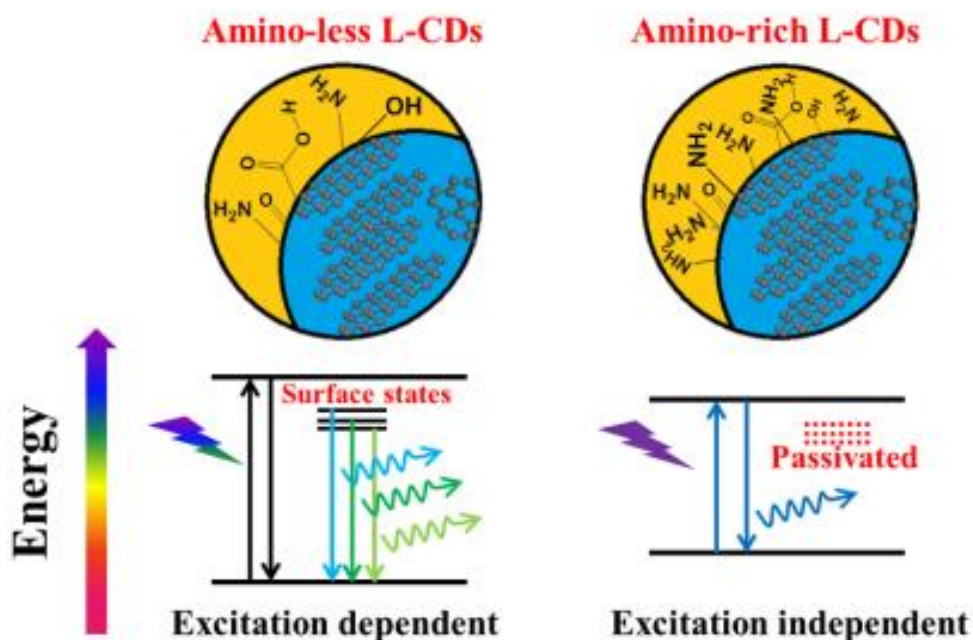


Figure 12: fabrication and its fluorescence mechanism⁶⁷ L-CDs (luminescent CDs)

(d) Quantum confinement effect: When a semiconductor crystal is nanometre in size, the crystal boundary has a significant influence on the electron distribution, which exhibits bandgap and size-dependent energy relaxation dynamics.⁶⁸ This phenomenon is known as the quantum confinement effect, and it has been studied in many semiconductor materials. Lin's group created three types of CDs with UV-excited red, green, and blue (RGB) fluorescence. These three types of CDs have similar chemical compositions, but their particle size distributions differ. As a result, the quantum confinement effect is thought to be responsible for changes in the fluorescence emission of these CDs.⁶⁹

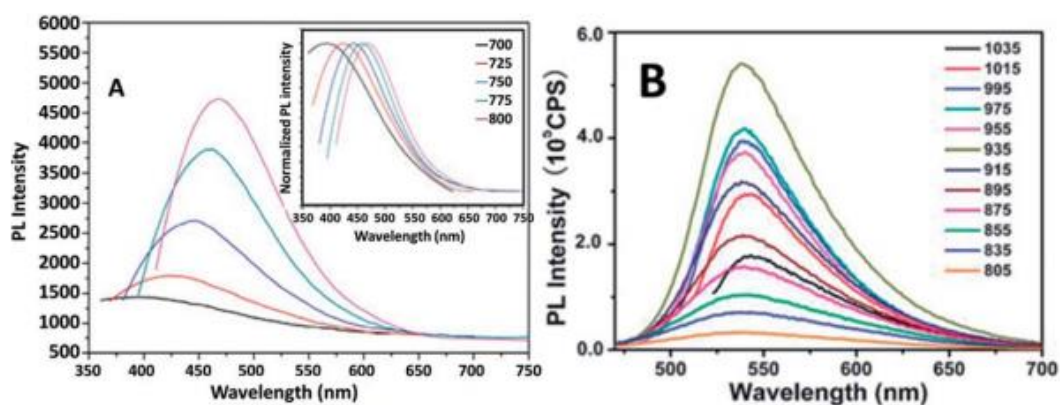


Figure 13: (A) UCPL spectra of the CQDs dispersed in water at excitation wavelengths progressively increasing from 700 nm in 25 nm increments. Inset: the corresponding normalized PL spectra. (B) UCPL properties of CQDs dispersed in water at excitation wavelengths from 805 nm to 1035 nm.⁷⁰

(e) Luminescence mechanism: "What is the source of the luminescence?" has always been a difficult question to answer. The problem that we must address is the difficulty in accurately describing and evaluating the overall picture of the PL mechanism for a variety of CDs. Many patterns have been proposed up to this point, including the radioactive recombination nature of excitations, surface passivation/defect, and quantum mechanics heteroatom doping, size effect, surface state effect, and state effects in the carbon-core and edge states. Nonetheless, surface functional groups, surface oxidation levels, quantum sizes/Conjugated sp² domain effect, and element doping are common reasons for CDs' tunable and long-wavelength emission shown in **figure 14**.⁵⁰

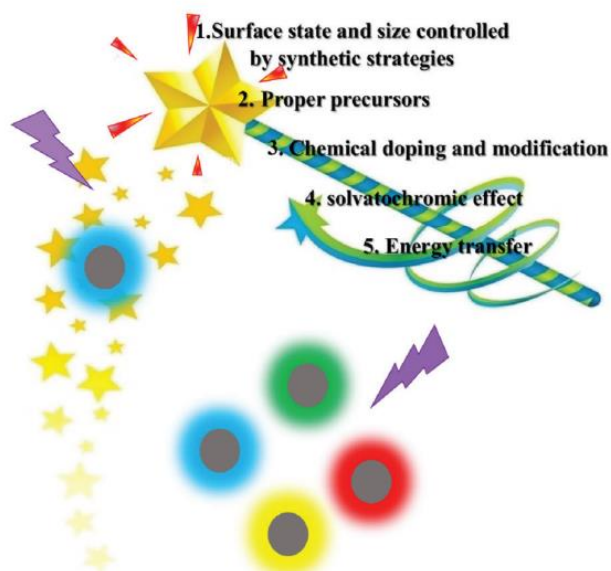


Figure 14: An example of a technique for achieving the long-wavelength and multicolour emission of CDs.⁷¹

There are several approaches for luminescence, long-wavelength, and multicolor CD emission: Previous studies on CDs show wonderful emission only in the blue-light region; however, this region's emission is significantly interfered by the common blue

autofluorescence of biological matrices, and there is photo-damage to biological tissues under ultraviolet light.⁷¹ As a result, their additional practical applications are limited to biologically relevant fields and other optical fields that require light harvesting at different wavelengths. Otherwise, the PL mechanism of CDs remains unknown, making it extremely difficult to control CD fluorescence due to a variety of ingredients and methods used to create CDs, and the resulting CDs included complex structure and parts. As a result, developing a comprehensive hypothesis based on current literary works is difficult. To investigate the source of full-color emissions and illuminate the mechanism of CDs' PL, multicolor CDs must be prepared under controlled and comparable conditions.

1.1.2.5. Surface state, size controlled and quantum confinement by synthetic strategies

To broaden the scope of applications and investigate the origin of CD fluorescence, researchers have committed to developing CDs with long-wavelength and tunable emission by improving reaction conditions or implementing separation technologies. Qu *et al.* 2014 described a new method based on the Maillard reaction between serial amino acid analogues and saccharides, which provided a superior methodology that could be easily scaled to high yields. As a result,¹⁷ distinct CDs with excellent amphiphilic properties were obtained. As-prepared CDs with properties and QY of up to 70.1% CDs derived from tryptophan, leucine, and aspartic acid are among them. Acid was used as a blue, green, and yellow emitter. The multicolor factors as shown in **figure 15** relating to shape and composition should come from the various sizes.⁷²

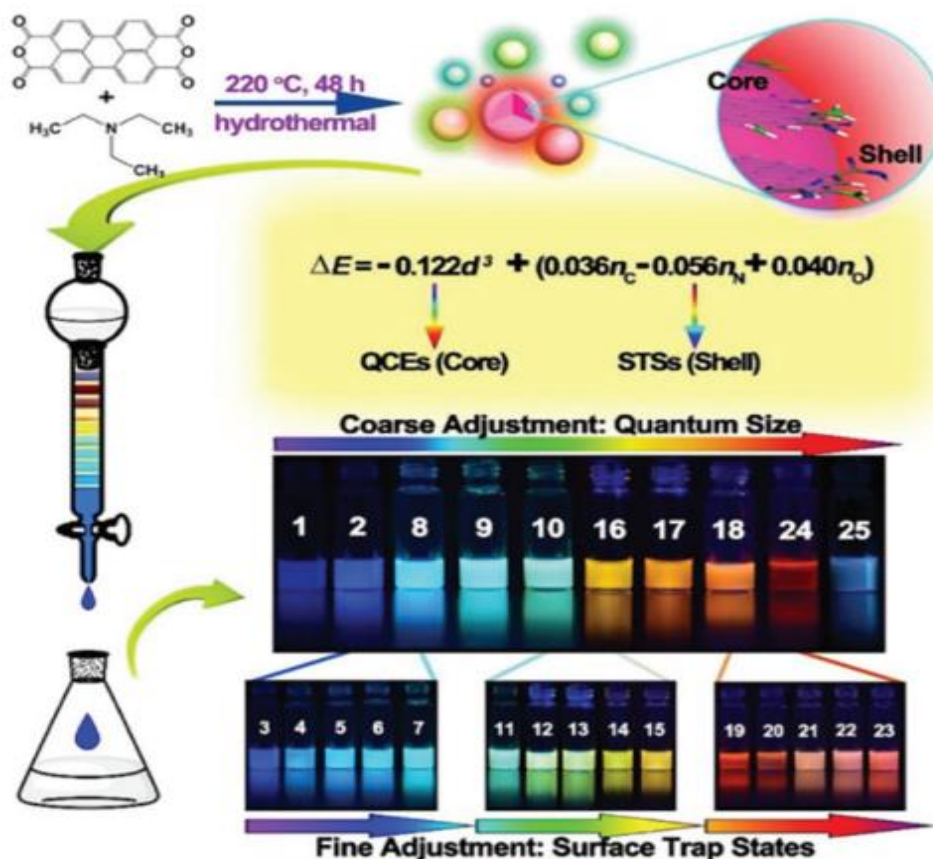


Figure 15: According to the inserted equation and photos, the size of the crystalline core in the core-shell nanostructured fluorescent CQDs plays the most important role due to the quantum confinement effect, while the functional groups of the shell play a secondary role in the adjustment of the fluorescence wavelength due to surface trap states (color).⁷³

1.1.2.5.1. Proper precursors

As we all know, the synthesis of carbon materials on the basis of well-defined molecular precursors is a highly effective approach because well-defined molecular precursors could afford functional carbonaceous materials through the inheritance of features from ingredients with controllable surface chemistry, surface topology, microcosmic morphology, and microstructure, endowing the carbon materials with special properties and broadening the scope of their possible applications. CA is a common organic precursor used in the bottom-up method of producing CDs, with abundant carboxyl groups that aid in dehydration and carbonization as a carbon source. CDs made solely from CA have low

luminescence, so another source must be used to produce CDs with good emission and special properties. As shown in **table 3** below.

Carbon Source	Nitrogen Source	QY	Application
Citric acid	Ethylenediamine	80.6%	Ink, Fe ³⁺ detection, CD/polymer composites
	Ethylamine	8.4%	–
	n-heptylamine	7.7%	–
	Urea	19.4%	–
Sodium citrate	Ethylenediamine	21.6%	–
Citric acid	Ethylenediamine	53%	–
	Hexamethylenetetramine	17%	–
	Triethanolamine	7%	–
Citric acid	Ethylenediamine	69.3%	Bioimaging
	Diethylenetriamine	68%	Bioimaging
	Triethylenetetraamine	33.4%	Bioimaging
Citric acid	Urea	36%	Drug delivery
Acrylic acid	Ethylenediamine	30.5%	Fluorescent polymers
p-phenylenediamine	Urea	up to 35%	Bioimaging
Calcium citrate	Urea	10.1%	Ink
Citric acid	Ethylenediamine	1.7%	–

Table 3: Small molecule dual precursors for carbon dot (CD) synthesis. QY: quantum yield.⁷⁴

1.1.2.5.2. Chemical doping and modification

Doping CDs (**figure 16**) with heteroatoms or inorganic salts has recently proven to be an effective method for tuning the electronic density, modulating the electronic structure, and then their intrinsic performance properties, resulting in unexpected phenomena and characteristics.⁷⁵ During or after synthesis, various chemical groups, such as diamine, hydrazide, thiol, and alkynyl, have been attached to the surface of CDs. Edge-terminated polymer is one of these. Similar to PEG, BPEI, amine is frequently used for chemical modification to improve surface passivation and prevent non-radiative recombination.⁷⁶

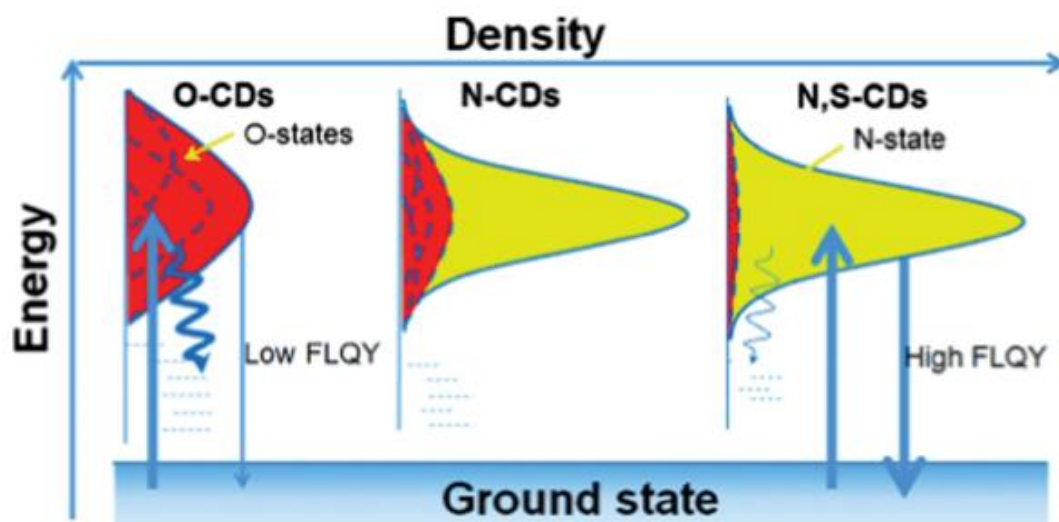


Figure 16: illustration of the fluorescence mechanism for O-CDs, N-CDs, and N, S-CDs.⁷⁷

1.1.2.5.3. Solvatochromic effects

The solvatochromic effect describes how the color of a substance changes with the polarity of the solvent, which is common for metal nanoparticles and is caused by optical properties such as surface plasmons.⁷⁸ As shown in **figure 17**, Zboril *et al.* 2013 and colleagues demonstrated a new class of CDs derived from cationic surfactants with amphiphilicity and tunable PL depending on the polarity of the solvent, from blue to green to yellow.

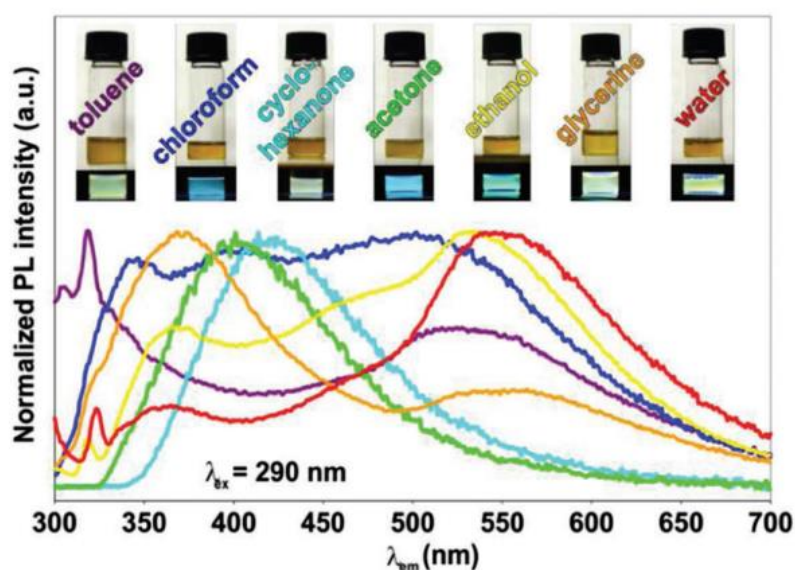


Figure 17: Effect of different solvents on the fluorescence of GQDs.⁷⁹

1.1.2.5.4. Energy transfer

Long-wavelength emission can be observed indirectly via an energy transfer mechanism in which CDs serve as a good energy donor and an energy acceptor is attached to the CDs for energy acceptance over a short distance and with higher efficiency. The donor spectrum's emission must effectively overlap with the acceptor's absorbance. Spectrum is a prerequisite for efficient energy transfer. In the energy transfer system, the energy acceptor always emits at a long wavelength and is used in sensing systems for bio-analysis with high selectivity. Wu *et al.* 2013 conjugated CDs with naphthalimide-azide, which when reduced by H₂S could transform into an energy acceptor (naphthalimide-amine), and thus a FRET-based ratiometric sensor for detecting H₂S was created.⁸⁰ There are numerous challenges and opportunities in the fabrication of energy transfer systems because there are many undiscovered fantastic functional molecules and luminescent materials, such as rare-earth metals-based materials, that can be used as energy acceptors/donors.⁸¹

1.2. State of Art of optoelectronic device

1.2.1. Microwave Photoconductive switch

1.2.1.1. Introduction

Modern wireless circuits and system rely heavily on microwave switches. As microwave photonic devices gain popularity and enabling technologies for future microwave circuits and subsystems, several designs of optically controlled switches have recently been proposed. The search of microwave switches began in 1970s⁸² and still going on today. In the literature devices made from coplanar waveguides and microstrip transmission lines printed on silicon substrate has been reported. The basic microwave switch was used in the designs of Antennas, filters, phase shifters and couplers are example of passive device components. The primary advantage of optically controlled microwave circuits is their high efficiency and the degree of separation between the controlling electronic circuits and the microwave circuit. The highly resistive silicon wafer in these devices is typically illuminated by near-infrared laser or a laser diode having optical power of several hundred milliwatts. Reconfigurable antennas and cryogenic components have proven to be ideal for the

implementation of silicon switches. The primary advantage of antenna design is the removal of biasing lines that can interrupt with the operation of the antenna.⁸³

One disadvantage of photoconductive switches has been their isolation, which cannot always match that of RF MEMS switches. The majority of switch applications in mobile and wireless communication system necessitate for both low insertion loss and excellent isolation performance.

A Photoconductive switch is an electrical switch that is based on material's photoconductivity, or an increase in conductance as a result of light irradiation. In almost all the cases, semiconductor materials are used, where absorbed light (having photon energy above band gap energy) generate free carriers, which contribute to conductivity. Semiconductor materials used frequently are low-temperature grown gallium arsenide (LT-GaAs)⁸⁴, Chromium-doped gallium arsenide (Cr-GaAs), indium phosphide, amorphous silicon etc. are common materials. In order to reduce the switch's recovery time (i.e., photoexcited carrier lifetime)⁸⁵, low-temperature grown or some doping for example chromium in GaAs, or ion bombardment for producing crystal defects are commonly used. Apart from time of recovery, the bandgap energy, dark resistivity, and electrical breakdown are all important criteria.

Photoconductive switch made with different designs like:

- Bulk devices a few millimeters or centimeters long with electrical contacts on the end faces used to switch extremely high voltages (several times above 100 kV).⁵
- Microstrip devices with a small gap; the gap can be straight or interdigitated, with a width ranging from a few microns to tens of microns; for high-speed, low-power applications.
- For high-speed sliding contact devices that illuminate the point between two parallel strips of a coplanar stripline.

A photoconductive switch is used in a variety of applications, including:

- For photoconductive sampling, particularly in the testing of high-speed integrated electronic devices (because electrical contacts are required for DC and low-frequency signals even before dicing).

- For the generation of terahertz pulses.
- In both continuous-wave and pulsed modes, direct DC to RF conversion is used to generate microwave and millimeter waves (e.g., with a frozen waveform generator).
- As high-speed photodetectors in optical fiber communication.
- In high-performance analog-to-digital converters.

The microwave photoconductive switch operates in the RF or microwave range, and the device is used to route high frequency signals through transmission paths. The switch operates at communication wavelengths of 1.3 and 1.55 μm .

1.2.1.2. Working principle of microwave PCS

A photoconductive switch is made up of a small piece of semiconductor crystal (Like LT-GaAs) and two planar metal electrode and two ground planes with a specific geometric design is that of an antenna, which can support a large electric field across its surface. Then Continuous light wave is focused at short wave infrared wavelength onto the gap between the electrodes (Typically laser with wavelength of 1.3 to 1.5 μm) shown in **figure 19**. So, the operation of such devices is based on the change in electrical conductance caused by illumination, such as the generation of electron-holes in semiconductors as a result of above-bandgap photoexcitation is distinguished by a photoconductance G_g is the equivalent of a photoresistance R_g is produced at the level of the illuminated area., which contributes to the increased conductivity. Also, the generation of electron-hole pairs, resulting in a rapid change in current density. A microwave signals (in GHz) is generated which is depends on the frequency distribution, design and carrier dynamics.

The equivalent circuit model of the active region (the region between the gap) of photoconductive switches has been reported previously^{86,87} and in **figure 18** in similar way as microwave has high pass filter. According to this model the active region is dominated by gap conductance (G_g) and gap capacitance (C_g) connected in parallel, whose value depends on the illumination intensity and wavelength. They are also linked in series with the two circuits in which the shunt conductance (G_s) and shunt capacitance (C_s), Both connected with the region outside the gap, which connected in parallel. G_s is generally extremely small in high resistivity materials and can be ignored. The S21 transmission coefficient measured

by network analyzer can be used to calculate the microwave photoconductive ON/OFF ratio (with and without illumination):

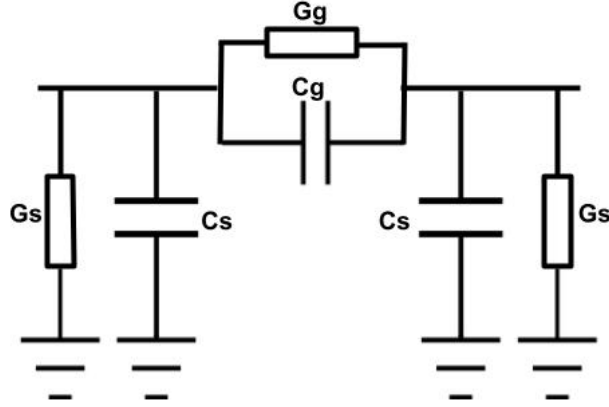


Figure 18: (a) Equivalent circuit model of such types of photoconductive switches. G and C refer respectively to conductance and capacitance, while the subscript of 'g' and 's' refer respectively 'gap' and 'shunt'.

$$R_{\frac{on}{off}} = \frac{S_{21}(On)}{S_{21}(Off)} = R_{on/off} \cdot e^{j\Delta\phi_{on/off}} \quad (1)$$

$$S_{21}(Off) = \frac{j2\omega Z_0 C_g}{(1+j2\omega Z_0 C_g)} \quad (2)$$

$$S_{21}(Onn) = \frac{2Z_0 G_g (1+j\omega \frac{C_g}{G_g})}{(1+2Z_0 G_g) \left(1 + \frac{j\omega 2Z_0 C_g}{(1+2Z_0 G_g)}\right)} \quad (3)$$

$$\left| R_{\frac{on}{off}} \right| = \sqrt{\frac{(G_g^2 + C_g^2 \omega^2)(1 + 4C_g^2 Z_0^2 \omega^2)}{4C_g^4 Z_0^2 \omega^4 + C_g^2 (\omega + 2G_g Z_0 \omega)^2}} \quad (4)$$

where ω is the angular frequency in radians per second of the input electrical signal, Z_0 is the characteristic impedance of the input and output accesses of the device ($= 50 \Omega$), G_g and C_g is the gap conductance and gap capacitance described above, respectively.

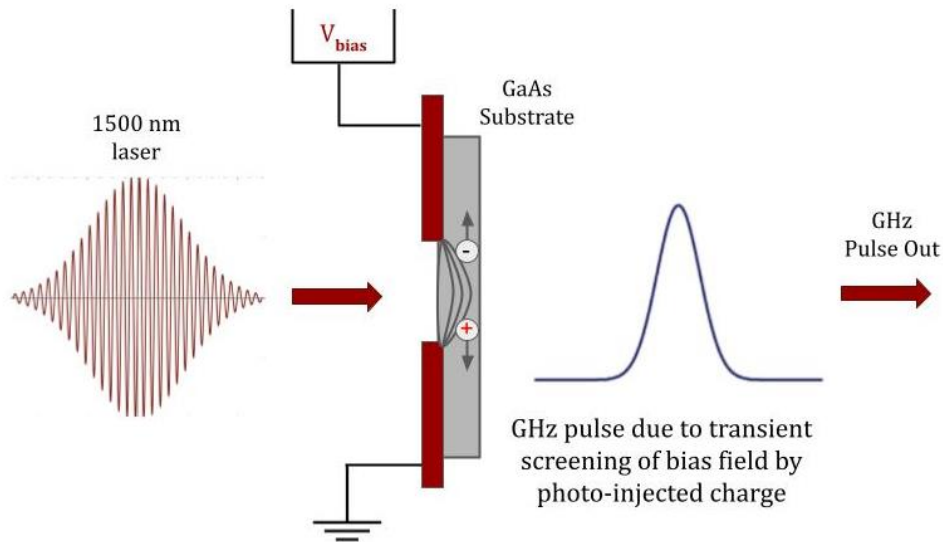


Figure 19: Schematic of THz generation using a photoconductive switch⁸⁸

1.2.1.3. Photoconductive switch operating at SWIR range ($\lambda = 1.55 \mu\text{m}$)

Several research efforts have been devoted to the development of photoconductive switches operate in the short-wave-infrared spectrum window (i.e., 1.3 - 1.55 μm). For example, efforts have been made to elevate the TPA (trap-assisted two-photon absorption) LT-GaAs to make photoconductive switch working under SWIR range, but the device performance was limited by the low absorption of TPA coefficient in LT-GaAs⁸⁹. Another strategy by lowering the bandgap of GaNAsSb⁸⁷ to 0.8eV through increasing the nitrogen concentration and antimony doping. This makes switch functional at 1.55 μm and with ON/OFF ratio of 9dB at microwave signal frequency of 1.5 GHz. Photoconductive switch with similar objectives on 2D materials such exfoliated black phosphorus, a maximum ON/OFF ratio was achieved at 1 GHz, and has a signal-to-noise ratio of 17.2 dB.⁹⁰

1.2.1.4. SWIR

Short-wave infrared (SWIR) generally refers to the photon ranging from in wavelength 1 to 3-micron electromagnetic spectrum.^{91–93} Application in this wavelength range benefit from a verity of advantages including long penetration length in biological tissue, spectral coverage of atmospheric nightglow and the distinctive excitation energy of specific molecular vibrational modes. Thus, in SWIR based devices is used for achieving optical communication, in sensing of environmental gases, and passive night vision.⁹⁴

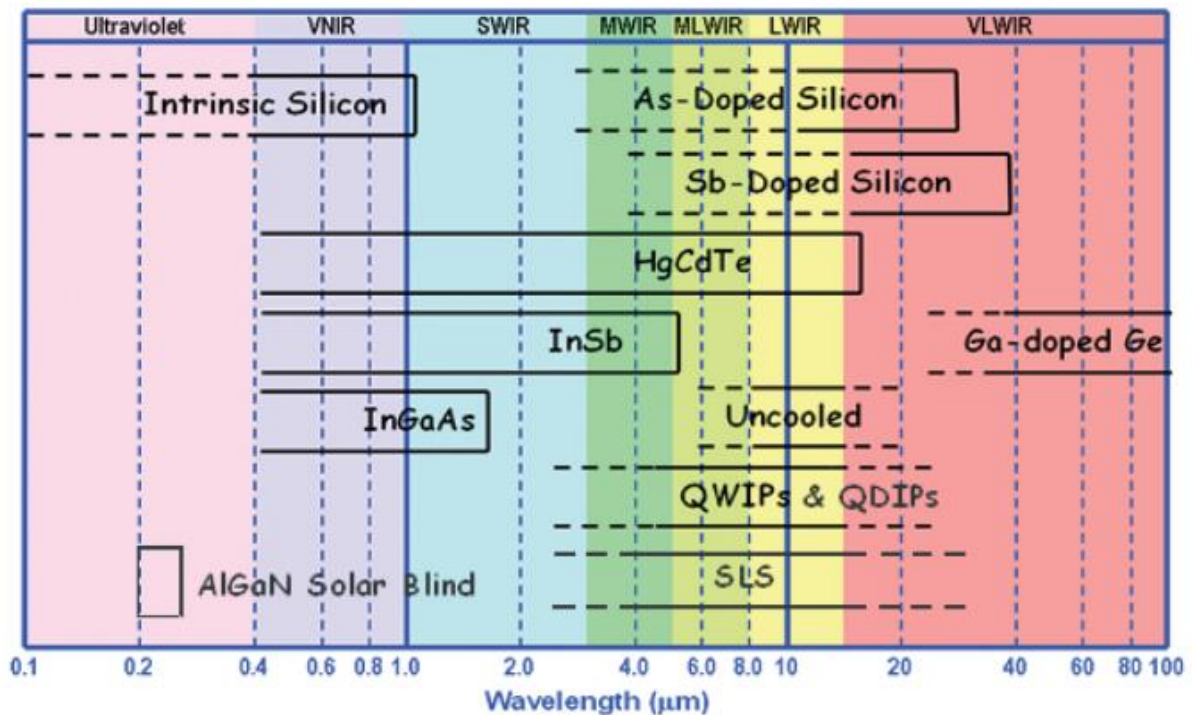


Figure 20: Material systems for UV-visible-infrared detection. Except for the bottom two entries, these material systems have been known and developed for decades.⁹⁵

Current SWIR technology rely primarily on low-bandgap semiconductors like Indium Gallium Arsenide (InGaAs), Indium antimonide (InSb), and mercury cadmium telluride (HgCdTe). A list of materials can be shown in the **figure 20** depicts material in the range of UV-Vis-infrared light. We can see from this image all the materials cover nearly the entire spectrum from 0.1 m to 100 m. However, only the silicon (Si) is inexpensive; the devices beyond the visible spectrum are expensive due to epitaxial growth requirements and unfriendly environment having highly heavy metal elements that are toxic. For example, because of rarity of InGaAs it is an expensive material. For these practical reasons, ongoing efforts are

made to find suitable materials to replace the costly and toxic metal elements. Many new materials have emerged in the last year; including 2D materials,⁹⁶ colloidal lead sulphide⁹⁷ and plasmonic nanostructures, and last but not least Lanthanide-based fluoride upconversion nanocrystals, which allow devices to operate in the SWIR range. This material has already been thoroughly discussed in the materials sections.

1.2.2. Transistors

1.2.2.1. Introduction

A transistor is a type of semiconductor device that is used to amplify or switch electrical signals and power. The transistor is a fundamental component of modern electronics. It is typically made of semiconductor material and has at least three terminals for connecting to an electronic circuit. A voltage or current applied to one pair of terminals of the transistor and controls the current flowing through another pair of terminals.⁹⁸ The metal–oxide–semiconductor field-effect transistor (MOSFET) is the transistor that is most widely used which was invented in 1959 by Mohamed Atalla and Dawon Kahng at Bell Labs. Transistors revolutionized the field of electronics, paving the way for smaller and cheaper radios, calculators, and computers, among other things shown in **figure 21**.⁹⁹

In 2007, display manufacturers produced approximately 50 square kilometres of liquid crystal displays containing approximately 10^{15} TFTs and sold them for approximately \$100 billion. The majority of these TFTs are made of amorphous silicon (a-Si), with a smaller proportion made of polycrystalline silicon. TFTs are most commonly used in displays, but they are also used in digital X-ray imagers and have potential applications in radio-frequency identification (RFID) tags, sensing devices, various medical applications, and low-cost disposable electronics. Despite the success of thin film Si, there is an active search for new and better TFTs to meet anticipated future needs, the primary ones being the following.¹⁰⁰ TFTs have the same roots as silicon field-effect transistor (FET) and integrated circuit (IC) fabrication, but the two technologies have diverged due to different applications. Silicon integrated circuits have become increasingly dense because size is no longer a constraint, and as feature size is reduced, both cost and performance improve. TFTs, on the other hand, are driven by large substrate size rather than device density. TFTs have a lower cost per unit area than silicon ICs due to different fabrication methods, but the cost per FET is much

higher. As a result, TFTs cannot compete with silicon ICs in terms of processing power, and silicon ICs will never be manufactured in square meter size arrays. Only in a few applications is the choice between TFTs and silicon ICs obvious.^{101 102}

As previously reported, interest in this field has steadily increased since the invention of the first polymer and small molecule^{17,18} semiconductor field-effect transistors (FETs) for both technological and scientific reasons. In recent years, there has been a significant increase in the number of publications on field effect transistors. Field Effect Transistors are technologically interesting because they have the potential to be the main component in low-cost, flexible electronic circuits. One of the most important potential applications is radio frequency identification. RFID (radio-frequency identification) tags and flexible displays from these prototypes have been demonstrated and are on their way to the market.

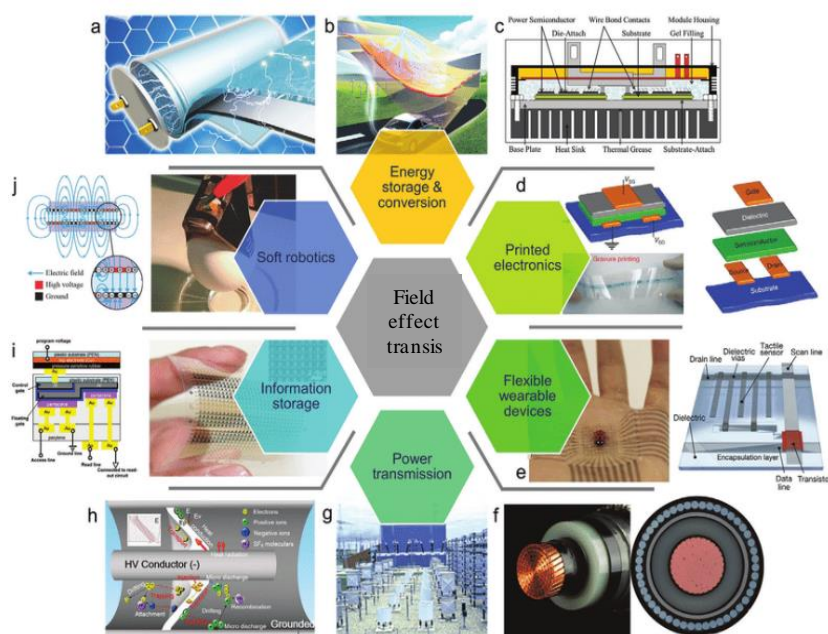


Figure 21: Main application field effect Transistors in today's technological world.^{103,104}

1.2.2.2. Basics of Field-Effect Transistors

We'll go over the fundamental structures and operating principles of field-effect transistors, as well as their current applications, voltage characteristics, and data extraction techniques. We'll go over the most common charges briefly, as well as the role of the gate dielectric and transport models in FETs.

1.2.2.2.1. Working Principle of FETs

The following components shown in **figure 22(a)** are required for a field-effect transistor (organic or inorganic): an insulating gate dielectric that separates a thin semiconducting layer from a gate electrode; source and drain electrodes separated by a distance L (channel length) and of width W (channel width) that are in contact with the semiconducting material layer. In the case of an organic FET, the semiconducting layer is typically vacuum sublimed, spin-coated, or drop-cast based on the semiconductor. The gate electrode can be made of metal or a conducting polymer, but it is almost always highly doped silicon serves as both the substrate and the gate electrode at the same time.¹⁰⁵ Gate dielectric¹⁰⁶ such as SiO_2 (thermally grown on Si or sputtered), Al_2O_3 , and Si_3N_4 , are used or polymeric insulators, such as poly (methyl methacrylate), poly(4-vinylphenol) (PVP) or poly(4-vinylmethacrylate) (PMMA) are commonly used as gate dielectric based on transistor structure¹⁰⁷. The source and drain electrodes, which inject charges into the semiconductor, are typically made of metals with a high work function gold (along with Pd, Pt, and Ag), but conducting polymers (for example, PEDOT: PSS, PANI)¹⁰⁸ can be printed as well.¹⁰⁹

Normally, voltage is applied to the gate electrode (V_g) and the drain electrode (V_d). Generally, the source electrode is grounded so the value is 0 for (V_s). The potential distinction between the source and the gate voltage is commonly referred to as the gate voltage. Whereas, the potential difference between the source and the drain is called the source-drain voltage (V_{ds}). The source electrode is always referred as the charge-injecting electrode, it is always more negative than the gate electrode when a positive voltage is applied i.e., electrons are injected whereas source electrode is more positive when a negative gate voltage is applied i.e., holes are injected.

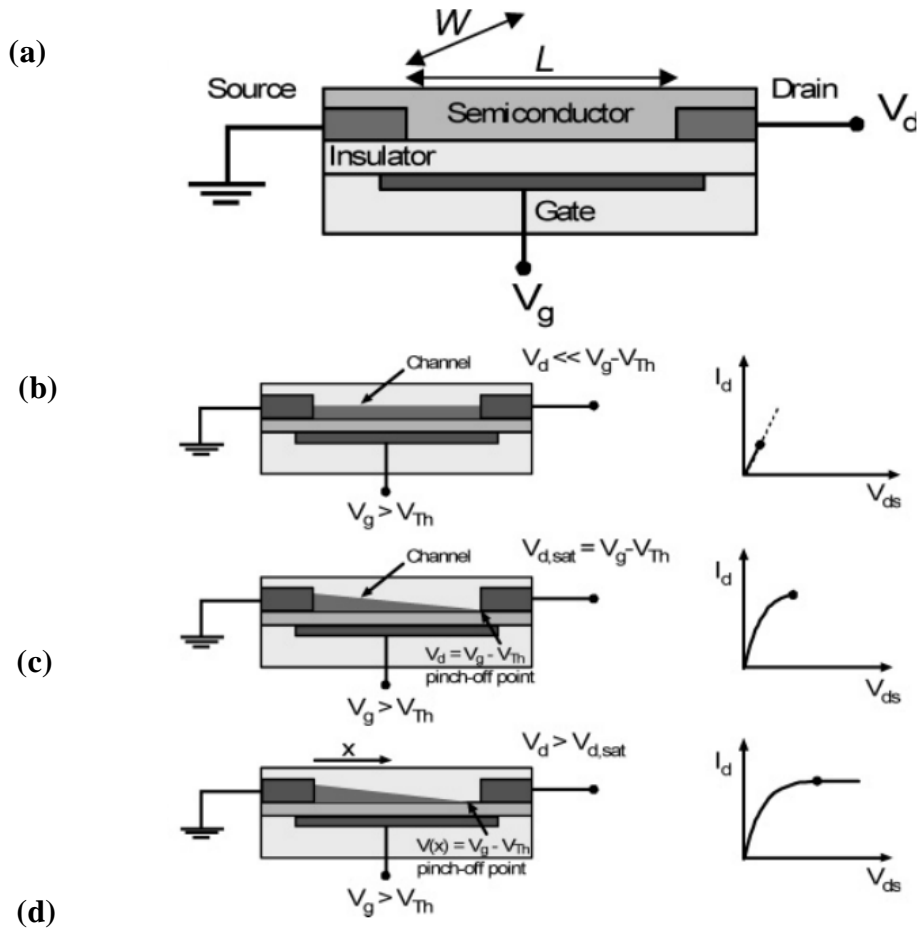


Figure 22: (a) Schematic structure of a field-effect transistor and applied voltages: L = channel length; W = channel width; V_d = drain voltage; V_g = gate voltage; V_{TH} = threshold voltage; I_d = drain current. (b-d) Illustrations of operating regimes of field-effect transistors: (b) linear regime; (c) start of saturation regime at pinch off; (d) saturation regime and corresponding current-voltage characteristics.¹¹⁰

Figure 22b-d depicts the fundamental operating regimes and associated current-voltage characteristics of a field-effect transistor. To begin, we can consider a simple metal-insulator semiconductor (MIS) diode (there is no potential voltage i.e., difference between source and drain), voltage V_g is applied on gate electrode. As explained before when positive or negative gate voltage that will induce electrons or holes at the insulator/semiconductor interface that was injected by ground electrode i.e., source. Therefore, the number of accumulated charges is proportional to V_g and capacitance C_i of the insulator. Nevertheless, not all induced charges are mobile thus responsible for current in field-effect transistor. Before making additionally charge carrier mobile, deep trap has to filled first. Therefore, a

higher gate voltage than the threshold V_{TH} has to be applied and the effective gate voltage will be $V_g - V_{TH}$. On the other side, at the acceptor (for p-channel) and donor (n-channel) states and interface dipole an internal potential is created at the interface and leads to accumulation of charge carrier in the channel when applied gate voltage (V_g) is 0. As a result, in some cases an opposite voltage must be applied to turn off the channel.^{111,112}

The charge carrier concentration in the transistor channel is uniform when no source-drain bias is applied. When a small source-drain voltage is applied a linear gradient of charge density formed from the carrier injecting source to the extracting drain electrode as seen in figure 22b ($V_{ds} \ll V_g$). This is the linear regime where in the flow of current through the channel is directly proportional to V_{ds} . Therefore, potential $V(x)$ increases linearly from the source within the channel ($x = 0, V(x) = 0$) to V_{ds} at the drain electrode ($x = L, V(x) = V_{ds}$).

When the source-drain voltage is increased further, point $V_{ds} = V_g - V_{TH}$ is reached, where the channel is “pinch off” (figure 22c). which leads to the formation of depletion region next to drain because the difference between the gate voltage and the local potential $V(x)$ is below threshold voltage. Because of high electric field in the depletion region carriers formed by a space-charge-limited saturation current $I_{ds,sat}$ current can flow across this narrow depletion zone are swept from the pinch-off point to the drain. Increasing the source-drain voltage further does not significantly increase the current but does cause the depletion region to expand, resulting in a slight shortening of the channel. Because the potential at the pinch-off point is still $V_g - V_{TH}$, therefore the potential drop between the point and the source electrode remains relatively constant, and the current saturates at an $I_{ds,sat}$ level.

It is important to note that transistor with short channel length needs thin gate dielectric, usually $L > 10d_{dielectrics}$,^{113,114} so as to ensure that the gate voltage created field determines channel's charge distribution (gradual channel approximation) and in relation to the source-drain voltage it is not dominated by the lateral field. Alternatively, saturation will be prevented by a space-charge limited bulk current and the gate voltage will not be able to determine whether the transistor is “on” or “off”.^{115–117}

1.2.1.2. Figures of Merits of FETs

The current-voltage characteristics of field effect transistor in different regimes described by using the gradual channel approximation. That is, the field generated by gate flow by gate voltage which is perpendicular to the current flow is much greater than the electric field caused by drain voltage which is in parallel with current flow. This is true for long channel transistors but begins to fail for very short channel length transistors.

The induced mobile charge carriers Q_{mob} per unit area at a given gate potential is greater than the threshold voltage V_{TH} at the source contact is linked to V_g via,

$$Q_{mob} = C_i (V_g - V_{Th}) \quad (1)$$

In which C_i denotes capacitance per unit area of gate dielectric. The channel potential is assumed to be zero in equation 1. Even so, the induced charge density is position dependent along the channel (x), which is taken into account in the following equation:

$$Q_{mob} = C_i (V_g - V_{Th} - V(x)) \quad (2)$$

Without taking into account diffusion, the source-drain current (I_d) induced by carriers is

$$I_d dx = W \mu Q_{mob} E_x \quad (3)$$

In which W is the width of channel, and E_x is the electric field at x . By replacing $E_x = dV/dx$ and equation 2 into equation 3 we find

$$I_d dx = W \mu C_i (V_g - V_{Th} - V(x)) dV \quad (4)$$

Integration of the current increment from x yields the gradual channel expression for the drain current from $x = 0$ to L , i.e., $V(x)=0$ to V_{ds} assuming the mobility is independent of carrier density and thus gate voltage is:

$$I_d = \frac{W}{L} \mu C_i \left[(V_g - V_{Th}) V_d - \frac{1}{2} V_{ds}^2 \right] \quad (5)$$

This can be simplified in the linear regime with $V_{ds} \ll V_g$ to

$$I_d = \frac{W}{L} \mu_{lin} C_i (V_g - V_{Th}) V_{ds} \quad (6)$$

In the above equation drain current is directly proportional to V_g , the field effect mobility in the linear regime (*lin*) can be calculated by gradient of I_d versus V_{ds} (also applied for gate voltage dependent mobilities)

$$\mu_{lin} = \frac{\partial I_{ds}}{\partial V_g} * \frac{L}{WC_i V_{ds}} \quad (7)$$

As previously stated, the channel is pinched off when $V_{ds} = V_g - V_{Th}$. The current cannot be increased significantly any longer as well as saturates ($I_{ds,sat}$). As a result, equation 5 is no longer valid. Ignoring channel shortening as a result of the depletion region the saturation current at the drain can be calculated by substituting V_{ds} with $V_g - V_{Th}$, we get

$$I_{ds,sat} = \frac{W}{2L} \mu_{sat} C_i (V_g - V_{Th})^2 \quad (8)$$

The square root of the saturation current is directly proportional to the gate voltage in the saturation regime. This equation implies that mobility is independent of gate voltage. If this is not the case, a gate voltage dependent saturation mobility (μ_{sat}) will be calculated by using

$$\mu_{sat}(V_g) = \frac{\partial I_{ds,sat}}{\partial V_g} * \frac{L}{WC_i} * \frac{1}{(V_g - V_{Th})} \quad (9)$$

Figure 23a depicts the typical output characteristics (include the different gate voltage for drain current versus source drain voltage). In the output characteristics clearly shows the linear regime at low V_d and the saturation regime at high V_{ds} .

Figure 23b depicts the transfer characteristics (drain current versus gate voltage at constant drain source current V_{ds}) of transistor in liner regime ($V_{ds} \ll V_g$) in both semi log and linear plot. Onset voltage (V_{on}) can be easily determined from the semi log plot (i.e., the voltage at which drain current increases drastically above a predefined low off-current value) and the subthreshold swing ($S = dV_g/d(\log I_{ds})$), depending on the trap states and the gate dielectric capacitance at the interface. According to equation 7, the gradient of the current increases in the linear regime is directly proportional to the mobility and its constant if the mobility of gate voltage independent. However, most semiconductor exhibit gate voltage dependent mobilities that leads to curve shape deviation from being linear.

Figure 23c depicts a transfer curve in saturation regime, the square root of the drain current must be linearly depended on the gate voltage, and the gradient is proportional to the

mobility according to equation 8. By extrapolating the linear fit to zero threshold voltage is obtained.

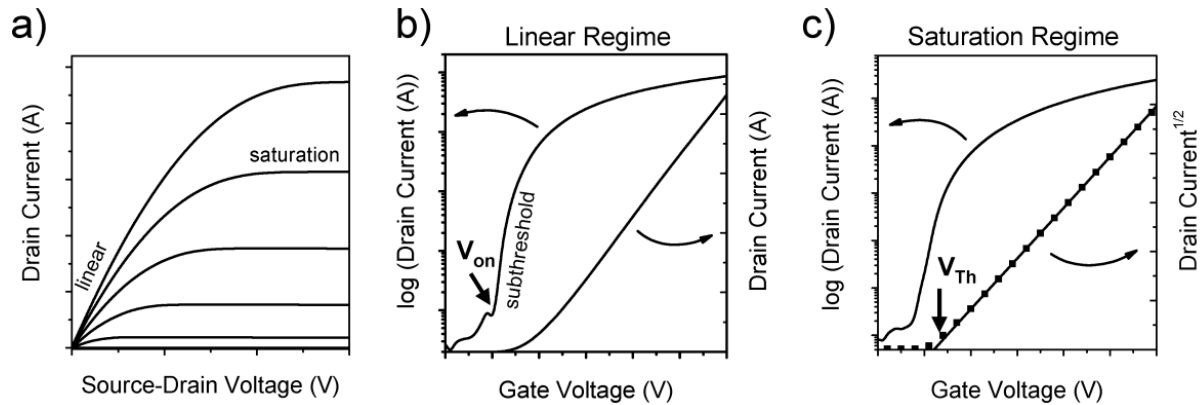


Figure 23: shows a field-effect transistor current-voltage characteristics (a) output characteristics showing linear and saturation regimes; (b) transfer characteristics of transistor in linear regimes ($V_d \ll V_g$) showing onset voltage V_{on} when drain current increases suddenly; (c) transfer characteristics in saturation regime showing threshold voltage, in which x-axis intersect the linear fit to the square root of the drain current.¹¹⁰

Threshold voltages can be caused by a variety of effects and are heavily influenced by the semiconductor and dielectric used. Impurities, interface states, and, in particular, built-in dipoles. The threshold voltage is influenced by charge traps.¹⁰⁶ A change in the threshold voltage on the current-voltage time scale Current hysteresis is caused by measurements (usually forward scan reveals higher currents than the reverse scan). Memory devices can make use of large stable threshold shifts, such as those caused by polarization of ferroelectric gate dielectrics.¹¹⁸

Another important characteristic is the On/Off ratio (I_{ON}/I_{OFF}), which is the ratio of drain current in the on-state to drain current in the off-state for a given gate voltage. This value should be as high as possible for the clean switching behavior of the transistor. It is possible to disregard the effect of contact resistance at the source-drain electrodes. I_{ON} is ordinarily determined by the semiconductor and capacitance of the gate dielectric. For determining the off current (I_{OFF}) magnitude by gate leakage, particularly for unpatterned gate electrode and semiconductor layer at the substrate interface by conduction pathways and

also due to bulk conductivity of the semiconductor which increases as a result of unintentional doping.³⁴

1.2.1.3. Optoelectronic field effect memory transistors:

Electronic devices have become an integral part of our lives since 90's. The memory component is essential for electronic information products (computers, mobile phones, wearable devices etc.). Massive data storage is also required for mining the values of the data. As a result, with the advent of rise of internet of things, 5G, big data analysis and the artificial intelligence (AI) era, the semiconductor market begun a round of explosive growth for memory devices (**figure 24**).¹¹⁹ Traditional memories use optical, electrical and magnetic signals for storing information. So, the memory component is limiting the performance of the current computer system instead of processing data which is known as “von Neumann bottleneck” or memory wall”.¹²⁰ To address these issues, the scientific community have been putting a considerable effort for the development of novel high-performance memories.

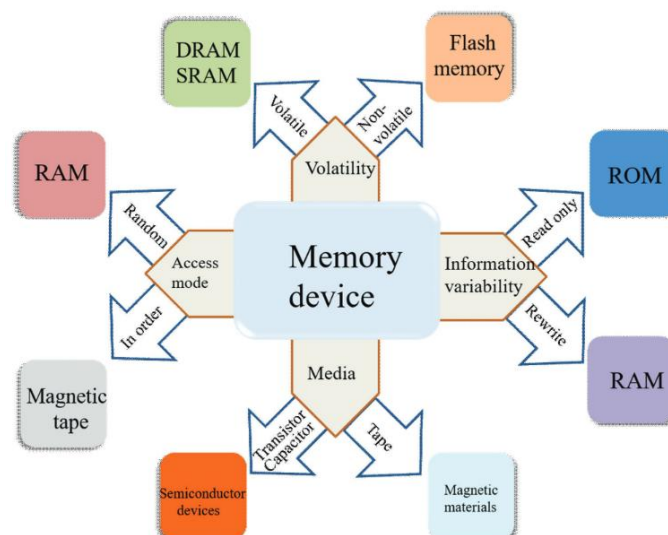


Figure 24: Schematic illustration of the classification of memory devices.¹²¹

Traditionally the transistors-based memories are equally under intense research with other types of memory including memristors, phase-change memory and ferroelectric memory.^{122–124} Science Kahng and Sze used floating gate device to create non-volatile

memory in 1967, floating gate memories has grown in popularity by possessing advantages like low power consumption, high reliability, high density, low power consumption and high compatibility with CMOS industry. However, the potential of the current floating gate transistor is getting exhausted because of certain limitations physical and technical. Further development of memory transistor relies on material parameters like morphology, crystallography, energy level alignment between the constituent materials, etc. and breakthrough in device concept.

The so-called quantum limit of Moore's law is currently posing a challenge to memory capacity development. By taking an advantage of light's ultrafast signals and wide bandwidth optical spectrum. Therefore, by combining non-volatile memory and light, phototransistor memory is a promising candidate for next generation of electronics.¹²⁵ The phototransistor memory is classified into three types based on its operating mechanism: (a) photographic memory,^{126,127} (b) photo erasure memory,¹²⁸ (c) completely photo driven memory.¹²⁹

1.2.1.4. Working mechanism of optical memory transistor:

Non-volatile memories divided into two parts based on their storage mechanism: (i) oriented-dipole memory (ii) charge-trapping memory

i. Oriented dipole memory: The oriented-dipole device is an FeFET device that involves the electrically switchable spontaneous polarization of ferroelectric materials.

ii. Charge-trapping memory: For example, by taking p-type channel in field effect transistor memory by applying a negative voltage to the gate electrode allow injection of holes from the source electrode and causes accumulation regime in the channel. The accumulated holes injecting into the charge storage layer (i.e., floating gate) when the negative gate voltage is above specific range by direct tunnelling or Fowler-Nordheim (FN) tunnelling mechanism.^{130,131} There is a negative shift to the transfer curve and change in threshold voltage (V_{th}) because of these trapped charges which alter the carrier distribution in the channel. Therefore, the memory is switched to programmed state and the process is called "**programming**". When a positive gate voltage applied the trapped charge carriers either go back to the channel through tunnelling or recombine with the injected opposite charges

that is depend on the transporting behaviour of the channel. This procedure causes the transfer curve back to the erased state (initial state), which is called “erasing” operation.

A mechanism for optical filed effect transistor shown in **figure 25**¹³² where a transistor-based memory records information through the semiconductor layers conductive states, which are tuneable by the device’s charge storage. In this mechanism by illuminating light on the semiconductor photo responsive materials the photoinduced exciton dissociates into electron and holes. One of the charge carriers’ tunnels into the channel layer and counterpart of the other carriers accumulates in charge trap layer and the gate conductance states the channel. In order to restore the memory device to its OFF state, a positive/negative gate bias is then used to draw electrons/holes from the channel layer to the eletret. The attracted electron/holes are then recombined with the trapped hole/electron.

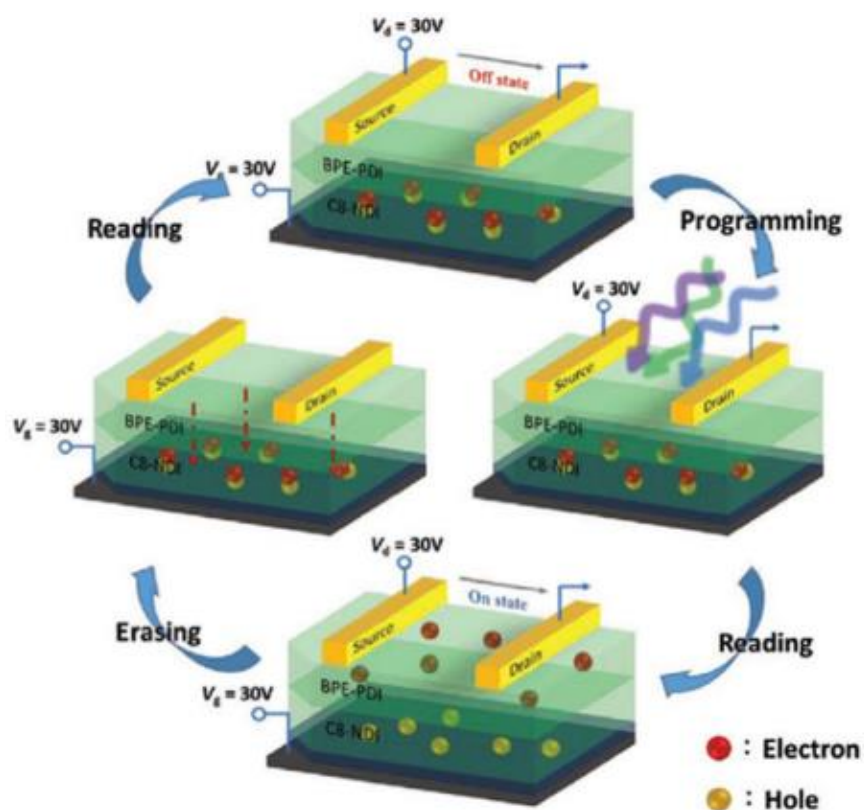


Figure 25: the corresponding working mechanism of the device with photo writing and electrical erasing operations.¹³²

As result, in a transistor-based memory, the charge storage media is crucial. In an effort to enhance device performance, a wide variety of materials including metals,^{133,134} dielectrics,¹³⁵ and semiconductors,^{136–138} and their properties have been researched for their

application as the charge storage in transistor-based memory medium that beyond silicon.¹²² Among all the materials semiconductor nanocrystals (NCs) have stood out due to their distinct qualities.¹³⁹ Typically, the charge transfer between semiconductor NCs is prohibited, which effectively prevents charge loss. The abundance of surface states in NCs creates an enormous charge storage potential.⁵⁷ The memory based on transistors can also be programmed and erased by light due to the excellent light absorption capability and electronic bandgap of semiconductor NCs. Given the tremendous potential, the final characteristic is particularly appealing in optoelectronic memory^{139–141} in all-optical circuits and artificial neuromorphic computer application.^{142,143} For instance, Han *et al.* demonstrated an effective photonic synapse for neuromorphic computing in 2018 using Perovskite quantum dots as charge storage medium, also Zhenhua *et al.* 2021¹⁴⁴ reported excellent memory retention properties in N doped TiO₂. Despite the fact that optoelectronic memories have utilized carbon NCs,¹⁴⁵ perovskites,¹⁴⁰ CdSe,¹³⁶ CdSe/ZnS core-shell,¹⁴⁶ etc.¹⁴⁷ a number of semiconductors with excellent, investigating properties has not yet been done

1.2.1.5. Performance Figures of Merit:¹³¹

Optoelectronic field effect transistor memory has been described in terms of a number of significant metrics, memory capacity, speed, reliability and power consumption.

Memory capacity (Δn): Typically, the memory window (V_{th}) value, which refers to the difference in threshold voltage between the programming state and the erasing state, is used to describe the memory capacity, which can be expressed as

$$\Delta V_{th} = V_{th}^{PRM} - V_{th}^{ERS} \quad (1)$$

The number of trapped charge carriers per unit area is known as the charge-trapping density (n), and it may be determined using the following equation

$$\Delta n = \frac{\Delta V_{th} \cdot C_i}{e} \quad (2)$$

Where C_i is the total capacitance per unit area, e is the element charge (1.602×10^{-19}) also C_i can be calculated approximately or directly from $C_i - F/C_i - V$ plots

$$\frac{1}{C_i} = \frac{1}{C_{TDL}} + \frac{1}{C_{CTL}} + \frac{1}{C_{BDL}} \quad (3)$$

In state-of-art of optoelectronic memory FETs the values of Δn values are in range of 10^{12} to 10^{13} cm^{-2} , despite of their widespread ΔV_{th} , Δn exhibit small variation among different devices.

The lack of variation in Δn associate to the fact that OFET memory require high operating voltage for low C_i and long programming time (t_{prog}), resulting in $C_i \Delta V_{th}$ product (and thus Δn) shows similar range in different devices systems. To objectively evaluate the performance of the photodetectors made with different martials and geometries, a new evaluation parameter has been purposed i.e., memory efficiency (η) defined as

$$\eta = \frac{\Delta n}{V_{GS} \cdot t_{prog}} \quad (4)$$

For proper memory functioning, Equation (4) takes into account all the influencing elements, such as total area capacitance, power consumption, and speed.

- (a) Speed:** it is defined as the operating speed is the time of charge tunnelling between the channel and the charge trapping layer. A low operating time relates to a fast access speed. Generally, OFET memory is of the order of $100\mu\text{s}$ to 1s for reasonable memory window, which is constrained by relatively low semiconducting mobility and long channel length (L , tens of micrometre) and low-k dielectric.
- (b) Reliability:** There are two main components to reliability. First, the retention time reflecting stability of charge trapping. For commercialized OFET memory products should retain memory over 10 years (approximately 3.15×10^8) at ambient temperature, but present research suggests about 10^3 to 10^6 s. An efficient technique used to examine the stability of OFET memory devices in the lab is extrapolation of the retention time plots. Secondly, persistence describes the memory device capacity to resist several program/erase cycles. Over 10^6 is the ideal endurance for non-volatile secondary storage and 10^{12} cycle for main memory. By enhancing the TDLs and BDLs' thickness and quality, the reliability can be enhanced. It is suggested to use the memory ratio (MR) to assess the dependability of OFET memory at a chosen bias-stress period or cycle number, which is denoted by

$$MR = \frac{I_{DS}^{ON}}{I_{DS}^{OFF}} \quad (5)$$

Where, I_{DS}^{ON} and I_{DS}^{OFF} are drain current programmed and erased state at fixed gate voltage (V_R).

- (c) **Power consumption:** The writing/erasing gate voltage and the supplied drain voltage are both included in the operational power. An OFET memory must have a writing/erasing voltage below 10V to enable low-power integrated circuit (IC) designs.

1.2.3. Graphene Based transistor

1.2.3.1. Graphene

As the structure (figure 26) and performance of silicon transistors challenge their physical limits, there is an urgent need to investigate appropriate materials to support new technologies.¹⁴⁸ Graphene has been reimagining electronics since October 2004, when Andre Geim and Kostya Novoselov¹⁴⁹ discovered how to extract a single layer of carbon lattice from graphite. Graphene is typically found in the form of highly ordered pyrolytic graphite (HOPG), in which individual layers of graphene are stacked on top of each other to form a crystalline lattice. Its stability can be attributed to a densely packed, periodic array of carbon atoms.

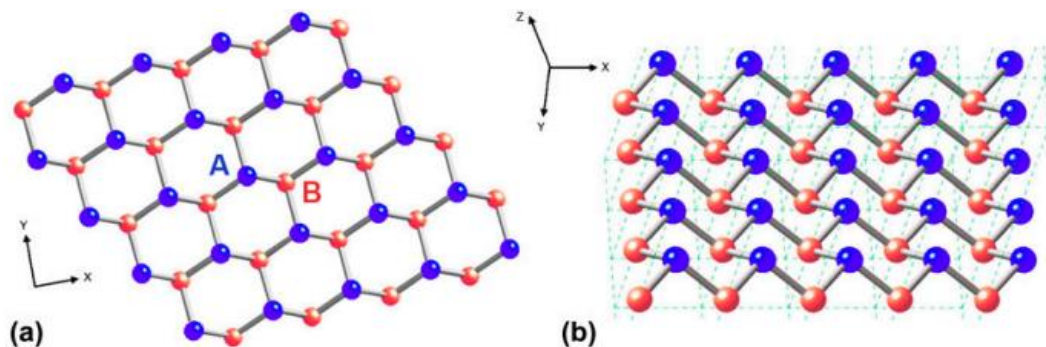


Figure 26: (a) The two-dimensional honeycomb lattice is depicted, with carbon atoms A and B per unit cell. The shape of graphene or other two-dimensional crystals (such as silicene, BN, or germanene) can be roughly flat or slightly corrugated (see Figure side-view)(b)).¹⁵⁰

Furthermore, the method of preparation for graphene will have a significant impact on its overall quality and characteristics.¹⁵¹ As study conducted by Geim *et al.* 2007. Three techniques include **figure 27** mechanical exfoliation one of the most basic methods of producing a graphene layer.¹⁵² Exfoliated graphene has a mobility of $15,000 \text{ cm}^2 \text{ V}^{-1} \text{ s}^{-1}$.¹⁵³ Despite its small size, this method is a simple way of producing graphene, but this method

produces only small amounts each time. Second technique is Vacuum epitaxial growth technique in this technique graphene produced typically has an intermediate mobility range, which is lower than for exfoliated graphene but higher as compared to CVD. Graphene Coated silicon carbide (SiC) on a silicon wafer, requiring high temperatures.¹⁵⁴ Both silicon and carbon atoms would Individually become isolated, because silicon atoms are only evaporated at temperatures above 1000 K therefore carbon atoms remain and graphene will grow on the substrate later. In any case, structure Defects are always found because carbon atoms are occasionally burned due to high temperatures – thus being oxygen and hydrogen contamination.¹⁵⁵ Last and most preferred technique for industry for mass production of graphene. High-temperature chemical reactions are used in the process, hydrocarbon gases (such as H₂ and CH₄), as well as a catalytic metal surface, such as copper or nickel **Figure 27b**. These Metals aid in the breakdown of chemical bonds, and form a hexagonal (honeycomb) lattice out of carbon atoms. As a result, the larger the metal surface, the greater the quantity graphene that can be manufactured. The is used for this purpose a polished polycrystalline copper foil is the most common. It is simple to transfer graphene from this metal surface to another substrates, such as by applying a voltage. As a result, the CVD method outperforms the other methods on a large scale in comparison to other graphene production methods.^{154,156}

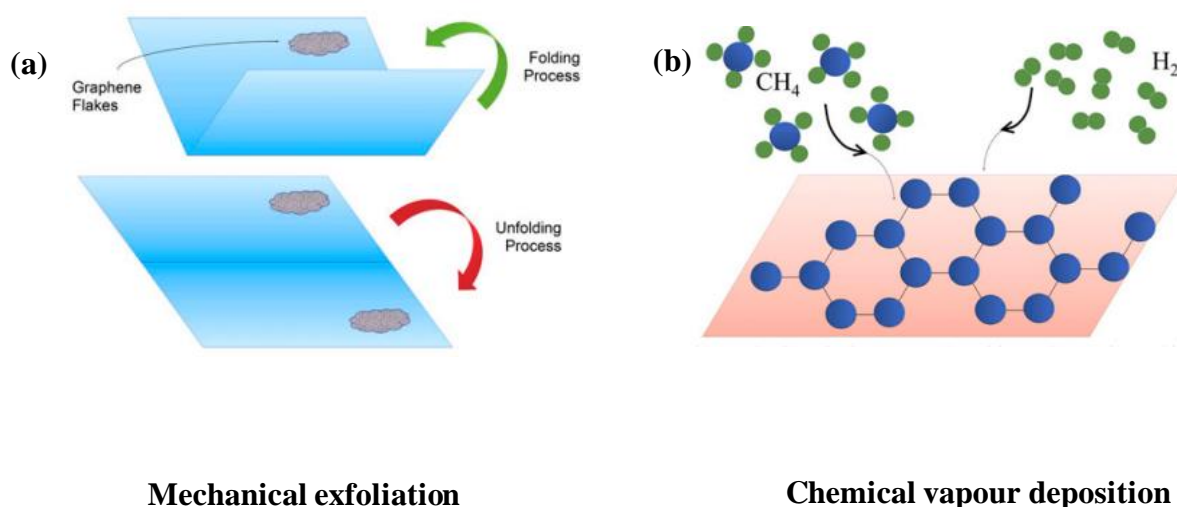


Figure 27: (a) The simplest method of separating graphene from graphite is the 'scotch-tape' method. (b) Chemical vapour deposition (CVD)^{157,158}

In addition to its exceptional electrical, thermal and, in general, optical properties. As a result, graphene has become a highly sought-after material for future semiconducting and optoelectronic devices.^{150,154,159}

- **High electrical properties:** In theory, graphene can conduct electricity with 100 % efficiency. At room temperature, graphene has a very low resistivity and an intrinsic mobility that is more than 100 times that of silicon. Under particular conditions (such as twisting bilayer graphene at an angle of 1.1 degrees or chilling it to 1.7°C above absolute zero), it also demonstrates superconductivity.⁶⁹
- **High thermal conductivity:** Graphene is an isotropic conductor that emits heat in all directions and has higher thermal conductivity than diamond, carbon nanotubes, and graphite.¹⁶⁰
- **Excellent optical properties:** Despite being extremely thin, graphene is visible and can absorb approximately 2.3% of white light. (This is a great deal of 2D material.) Graphene is an attractive material for the construction of highly efficient solar cells as a result of this ability and its superior electrical properties.⁷⁵
- **Excellent chemical properties:** Graphene is a chemically inert material that does not readily react with other materials. However, under certain conditions, it can absorb various molecules and atoms, causing its properties to change. As a result, it is appropriate for applications like chemical and biological sensors.¹⁵⁶
- **Quantum Klein tunnelling:** **Figure 28a** depicts Klein tunnelling with excellent transmission through the barrier. A particle with kinetic energy is defined in classical mechanics as for the sake of argument, energy K is incapable of crossing a potential barrier U . $K < U$ condition However, according to quantum mechanics, a particle can tunnel through the barrier with some degree of certainty, even when $K < U$. This is especially unusual in the case of graphene. A particle can tunnel through the barrier at certain angles flawless with transmission
- **Energy spectrum and anomalous quantum Hall effect:** **Figure 28b** the conduction and valence bands of graphene come together at six points in the Brillouin zone. These are known as the Dirac's points Both conduction and convection are present in the vicinity of these points. The bands (red) and valence (blue) are conical in shape. These cones are can be used to describe the dispersion of low energy and momentum ¹⁵⁶

$$E = \pm v_F(\mathbf{p}_x^2 + \mathbf{p}_y^2)^{1/2}$$

Where, v_F is the Fermi velocity, p_x and p_y denotes the electron momentum

The electron momentum is defined by velocity and (p_x, p_y) . The Fermi equation the energy level E_F is commonly associated with the Dirac point – where DoS (density of states) is equal to zero. Electrons are everywhere. states in the valence band, while the conduction band is still present unoccupied.

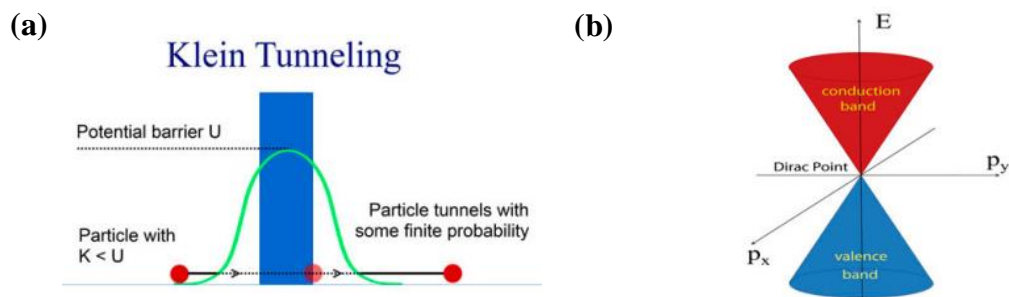


Figure 28: (a) quantum kien Tunneling, (b) Energy spectrum and anomalous quantum Hall effect.¹⁵⁸

Graphene properties important to transistors is band-gap i.e., large-area graphene is a semimetal with a bandgap of zero. It has cone-shaped valence and conduction bands that meet at the Brillouin zone's K points. Because there is no bandgap, devices with large-area graphene channels cannot be switched off, making them unsuitable for logic applications. Nonetheless, the graphene band structure can be changed, and it is possible to open a bandgap in three ways: in one, by constraining large-area graphene dimension, biasing bilayer graphene, and applying strain to graphene to form graphene nanoribbons.¹⁶¹ In **figure 29** mobility the most commonly mentioned benefit of graphene is its high carrier mobility at room temperature, mobility of $10,000\text{--}15,000 \text{ cm}^2 \text{ V}^{-1} \text{ s}^{-1}$. Transport at high fields. When FET gates were several micrometres long, mobility was the effective measure of the device carrier transport speed. However, strictly speaking, the mobility short gate lengths; explains carrier transport in low electric fields. High fields in a significant portion of the channel in modern FETs reduce the significance of mobility to device performance.¹⁵³ As

an electronic material, graphene Graphene is one of the materials being studied, and it is an appealing channel material for field-effect transistors due to its superior electrical, mechanical, and thermal properties.¹⁶²

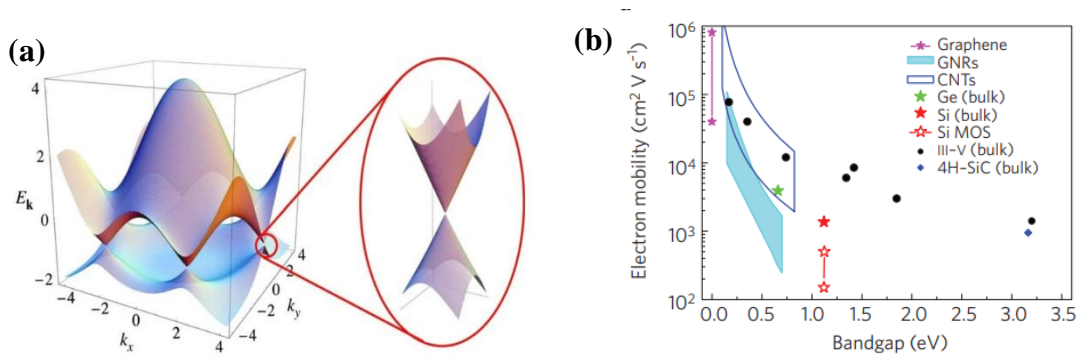


Figure 29: (a) band structure of graphene with the Dirac cones located at the K and K' points in the Brillouin zone.¹⁶³ (b) Electron mobility versus bandgap in low electric fields for various materials, as shown (iii–v compounds are InSb , InAs , $\text{In}_{0.53}\text{Ga}_{0.47}\text{As}$, InP , GaAs , $\text{In}_{0.49}\text{Ga}_{0.51}\text{P}$, and GaN , from left to right).¹⁵³

1.2.3.2. Graphene FET structure and evolution

It has been a decade since Novoselov *et al.* 2000, published their field-effect transport results in few layers graphene the field is now prepared for serious consideration.¹⁵¹ The basic GFET is a three-terminal device that is alike in some aspects to the conventional FET. It has a source, a drain, and a top or back gate. Unlike a silicon-based transistor, the GFET has a thin graphene channel between the source and drain metal electrodes, typically tens of microns thick.

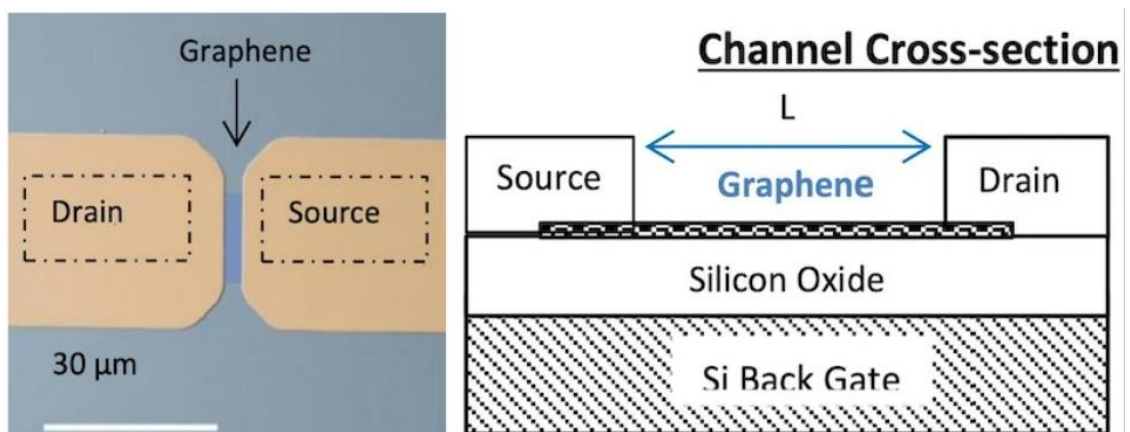


Figure 30: Schematic of Graphene transistor, the gate governs how electrons react, and thus control the channel's behaviour.¹⁴⁹

1.2.3.3. GFET configuration and gate bias

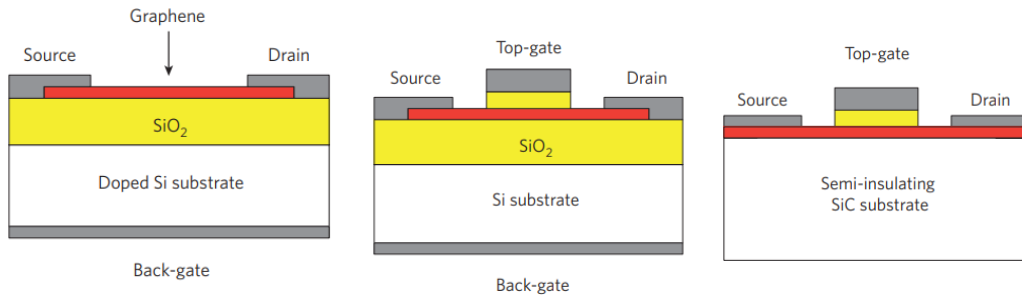


Figure 31: Schematics of different graphene MOSFET types: back-gated GFET (left); top-gated GFET with a channel of exfoliated graphene or of graphene grown on metal and transferred to a SiO_2 -covered Si wafer (middle); top-gated GFET with an epitaxial-graphene channel (right).¹⁵³

The gate in a GFET (**figure 31**), like the gate in traditional silicon FETs, controls the flow of electrons or holes across its channel. Because the transistor channel is only one atom thick, all current flows on its surface, explaining the graphene FETs' high sensitivity. In silicon devices, current flows primarily through electrons or holes. The GFET, on the other hand, allows for equal conduction of electrons and holes. GFET devices typically exhibit ambipolar behavior, with hole carrier conduction occurring in the channel region under negative bias. A positive bias, on the other hand, causes electron carrier conduction.

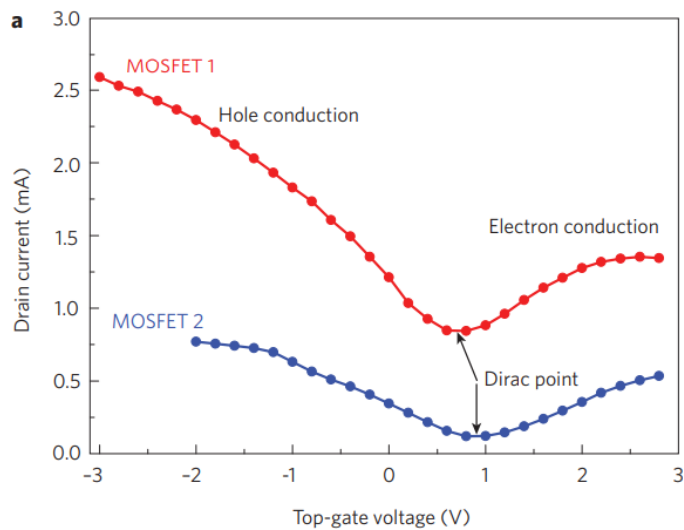


Figure 32: Transfer characteristics and Dirac point for GFET under a back gate bias.¹⁶⁴

The two conduction curves intersect at the Dirac or charge neutrality point (**figure 32**), which should ideally be at zero voltage. In practice, however, the actual Dirac point may vary depending on doping, the level of defects on the surface of graphene, the surrounding atmosphere, and other factors. Some p-doped graphene FET devices, for example, have typical values of 10-40V.

1.2.3.4. The Advantages of Graphene-Based FETs^{153,156}

- As graphene has higher electrical and thermal conductivity than silicon, it has lower resistance losses and better heat dissipation. As a result, graphene transistors have the potential to improve performance and efficiency.
- Because the structure is one atom thick, the entire channel is on the surface. As a result, for sensor applications, the channel is directly exposed to the material or environment under test. As a result, some GFETs are extremely sensitive and can be used in a variety of bio- and chemical-sensing applications. It can detect individual molecules detaching from or attaching to a surface, for example.
- Finally, scientists discovered that using a thin, top-gate insulator material improves GFET parameters like open-circuit gain, forward transmission coefficient, and cutoff frequency. As a result, this opens up new opportunities for GFET applications, such as operations at extremely high frequencies. The transistor has the theoretical capability of switching at very high speeds approaching the terahertz range, which is several orders of magnitude faster than silicon-based FETs.
- Traditional semiconductor materials' lattice structure has some limitations that cause them to dissipate more heat at higher frequencies. Graphene, on the other hand, can operate at terahertz frequencies due to its hexagonal lattice structure, high electron mobility, and other factors.

1.2.3.5. GFET Challenges:¹⁶⁵

Inadequate Bandgap: The GFET, even though being one fast and efficient transistor, lacks a bandgap. Because of its gapless structure, the valence and conduction bands meet at zero volts, causing graphene to behave like a metal. In semiconductor materials such as silicon, the two bands are separated by a gap that, under normal conditions, behaves like an

insulator. Normally, electrons need some extra energy to move from the valence band to the conduction band. In FETs, a bias voltage allows current to flow through the band, which acts as an insulator when not biased. Unfortunately, the lack of a band gap in GFET makes it difficult to turn off the transistor because it cannot behave as an open circuit. Several groups are working on solutions to these bandgap issues, including techniques such as the negative resistance approach and fabrication bottom-up synthesis.

Delicate and Expensive Fabrication: The graphene transistor fabrication method differs from that of silicon devices and needs a sensitive, complex, and costly method. The GFET fabrication process starts with the placement of a graphene layer on a silicon wafer, followed by the addition of metal contacts at the ends. Chemical vapor deposition is frequently used by manufacturers to create the graphene layer. The synthesized graphene is then transferred and deposited onto the target SiO_2 substrate via a delamination process. Other steps include building the gate dielectrics, gate contacts, and, eventually, the contact electrodes using the lift-off process or another appropriate method. Impurities and defects in the graphene channel material are frequently introduced by traditional practices. In addition to changing the level of doping, this can cause scattering of charge carriers and degrade electrical performance. Dirac point shifts and low mobility are two specific issues.

Analog Circuit Saturation: Another barrier to widespread GFET adoption is a lack of current saturation, which prevents the transistor from reaching its maximum voltage gain and oscillation frequency in RF applications. Manufacturers can overcome this, however, by optimizing the dielectric material that insulates the top gate. A good dielectric gate material typically provides better control of the carriers in the graphene channel, resulting in improved performance.

1.2.3.6. Application Graphene field effect transistors:

There are five subareas that are important for future graphene applications in electronic and mechanical devices. Photonic components, circuits, and systems The subareas are as follows: 1) Graphene sensors 2) single field-effect transistors, high-frequency RF mixer circuits 3) multiscale modelling of graphene-based transistors; 4) graphene photonics, including plasmonic applications graphene-based terahertz devices as well as graphene-

based photodetectors 5) Additional graphene-based devices as well as applications such as resistive memory, on-chip interconnects, microelectromechanical systems, and other components bioelectronics based on graphene.

1). Graphene sensor: A **diagram 33a** depicting how a graphene sensor could be used as a molecular detector. Graphene is extremely sensitive. Its conductivity is easily affected by the molecules attached to it. In this case, graphene can be used to detect small biological particles. molecules (such as DNA), or even integrated into fire alarms as a security measure System for detecting smoke.¹⁶⁶

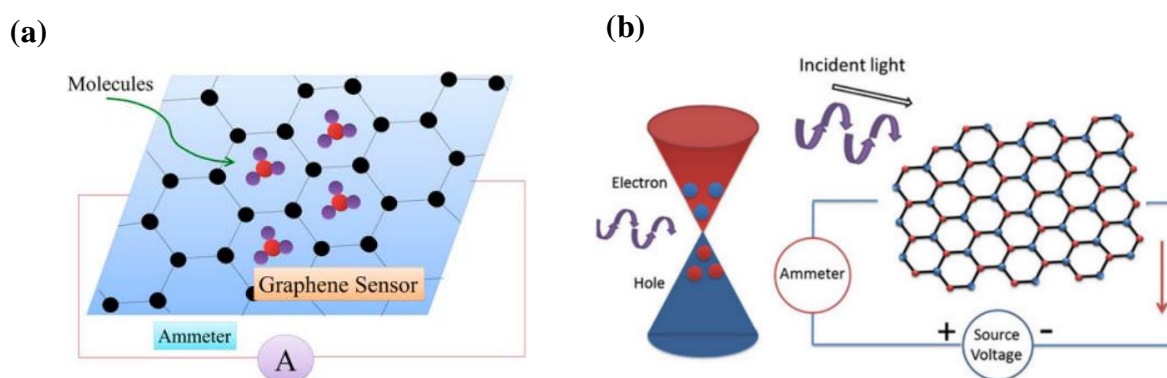


Figure 33: Schematic of graphene sensor,¹⁶⁷ (b) Graphene photodetector.¹⁶⁸



2). Photodiode and Graphene Photodetector: This **diagram 33b** depicts how incident photons can excite electrons in the valence band to the conduction band. Graphene's conductivity rises, and a measurable current can flow throughout the circuit. In practice, the concept can be used to calculate the intensity of incident light. electrons in the valence and conduction bands are referred to as e^{-}_{val} and e^{-}_{con} respectively. According to Bonac-corso¹⁶⁹ *et al.* 2010, the absorption bandwidth of light and the spectrum is determined by the semiconductor used. As previously stated, Graphene interacts with an electromagnetic range that encompasses the majority of the visible spectrum.

3). Graphene Waveguide: A waveguide (**figure 34a**) is a physical channel that traps light and guides it along a set path.⁸² Fiber-optic cable, which has a high refractive index and keeps light inside the fiber, is a common waveguide for sending light signals. The semiconducting substrate is covered with a thin layer of graphene, and either TE or TM wave modes can travel along the graphene film.

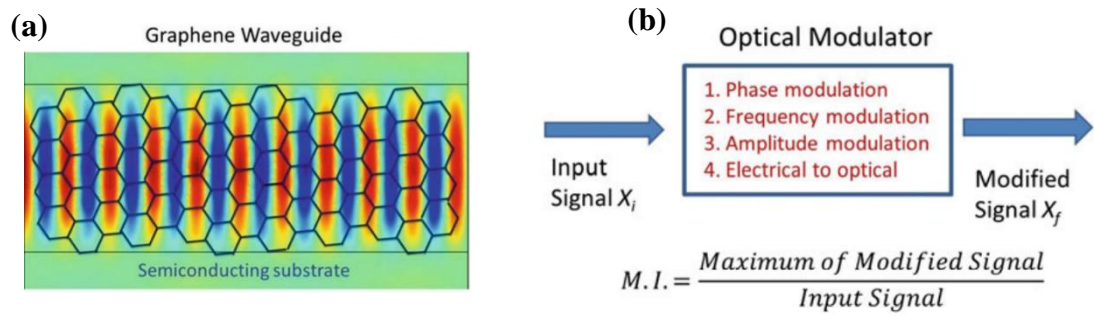


Figure 34: (a) Schematic of graphene waveguide,¹⁷⁰ (b) Optical modulator.¹⁷¹

4). Optical Modulator: The optical modulator (**figure 34b**) is a critical device for converting electrical signals into optical equivalents, serving as an ideal link between electronic and optical devices. This device can also modify the incident wave's properties such as phase, frequency, and amplitude.¹⁷²

5). Transistor: With their high electrical mobility, graphene-based materials are becoming more popular as candidates for future transistors for example: Carbon Nanotube Transistor, Tunneling Transistor has a very quick response time, Furthermore, an ON/OFF switching ratio of up to 10^4 is reported shows memory properties. The upper figure depicts an intermediate barrier that separates the two graphene layers. The Fermi energies are located at the Dirac points in the absence of external electric fields. Whenever the When the gate voltage V_G and the drain-source voltage V_{DS} are applied, electrons start to accumulate in the One graphene layer has a conduction band and the other has holes. Tunneling (**figure 35**) is a possibility in this situation situation by fine-tuning both voltages used to collect electrons and holes in the upper and lower graphene layers, thereby changing the shape of the potential barrier Tunneling is also related to channel length and channel thickness toxic gate oxide layer.^{173,174}

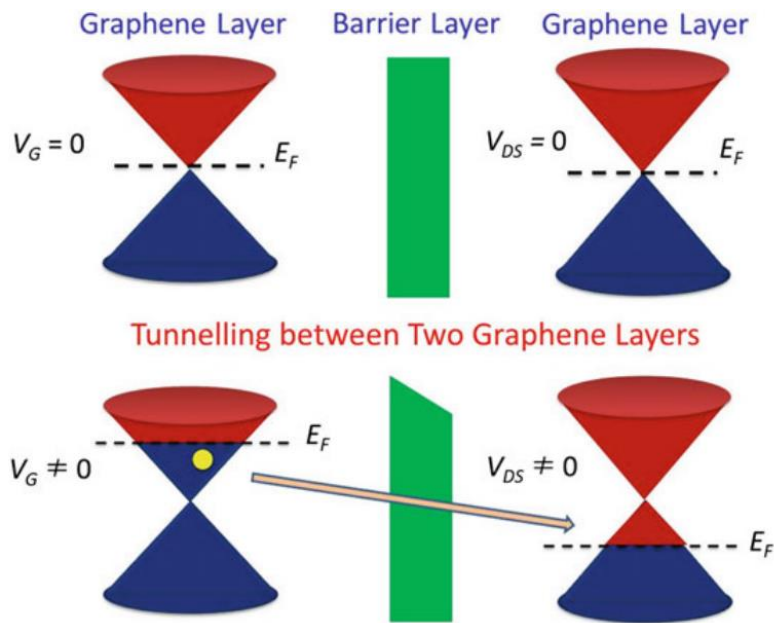


Figure 35: Schematic and working of how tunnelling is done in graphene.^{175,176}

6). High Frequency Devices: High frequency transistors do not require an OFF state and can operate solely on current or voltage variations Graphene could thus be applicable to high-frequency transistors, inverters, or operational amplifiers. The response of graphene to these signals is astounding fast, with operating speeds of a few hundred gigahertz.^{156,169,177}

1.3 Objective of the thesis

My thesis work has particularly explored the materials that give response when illuminated by light of certain wavelength. Experimental and synthesis technique (chapter 2 and 3) and application in microwave switch in SWIR range (chapter 4) and application of CDs in non-volatile optoelectronic memory devices (chapter 5). Last (chapter 6) followed by conclusion and perspective.

Chapter 2 reports the experimental techniques used for optical and structural analysis of the materials UV-Vis, PL, Raman, XRD, SEM, TEM used for. Also, I-V measurement and $R_{ON/OFF}$ by network analyzer has been represented.

Chapter 3 Explores the synthesis of materials and the analysis of materials characterize via different instrument.

Chapter 4 After detailed introduction about materials and technique. Hybrid upconversion Er³⁺-doped NaYF₄ nanocrystal/LT-GaAs photoconductive switch was fabricated. Under a continuous wave $\lambda = 1.55 \mu\text{m}$ laser illumination (power density $\sim 12.9 \text{ mW } \mu\text{m}^{-2}$), thanks to the upconversion energy transfer from the nanocrystals, a more than 2-fold larger value in decibel was measured for the ON/OFF ratio on the hybrid nanocrystal/LT-GaAs device by comparison to the control device without upconversion nanoparticles. A maximum ON/OFF ratio reaching 20.6 dB was measured on the nanocrystal/LT-GaAs hybrid device at an input signal frequency of 20 MHz.

Chapter 5 Here, we address a novel CDs based non-volatile memory with graphene as charge transport layer, storage state induced by optical illumination of UV light (365nm). Through accurate control of the incident light dose, multilevel non-volatile information recording can be found, which is attributed to the huge and firm hole trapping abilities of the CDs induced by the Nitrogen presented in CDs responsible for charge trapping. The device has excellent characteristics, such as a high programming/erasing current $>10^8$.

Chapter 6 Includes a short summary of conclusions observed from the experiments. This chapter also ends with a perspective of experiments which can be done in the future to deeper understanding of systems.

1.4 References

1. Auzel, F. Upconversion and Anti-Stokes Processes with f and d Ions in Solids. *Chemical Reviews* vol. 104 139–173 Preprint at <https://doi.org/10.1021/cr020357g> (2004).
2. Zheng, K. *et al.* Recent advances in upconversion nanocrystals: Expanding the kaleidoscopic toolbox for emerging applications. *Nano Today* vol. 29 Preprint at <https://doi.org/10.1016/j.nantod.2019.100797> (2019).
3. Zheng, K. *et al.* Recent advances in upconversion nanocrystals: Expanding the kaleidoscopic toolbox for emerging applications. *Nano Today* vol. 29 Preprint at <https://doi.org/10.1016/j.nantod.2019.100797> (2019).
4. Fan, Y., Liu, L. & Zhang, F. Exploiting lanthanide-doped upconversion nanoparticles with core/shell structures. *Nano Today* vol. 25 68–84 Preprint at <https://doi.org/10.1016/j.nantod.2019.02.009> (2019).

CHAPTER 1 INTRODUCTION

5. Li, D., Ågren, H. & Chen, G. Near infrared harvesting dye-sensitized solar cells enabled by rare-earth upconversion materials. *Dalton Transactions* vol. 47 8526–8537 Preprint at <https://doi.org/10.1039/c7dt04461e> (2018).
6. Suyver, J. F. *et al.* Novel materials doped with trivalent lanthanides and transition metal ions showing near-infrared to visible photon upconversion. *Opt Mater (Amst)* **27**, 1111–1130 (2005).
7. Zhang, Y. *et al.* Cocrystal engineering for constructing two-photon absorption materials by controllable intermolecular interactions. *J Mater Chem C Mater* **10**, 2562–2568 (2022).
8. Kumar, D. *et al.* A Short Review on Rare Earth Doped NaYF₄ Upconverted Nanomaterials for Solar Cell Applications. *Materials Today: Proceedings* vol. 21 www.sciencedirect.com www.materialstoday.com/proceedings2214-7853 (2020).
9. *214 Topics in Current Chemistry.*
10. Shalav, A., Richards, B. S. & Green, M. A. Luminescent layers for enhanced silicon solar cell performance: Up-conversion. *Solar Energy Materials and Solar Cells* **91**, 829–842 (2007).
11. Dinic, I. Z. *et al.* Compositional and structural dependence of up-converting rare earth fluorides obtained through EDTA assisted hydro/solvothermal synthesis. *Advanced Powder Technology* **28**, 73–82 (2017).
12. Grzechnik, A. *et al.* Hexagonal Na_{1.5}Y_{1.5}F₆ at high pressures. *J Solid State Chem* **165**, 159–164 (2002).
13. Krämer, K. W. *et al.* Hexagonal Sodium Yttrium Fluoride Based Green and Blue Emitting Upconversion Phosphors. *Chemistry of Materials* **16**, 1244–1251 (2004).
14. Li, C. & Lin, J. Rare earth fluoride nano-/microcrystals: Synthesis, surface modification and application. *J Mater Chem* **20**, 6831–6847 (2010).
15. Lingeshwar Reddy, K., Balaji, R., Kumar, A. & Krishnan, V. Lanthanide Doped Near Infrared Active Upconversion Nanophosphors: Fundamental Concepts, Synthesis Strategies, and Technological Applications. *Small* vol. 14 Preprint at <https://doi.org/10.1002/smll.201801304> (2018).
16. Bloembergen N. *SOLID STATE INFRARED QUANTUM COUNTERS 2 PHYSICAL REVIEW LETTERS.* (1959).
17. Chicklis, E., Incorporated, M. & Esterowitz, L. *COMPETITIVE EXCITATION MECHANISMS FOR THE BLUE FLUORESCENCE IN CdF₂:Er³⁺* vol. 21 (1968).

18. Suyver, J. F. *et al.* Upconversion spectroscopy and properties of NaYF₄ doped with Er³⁺, Tm³⁺ and/or Yb³⁺. *J Lumin* **117**, 1–12 (2006).
19. Ghosh Chaudhuri, R. & Paria, S. Core/shell nanoparticles: Classes, properties, synthesis mechanisms, characterization, and applications. *Chemical Reviews* vol. 112 2373–2433 Preprint at <https://doi.org/10.1021/cr100449n> (2012).
20. Ren, W. *et al.* TWEEN coated NaYF₄:Yb,Er/NaYF₄ core/shell upconversion nanoparticles for bioimaging and drug delivery. *RSC Adv* **2**, 7037–7041 (2012).
21. Qiu, P. *et al.* Recent advances in lanthanide-doped upconversion nanomaterials: Synthesis, nanostructures and surface modification. *Nanoscale* **5**, 11512–11525 (2013).
22. Chen, H. *et al.* Plasmon-molecule interactions. *Nano Today* vol. 5 494–505 Preprint at <https://doi.org/10.1016/j.nantod.2010.08.009> (2010).
23. Xiang, H. *et al.* Heavy-Metal-Free Flexible Hybrid Polymer-Nanocrystal Photodetectors Sensitive to 1.5 μm Wavelength. *ACS Appl Mater Interfaces* **11**, 42571–42579 (2019).
24. Ye, S. *et al.* Modulated Visible Light Upconversion for Luminescence Patterns in Liquid Crystal Polymer Networks Loaded with Upconverting Nanoparticles. *Adv Opt Mater* **5**, (2017).
25. Zhou, Y. *et al.* An upconverted photonic nonvolatile memory. *Nat Commun* **5**, (2014).
26. Xu, X. *et al.* Electrophoretic analysis and purification of fluorescent single-walled carbon nanotube fragments. *J Am Chem Soc* **126**, 12736–12737 (2004).
27. Ding, C., Zhu, A. & Tian, Y. Functional surface engineering of C-dots for fluorescent biosensing and in vivo bioimaging. *Acc Chem Res* **47**, 20–30 (2014).
28. Fernando, K. A. S. *et al.* Carbon quantum dots and applications in photocatalytic energy conversion. *ACS Appl Mater Interfaces* **7**, 8363–8376 (2015).
29. Yang, P. *et al.* Pure carbon nanodots for excellent photocatalytic hydrogen generation. *RSC Adv* **5**, 21332–21335 (2015).
30. Cayuela, A., Soriano, M. L., Carrillo-Carrión, C. & Valcárcel, M. Semiconductor and carbon-based fluorescent nanodots: The need for consistency. *Chemical Communications* **52**, 1311–1326 (2016).

31. Zuo, P., Lu, X., Sun, Z., Guo, Y. & He, H. A review on syntheses, properties, characterization and bioanalytical applications of fluorescent carbon dots. *Microchimica Acta* vol. 183 519–542 Preprint at <https://doi.org/10.1007/s00604-015-1705-3> (2016).
32. Li, H., Kang, Z., Liu, Y. & Lee, S. T. Carbon nanodots: Synthesis, properties and applications. *J Mater Chem* **22**, 24230–24253 (2012).
33. Yang, P. *et al.* Pure carbon nanodots for excellent photocatalytic hydrogen generation. *RSC Adv* **5**, 21332–21335 (2015).
34. Cayuela, A., Soriano, M. L. & Valcárcel, M. Photoluminescent carbon dot sensor for carboxylated multiwalled carbon nanotube detection in river water. *Sens Actuators B Chem* 596–601 (2015) doi:10.1016/j.snb.2014.10.102.
35. Sciortino, A., Cannizzo, A. & Messina, F. Carbon Nanodots: A Review—From the Current Understanding of the Fundamental Photophysics to the Full Control of the Optical Response. *C (Basel)* **4**, 67 (2018).
36. Zhou, J., Yang, Y. & Zhang, C. Y. A low-temperature solid-phase method to synthesize highly fluorescent carbon nitride dots with tunable emission. *Chemical Communications* **49**, 8605–8607 (2013).
37. Rong, M. *et al.* Synthesis of highly fluorescent P,O-g-C₃N₄ nanodots for the label-free detection of Cu²⁺ and acetylcholinesterase activity. *J Mater Chem C Mater* **3**, 10916–10924 (2015).
38. Zhu, H. *et al.* Microwave synthesis of fluorescent carbon nanoparticles with electrochemiluminescence properties. *Chemical Communications* 5118–5120 (2009) doi:10.1039/b907612c.
39. Papagiannouli, I. *et al.* Depth Profiling of the Chemical Composition of Free-Standing Carbon Dots Using X-ray Photoelectron Spectroscopy. *Journal of Physical Chemistry C* **122**, 14889–14897 (2018).
40. Bourlinos, A. B. *et al.* Surface functionalized carbogenic quantum dots. *Small* **4**, 455–458 (2008).
41. Zhou, J. *et al.* An electrochemical avenue to blue luminescent nanocrystals from multiwalled carbon nanotubes (MWCNTs). *J Am Chem Soc* **129**, 744–745 (2007).
42. Miao, X. *et al.* Red Emissive Sulfur, Nitrogen Codoped Carbon Dots and Their Application in Ion Detection and Theraonostics. *ACS Appl Mater Interfaces* **9**, 18549–18556 (2017).

43. Zhang, Y. *et al.* Excitation Wavelength Independence: Toward Low-Threshold Amplified Spontaneous Emission from Carbon Nanodots. *ACS Appl Mater Interfaces* **8**, 25454–25460 (2016).
44. Liu, S. *et al.* Hydrothermal treatment of grass: A low-cost, green route to nitrogen-doped, carbon-rich, photoluminescent polymer nanodots as an effective fluorescent sensing platform for label-free detection of Cu(II) ions. *Advanced Materials* **24**, 2037–2041 (2012).
45. Sciortino, A. *et al.* Different natures of surface electronic transitions of carbon nanoparticles. *Physical Chemistry Chemical Physics* **19**, 22670–22677 (2017).
46. Wang, C., Xu, Z. & Zhang, C. Polyethyleneimine-Functionalized Fluorescent Carbon Dots: Water Stability, pH Sensing, and Cellular Imaging. *ChemNanoMat* **1**, 122–127 (2015).
47. Shi, Y. *et al.* Facile synthesis of fluorescent carbon dots for determination of curcumin based on fluorescence resonance energy transfer. *RSC Adv* **5**, 64790–64796 (2015).
48. Wang, Y., Zhu, Y., Yu, S. & Jiang, C. Fluorescent carbon dots: Rational synthesis, tunable optical properties and analytical applications. *RSC Advances* vol. 7 40973–40989 Preprint at <https://doi.org/10.1039/c7ra07573a> (2017).
49. Li, H., Kang, Z., Liu, Y. & Lee, S. T. Carbon nanodots: Synthesis, properties and applications. *J Mater Chem* **22**, 24230–24253 (2012).
50. Wu, Z. L., Liu, Z. X. & Yuan, Y. H. Carbon dots: Materials, synthesis, properties and approaches to long-wavelength and multicolor emission. *Journal of Materials Chemistry B* vol. 5 3794–3809 Preprint at <https://doi.org/10.1039/c7tb00363c> (2017).
51. De, B. & Karak, N. Recent progress in carbon dot-metal based nanohybrids for photochemical and electrochemical applications. *J Mater Chem A Mater* **5**, 1826–1859 (2017).
52. Sciortino, A., Cannizzo, A. & Messina, F. Carbon Nanodots: A Review—From the Current Understanding of the Fundamental Photophysics to the Full Control of the Optical Response. *C (Basel)* **4**, 67 (2018).
53. Qu, S., Wang, X., Lu, Q., Liu, X. & Wang, L. A biocompatible fluorescent ink based on water-soluble luminescent carbon nanodots. *Angewandte Chemie - International Edition* **51**, 12215–12218 (2012).
54. Jiang, L. *et al.* UV–Vis–NIR Full-Range Responsive Carbon Dots with Large Multiphoton Absorption Cross Sections and Deep-Red Fluorescence at Nucleoli and In Vivo. *Small* **16**, (2020).

55. Lecroy, G. E. *et al.* Toward structurally defined carbon dots as ultracompact fluorescent probes. *ACS Nano* **8**, 4522–4529 (2014).
56. Liu, R., Wu, D., Feng, X. & Müllen, K. Bottom-up fabrication of photoluminescent graphene quantum dots with uniform morphology. *J Am Chem Soc* **133**, 15221–15223 (2011).
57. Wang, C. *et al.* A strong blue fluorescent nanoprobe for highly sensitive and selective detection of mercury(II) based on sulfur doped carbon quantum dots. *Mater Chem Phys* **232**, 145–151 (2019).
58. Wu, Z. L., Liu, Z. X. & Yuan, Y. H. Carbon dots: Materials, synthesis, properties and approaches to long-wavelength and multicolor emission. *Journal of Materials Chemistry B* vol. 5 3794–3809 Preprint at <https://doi.org/10.1039/c7tb00363c> (2017).
59. Wu, Z. L. *et al.* One-pot hydrothermal synthesis of highly luminescent nitrogen-doped amphoteric carbon dots for bioimaging from Bombyx mori silk-natural proteins. *J Mater Chem B* **1**, 2868–2873 (2013).
60. Yuan, Y. H. *et al.* Synthesis of nitrogen-doping carbon dots with different photoluminescence properties by controlling the surface states. *Nanoscale* **8**, 6770–6776 (2016).
61. Dong, Y. *et al.* Carbon-based dots co-doped with nitrogen and sulfur for high quantum yield and excitation-independent emission. *Angewandte Chemie - International Edition* **52**, 7800–7804 (2013).
62. Dai, Y. *et al.* Versatile graphene quantum dots with tunable nitrogen doping. *Particle and Particle Systems Characterization* **31**, 597–604 (2014).
63. Zhu, S. *et al.* Highly photoluminescent carbon dots for multicolor patterning, sensors, and bioimaging. *Angewandte Chemie - International Edition* **52**, 3953–3957 (2013).
64. Zong, J. *et al.* Photoluminescence enhancement of carbon dots by gold nanoparticles conjugated via PAMAM dendrimers. *Nanoscale* **5**, 11200–11206 (2013).
65. Liu, C. *et al.* Fluorescence-Converging Carbon Nanodots-Hybridized Silica Nanosphere. *Small* **12**, 4702–4706 (2016).
66. Feng, Y., Zhao, J., Yan, X., Tang, F. & Xue, Q. Enhancement in the fluorescence of graphene quantum dots by hydrazine hydrate reduction. *Carbon N Y* **66**, 334–339 (2014).

67. Li, X., Zhang, S., Kulinich, S. A., Liu, Y. & Zeng, H. Engineering surface states of carbon dots to achieve controllable luminescence for solid-luminescent composites and sensitive Be²⁺ detection. *Sci Rep* **4**, (2014).
68. Liu, M. L., Chen, B. bin, Li, C. M. & Huang, C. Z. Carbon dots: Synthesis, formation mechanism, fluorescence origin and sensing applications. *Green Chemistry* vol. 21 449–471 Preprint at <https://doi.org/10.1039/c8gc02736f> (2019).
69. Jiang, K. *et al.* Red, Green, and Blue Luminescence by Carbon Dots: Full-Color Emission Tuning and Multicolor Cellular Imaging. *Angewandte Chemie* **127**, 5450–5453 (2015).
70. Jia, X., Li, J. & Wang, E. One-pot green synthesis of optically pH-sensitive carbon dots with upconversion luminescence. *Nanoscale* **4**, 5572–5575 (2012).
71. Jiang, K. *et al.* Bright-Yellow-Emissive N-Doped Carbon Dots: Preparation, Cellular Imaging, and Bifunctional Sensing. *ACS Appl Mater Interfaces* **7**, 23231–23238 (2015).
72. Wei, W. *et al.* Non-enzymatic-browning-reaction: A versatile route for production of nitrogen-doped carbon dots with tunable multicolor luminescent display. *Sci Rep* **4**, (2014).
73. Liu, Z. *et al.* Photoluminescence of carbon quantum dots: coarsely adjusted by quantum confinement effects and finely by surface trap states. *Sci China Chem* **61**, 490–496 (2018).
74. Chu, K. W., Lee, S. L., Chang, C. J. & Liu, L. Recent progress of carbon dot precursors and photocatalysis applications. *Polymers* vol. 11 Preprint at <https://doi.org/10.3390/polym11040689> (2019).
75. Wang, X. *et al.* Heteroatom-doped graphene materials: Syntheses, properties and applications. *Chemical Society Reviews* vol. 43 7067–7098 Preprint at <https://doi.org/10.1039/c4cs00141a> (2014).
76. Dong, Y. *et al.* Polyamine-functionalized carbon quantum dots for chemical sensing. *Carbon N Y* **50**, 2810–2815 (2012).
77. Dong, Y. *et al.* Carbon-based dots co-doped with nitrogen and sulfur for high quantum yield and excitation-independent emission. *Angewandte Chemie - International Edition* **52**, 7800–7804 (2013).
78. Chen, H., Kou, X., Yang, Z., Ni, W. & Wang, J. Shape- and size-dependent refractive index sensitivity of gold nanoparticles. *Langmuir* **24**, 5233–5237 (2008).

79. Kozák, O. *et al.* Surfactant-derived amphiphilic carbon dots with tunable photoluminescence. *Journal of Physical Chemistry C* **117**, 24991–24996 (2013).
80. Yu, C., Li, X., Zeng, F., Zheng, F. & Wu, S. Carbon-dot-based ratiometric fluorescent sensor for detecting hydrogen sulfide in aqueous media and inside live cells. *Chemical Communications* **49**, 403–405 (2013).
81. Zhang, T. *et al.* Facilely prepared carbon dots and rare earth ion doped hybrid composites for ratio-metric pH sensing and white-light emission. *RSC Adv* **6**, 61468–61472 (2016).
82. Auston, D. H. Picosecond optoelectronic switching and gating in silicon. *Appl Phys Lett* **26**, 101–103 (1975).
83. Draskovic, D., Raphael, J., Fernandez, O. & Briso-Rodriguez, C. *HIGH ISOLATION SERIES-SHUNT PHOTOCONDUCTIVE MICROWAVE SWITCH*.
84. Smith, F. W. *et al.* Picosecond GaAs-based photoconductive optoelectronic detectors. *Appl Phys Lett* **54**, 890–892 (1989).
85. Krökel, D., Grischkowsky, D. & Ketchen, M. B. Subpicosecond electrical pulse generation using photoconductive switches with long carrier lifetimes. *Appl Phys Lett* **54**, 1046–1047 (1989).
86. Faci, S. *et al.* *Optically Switched Oscillator*.
87. Tripon-Canseliet, C. *et al.* *Electromagnetic modeling and characterization of an optically-controlled microwave phase shifter in GaAs integrated technology*.
88. Pickwell, E. & Wallace, V. P. Biomedical applications of terahertz technology. *Journal of Physics D: Applied Physics* vol. 39 Preprint at <https://doi.org/10.1088/0022-3727/39/17/R01> (2006).
89. Erlig, H., Wang, S., Azfar, T., Fetterman, H. R. & Streit, D. C. *LJ-GaAs detector with 451 fs response at 1.551μm via two-photon absorption*.
90. Tan, K. H. *et al.* 1.55-μm GaNAsSb-based photoconductive switch for microwave switching. *IEEE Photonics Technology Letters* **22**, 1105–1107 (2010).
91. Sicard, M., Thome, K. J., Crowther, B. G. & Smith, M. W. *Shortwave Infrared Spectroradiometer for Atmospheric Transmittance Measurements*.
92. Vidot, J. *et al.* Carbon monoxide from shortwave infrared reflectance measurements: A new retrieval approach for clear sky and partially cloudy atmospheres. *Remote Sens Environ* **120**, 255–266 (2012).

CHAPTER 1 INTRODUCTION

93. Hong, G., Antaris, A. L. & Dai, H. Near-infrared fluorophores for biomedical imaging. *Nature Biomedical Engineering* vol. 1 Preprint at <https://doi.org/10.1038/s41551-016-0010> (2017).
94. Hansen, M. P. & Malchow, D. S. Overview of SWIR detectors, cameras, and applications. in *Thermosense XXX* vol. 6939 69390I (SPIE, 2008).
95. National Research Council (U.S.). Committee on Developments in Detector Technologies. *Seeing photons : progress and limits of visible and infrared sensor arrays*. (National Academies Press, 2010).
96. Mueller, T., Xia, F. & Avouris, P. Graphene photodetectors for high-speed optical communications. *Nat Photonics* **4**, 297–301 (2010).
97. Du, H., Lin, X., Xu, Z. & Chu, D. Recent developments in black phosphorus transistors. *Journal of Materials Chemistry C* vol. 3 8760–8775 Preprint at <https://doi.org/10.1039/c5tc01484k> (2015).
98. transistor -- Britannica Online Encyclopedia.
99. A 77OAPWAW.
100. Street, R. A. Thin-film transistors. *Advanced Materials* **21**, 2007–2022 (2009).
101. Ray-Hua, H. Thin film transistor. *Crystals (Basel)* **9**, (2019).
102. *Fabrication and characterization of thin-film transistors with organic heterostructure of pentacene and PTCDI-C 13*. (2010).
103. Yang, Y., Dang, Z. M., Li, Q. & He, J. Self-Healing of Electrical Damage in Polymers. *Advanced Science* vol. 7 Preprint at <https://doi.org/10.1002/adv.202002131> (2020).
104. Ray-Hua, H. Thin film transistor. *Crystals (Basel)* **9**, (2019).
105. Schroeder, R., Majewski, L. A. & Grell, M. A study of the threshold voltage in pentacene organic field-effect transistors. *Appl Phys Lett* **83**, 3201–3203 (2003).
106. Veres, J., Ogier, S., Lloyd, G. & de Leeuw, D. Gate insulators in organic field-effect transistors. *Chemistry of Materials* vol. 16 4543–4555 Preprint at <https://doi.org/10.1021/cm049598q> (2004).
107. Cai, X. *et al.* N- and P-channel transport behavior in thin film transistors based on tricyanovinyl-capped oligothiophenes. *Journal of Physical Chemistry B* **110**, 14590–14597 (2006).

108. Scheinert, S., Pernstich, K. P., Batlogg, B. & Paasch, G. Determination of trap distributions from current characteristics of pentacene field-effect transistors with surface modified gate oxide. *J Appl Phys* **102**, (2007).
109. Kawase, T., Shimoda, T., Newsome, C., Sirringhaus, H. & Friend, R. H. Inkjet printing of polymer thin film transistors. in *Thin Solid Films* vols 438–439 279–287 (2003).
110. Zaumseil, J. & Sirringhaus, H. Electron and ambipolar transport in organic field-effect transistors. *Chemical Reviews* vol. 107 1296–1323 Preprint at <https://doi.org/10.1021/cr0501543> (2007).
111. Tsumura, A., Koezuka, H. & Ando, T. Macromolecular electronic device: Field-effect transistor with a polythiophene thin film. *Appl Phys Lett* **49**, 1210–1212 (1986).
112. Ebisawa, F., Kurokawa, T. & Nara, S. Electrical properties of polyacetylene/polysiloxane interface. *J Appl Phys* **54**, 3255–3259 (1983).
113. Frank, D. J. *et al.* Device scaling limits of Si MOSFETs and their application dependencies. *Proceedings of the IEEE* **89**, 259–287 (2001).
114. Figer, D. F. An upper limit to the masses of stars. *Nature* **434**, 192–194 (2005).
115. Tulevski, G. S., Nuckolls, C., Afzali, A., Graham, T. O. & Kagan, C. R. Device scaling in sub-100 nm pentacene field-effect transistors. *Appl Phys Lett* **89**, (2006).
116. Haddock, J. N. *et al.* A comprehensive study of short channel effects in organic field-effect transistors. *Org Electron* **7**, 45–54 (2006).
117. Li, D. & Guo, L. J. Organic thin film transistors and polymer light-emitting diodes patterned by polymer inking and stamping. *J Phys D Appl Phys* **41**, (2008).
118. Naber, R. C. G. *et al.* High-performance solution-processed polymer ferroelectric field-effect transistors. *Nat Mater* **4**, 243–248 (2005).
119. Zhu, Z., Guo, Y. & Liu, Y. Application of organic field-effect transistors in memory. *Materials Chemistry Frontiers* vol. 4 2845–2862 Preprint at <https://doi.org/10.1039/d0qm00330a> (2020).
120. Zhou, F., Chen, J., Tao, X., Wang, X. & Chai, Y. 2D Materials Based Optoelectronic Memory: Convergence of Electronic Memory and Optical Sensor. *Research* **2019**, 1–17 (2019).
121. Zhou, L. *et al.* Recent Advances of Flexible Data Storage Devices Based on Organic Nanoscaled Materials. *Small* vol. 14 Preprint at <https://doi.org/10.1002/sml.201703126> (2018).

122. Ren, Y. *et al.* Recent Advances in Ambipolar Transistors for Functional Applications. *Advanced Functional Materials* vol. 29 Preprint at <https://doi.org/10.1002/adfm.201902105> (2019).
123. Jiang, A. Q. *et al.* Ferroelectric domain wall memory with embedded selector realized in LiNbO₃ single crystals integrated on Si wafers. *Nat Mater* **19**, 1188–1194 (2020).
124. Yang, N. *et al.* Nonvolatile Negative Optoelectronic Memory Based on Ferroelectric Thin Films. *ACS Appl Electron Mater* **2**, 1035–1040 (2020).
125. Lin, Y., Li, G., Yu, P., Ercan, E. & Chen, W. Organic liquid crystals in optoelectronic device applications: Field-effect transistors, nonvolatile memory, and photovoltaics. *Journal of the Chinese Chemical Society* (2022) doi:10.1002/jccs.202200061.
126. Wang, J. *et al.* Deep-ultraviolet-triggered neuromorphic functions in In-Zn-O phototransistors. *Appl Phys Lett* **113**, (2018).
127. Ercan, E., Chen, J. Y., Shih, C. C., Chueh, C. C. & Chen, W. C. Influence of polymeric electrets on the performance of derived hybrid perovskite-based photo-memory devices. *Nanoscale* **10**, 18869–18877 (2018).
128. Jin, R., Shi, K., Qiu, B. & Huang, S. Photoinduced-reset and multilevel storage transistor memories based on antimony-doped tin oxide nanoparticles floating gate. *Nanotechnology* **33**, (2022).
129. Carroli, M. *et al.* Multiresponsive Nonvolatile Memories Based on Optically Switchable Ferroelectric Organic Field-Effect Transistors. *Advanced Materials* **33**, (2021).
130. Ling, H. *et al.* Effect of thickness of polymer electret on charge trapping properties of pentacene-based nonvolatile field-effect transistor memory. *Org Electron* **43**, 222–228 (2017).
131. Yu, Y. *et al.* Small-Molecule-Based Organic Field-Effect Transistor for Nonvolatile Memory and Artificial Synapse. *Advanced Functional Materials* vol. 29 Preprint at <https://doi.org/10.1002/adfm.201904602> (2019).
132. Lin, Y. S. *et al.* Liquid Crystalline Rylenediimides with Highly Order Smectic Layer Structure as a Floating Gate for Multiband Photoresponding Photonic Transistor Memory. *Adv Electron Mater* **8**, (2022).
133. Chang, H. C., Liu, C. L. & Chen, W. C. Flexible nonvolatile transistor memory devices based on one-dimensional electrospun P3HT: Au hybrid nanofibers. *Adv Funct Mater* **23**, 4960–4968 (2013).

134. Zhou, Y. *et al.* Real-time storage of thermal signals in organic memory with floating core-shell nanoparticles. *J Mater Chem C Mater* **5**, 8415–8423 (2017).
135. Chiu, Y. C. *et al.* Oligosaccharide Carbohydrate Dielectrics toward High-Performance Non-volatile Transistor Memory Devices. *Advanced Materials* **27**, 6257–6264 (2015).
136. Jeong, Y. J., Yun, D. J., Noh, S. H., Park, C. E. & Jang, J. Surface modification of CdSe quantum-dot floating gates for advancing light-erasable organic field-effect transistor memories. *ACS Nano* **12**, 7701–7709 (2018).
137. Yan, C., Wen, J., Lin, P. & Sun, Z. A Tunneling Dielectric Layer Free Floating Gate Nonvolatile Memory Employing Type-I Core–Shell Quantum Dots as Discrete Charge-Trapping/Tunneling Centers. *Small* **15**, (2019).
138. Ling, H. *et al.* Synergistic Effects of Self-Doped Nanostructures as Charge Trapping Elements in Organic Field Effect Transistor Memory. *ACS Appl Mater Interfaces* **8**, 18969–18977 (2016).
139. Lv, Z. *et al.* Semiconductor Quantum Dots for Memories and Neuromorphic Computing Systems. *Chemical Reviews* vol. 120 3941–4006 Preprint at <https://doi.org/10.1021/acs.chemrev.9b00730> (2020).
140. Wang, Y. *et al.* Photonic Synapses Based on Inorganic Perovskite Quantum Dots for Neuromorphic Computing. *Advanced Materials* **30**, (2018).
141. Yang, Y. *et al.* Hot Carrier Trapping Induced Negative Photoconductance in InAs Nanowires toward Novel Nonvolatile Memory. *Nano Lett* **15**, 5875–5882 (2015).
142. Rios, C. *et al.* Integrated all-photonic non-volatile multi-level memory. *Nat Photonics* **9**, 725–732 (2015).
143. Ling, H. *et al.* Electrolyte-gated transistors for synaptic electronics, neuromorphic computing, and adaptable biointerfacing. *Applied Physics Reviews* vol. 7 Preprint at <https://doi.org/10.1063/1.5122249> (2020).
144. Sun, Z., Li, J., Liu, C., Yang, S. & Yan, F. Trap-Assisted Charge Storage in Titania Nanocrystals toward Optoelectronic Nonvolatile Memory. *Nano Lett* **21**, 723–730 (2021).
145. Star, A., Lu, Y., Bradley, K. & Grüner, G. Nanotube optoelectronic memory devices. *Nano Lett* **4**, 1587–1591 (2004).
146. Han, S. T. *et al.* CdSe/ZnS core-shell quantum dots charge trapping layer for flexible photonic memory. *J Mater Chem C Mater* **3**, 3173–3180 (2015).

147. Zhou, Y. *et al.* An upconverted photonic nonvolatile memory. *Nat Commun* **5**, (2014).
148. Yung, K. C., Wu, W. M., Pierpoint, M. P. & Kusmartsev, F. v. Introduction to graphene electronics - a new era of digital transistors and devices. *Contemporary Physics* vol. 54 233–251 Preprint at <https://doi.org/10.1080/00107514.2013.833701> (2013).
149. Novoselov, K. S. *et al.* *Electric Field Effect in Atomically Thin Carbon Films*. *Phys. Rev. Lett* vol. 404 <http://science.sciencemag.org/> (2000).
150. O’Hare, A., Kusmartsev, F. v. & Kugel, K. I. A stable ‘flat’ form of two-dimensional crystals: Could graphene, silicene, germanene be minigap semiconductors? *Nano Lett* **12**, 1045–1052 (2012).
151. Novoselov, K. S. *et al.* *Electric Field Effect in Atomically Thin Carbon Films*. *Phys. Rev. Lett* vol. 404 <http://science.sciencemag.org/> (2000).
152. Katsnelson, M. I. *Graphene: carbon in two dimensions A two-dimensional form of carbon*. (2007).
153. Schwierz, F. Graphene transistors. *Nature Nanotechnology* vol. 5 487–496 Preprint at <https://doi.org/10.1038/nnano.2010.89> (2010).
154. Geim, A. K. *Graphene: Status and Prospects*. <http://science.sciencemag.org/>.
155. NISTEP-STT037E-76 (1).
156. Yung, K. C., Wu, W. M., Pierpoint, M. P. & Kusmartsev, F. v. Introduction to graphene electronics - a new era of digital transistors and devices. *Contemporary Physics* vol. 54 233–251 Preprint at <https://doi.org/10.1080/00107514.2013.833701> (2013).
157. Geim, A. K. *Graphene: Status and Prospects*. <http://science.sciencemag.org/>.
158. Yung, K. C., Wu, W. M., Pierpoint, M. P. & Kusmartsev, F. v. Introduction to graphene electronics - a new era of digital transistors and devices. *Contemporary Physics* vol. 54 233–251 Preprint at <https://doi.org/10.1080/00107514.2013.833701> (2013).
159. Wallace, P. R. & Ace, P. R. W. *The Band Theory of Graphite*. vol. 71 (1947).
160. Pumarol, M. E. *et al.* Direct nanoscale imaging of ballistic and diffusive thermal transport in graphene nanostructures. *Nano Lett* **12**, 2906–2911 (2012).
161. Yang, L., Park, C. H., Son, Y. W., Cohen, M. L. & Louie, S. G. Quasiparticle energies and band gaps in graphene nanoribbons. *Phys Rev Lett* **99**, (2007).

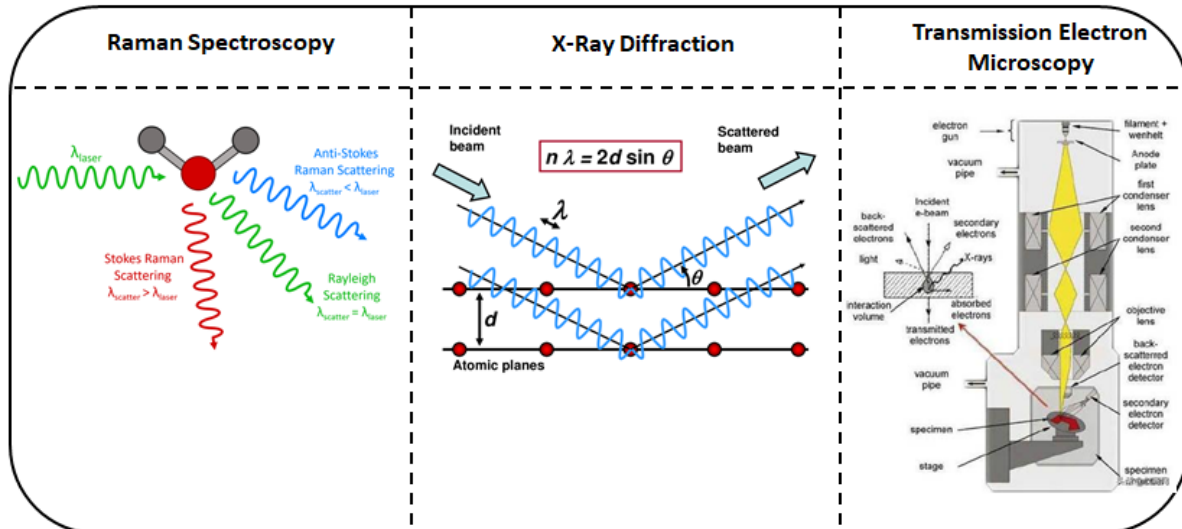
162. Papageorgiou, D. G., Kinloch, I. A. & Young, R. J. Mechanical properties of graphene and graphene-based nanocomposites. *Progress in Materials Science* vol. 90 75–127 Preprint at <https://doi.org/10.1016/j.pmatsci.2017.07.004> (2017).
163. Viola Kusminskiy, S., Campbell, D. K. & Castro Neto, A. H. Lenosky's energy and the phonon dispersion of graphene. *Phys Rev B Condens Matter Mater Phys* **80**, (2009).
164. Schwierz, F. Graphene transistors. *Nature Nanotechnology* vol. 5 487–496 Preprint at <https://doi.org/10.1038/nnano.2010.89> (2010).
165. Schwierz, F. Graphene transistors: Status, prospects, and problems. *Proceedings of the IEEE* **101**, 1567–1584 (2013).
166. He, Q., Wu, S., Yin, Z. & Zhang, H. Graphene-based electronic sensors. *Chemical Science* vol. 3 1764–1772 Preprint at <https://doi.org/10.1039/c2sc20205k> (2012).
167. He, Q., Wu, S., Yin, Z. & Zhang, H. Graphene-based electronic sensors. *Chemical Science* vol. 3 1764–1772 Preprint at <https://doi.org/10.1039/c2sc20205k> (2012).
168. Bonaccorso, F., Sun, Z., Hasan, T. & Ferrari, A. C. Graphene photonics and optoelectronics. *Nat Photonics* **4**, 611–622 (2010).
169. Bonaccorso, F., Sun, Z., Hasan, T. & Ferrari, A. C. Graphene photonics and optoelectronics. *Nat Photonics* **4**, 611–622 (2010).
170. Wu, Q., Turpin, J. P. & Werner, D. H. Integrated photonic systems based on transformation optics enabled gradient index devices. *Light Sci Appl* **1**, (2012).
171. Xing, F. *et al.* Sensitive real-time monitoring of refractive indexes using a novel graphene-based optical sensor. *Sci Rep* **2**, (2012).
172. Xing, F. *et al.* Sensitive real-time monitoring of refractive indexes using a novel graphene-based optical sensor. *Sci Rep* **2**, (2012).
173. Michetti, P., Cheli, M. & Iannaccone, G. Model of tunneling transistors based on graphene on SiC. *Appl Phys Lett* **96**, (2010).
174. Ponomarenko, L. A. *et al.* Tunable metalinsulator transition in double-layer graphene heterostructures. *Nat Phys* **7**, 958–961 (2011).
175. Michetti, P., Cheli, M. & Iannaccone, G. Model of tunneling transistors based on graphene on SiC. *Appl Phys Lett* **96**, (2010).

CHAPTER 1 INTRODUCTION

176. Ponomarenko, L. A. *et al.* Tunable metalinsulator transition in double-layer graphene heterostructures. *Nat Phys* **7**, 958–961 (2011).
177. Zheng, J. *et al.* Sub-10 nm gate length graphene transistors: Operating at terahertz frequencies with current saturation. *Sci Rep* **3**, (2013).

Chapter 2

Experimental Methods and Characterizations



Resume

Ce chapitre traite de la synthèse et des techniques de caractérisation utilisées pour préparer et analyser les nanocristaux de $\text{NaYF}_4:\text{Er}^{3+}$ et les points de carbone ainsi que la procédure de transfert de graphène monocouche. La synthèse des nanomatériaux choisie dans ce travail est la voie de la co-précipitation. Le dépôt des électrodes a été effectué par la technique PVD respectivement. Les nanomatériaux ainsi préparés ont été soumis à une caractérisation structurale, optique et électrique approfondie. Les techniques de caractérisation comprennent la diffraction des rayons X, la microscopie électronique à balayage, la microscopie électronique à transmission et le Raman.

2.1 Graphene transfer mechanism

2.1.1. Procedure of cleaning Si/SiO₂ substrate

The silicon substrate was cleaned by first washing it in DI water for 15 minutes, then cleaning it with Acetone and then Isopropanol (IPA). After cleaning the substrate, it was treated for 5 minutes with oxygen plasma.

2.1.2. Procedure of Graphene Transfer

In order to transfer the graphene layer,⁵ as shown in **figure 1** a solution of PMMA (40mg/mL) was made in 1mL of butyl-acetate. On top of Cu foil, the solution was spin coated at 2000rpm for 120 seconds and heated for 30 minutes at 80°C. Cu foil cut in small strips and was carefully placed on the surface of the etchant and left until the Cu foil was completely dissolved by the etchant, leaving the PMMA/graphene film floating on the solution's surface. To pick up the floating film, a glass slide was submerged in the solution. For 10 minutes, the film was kept near the surface of DI water to wash away any remaining solutions. This washing procedure was repeated three times. The desired substrate was then carefully dipped into water to pick up the floating film, resulting in a smooth PMMA/graphene film attached to the substrate's surface. When heated for >12 h at 150 ° C, the PMMA/graphene layer adhered well to the substrate. After cooling, the PMMA was quickly removed by rinsing three times with acetone, leaving graphene/substrate. Finally, 100nm thick gold electrode with length/width of 2.5/3mm was deposited to make a graphene transistor.

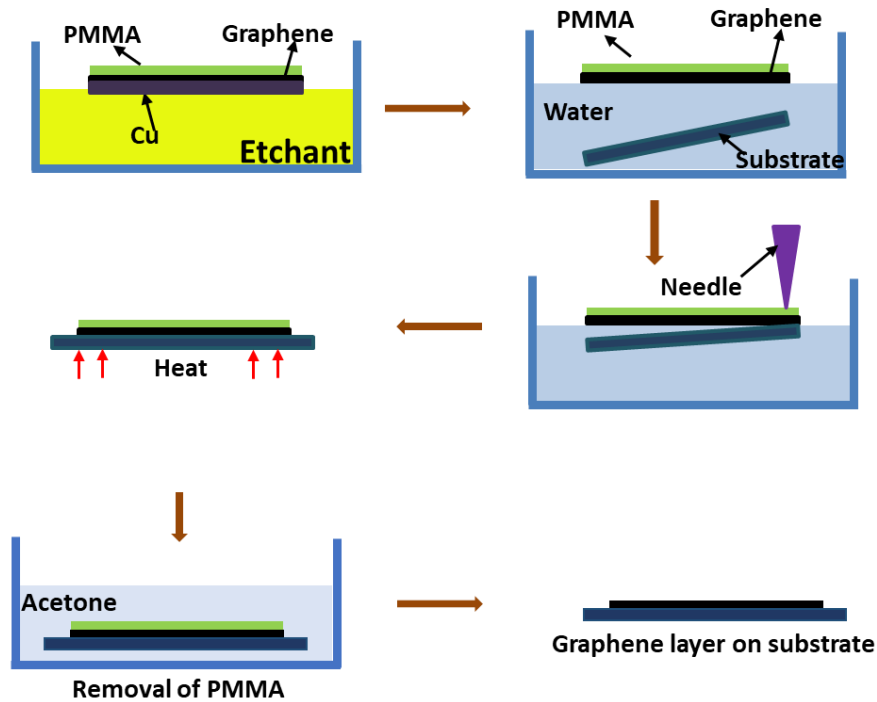


Figure 1: Schematic of wet transfer procedure of graphene film.

2.1.3. Preparation of GaAs and low-temperature grown GaAs photoconductive switch

LT-GaAs layer on a bulk GaAs substrate was grown using a standard MBE method and post annealing on which 150 nm thick gold electrodes (with 10 nm thick Ti adhesive layer) were then defined by E-beam lithography to complete the photoconductive switch fabrication. Er³⁺-doped NaYF₄ nanocrystals were first dispersed in isopropanol with the help of sonication and such solution was then drop-cast onto the surface of the above-mentioned LT-GaAs photoconductive switches. This work is done in the collaboration with the previous PhD student Hengyang of our group.

2.2 Deposition Technique

2.2.1 Thermal evaporation of source and Drain electrode

One of the most common deposition methods is thermal evaporation. It is one type of Physical vapor deposition (PVD) method for depositing a thin film (**figure 2**). In this method the target materials are heated by the passage of an electric current inside an evaporation source (boat, coil, and basket) this source contains target material inside it. The target material is heated to the evaporation point. Because heat is generated by electrical resistance of the evaporation source also known as resistive evaporation. Following evaporation, the atoms/molecules of target materials migrate to the substrate and a thin film is formed on its surface. The entire evaporation process must be done under a high vacuum i.e., 1×10^{-6} mbar, Because of the high vacuum, vaporized material can pass through the vacuum chamber without colliding with other gas molecules/atoms and finally nucleating on the target surface. A quartz crystal vibrating at a particular frequency is calibrated and used to measure the rate of evaporation. After stabilizing the evaporation temperature, the substrate is rotated to get uniform and dense film. With tolerances of less than 1nm, high vacuum thermal evaporation provides precise control of film thickness.

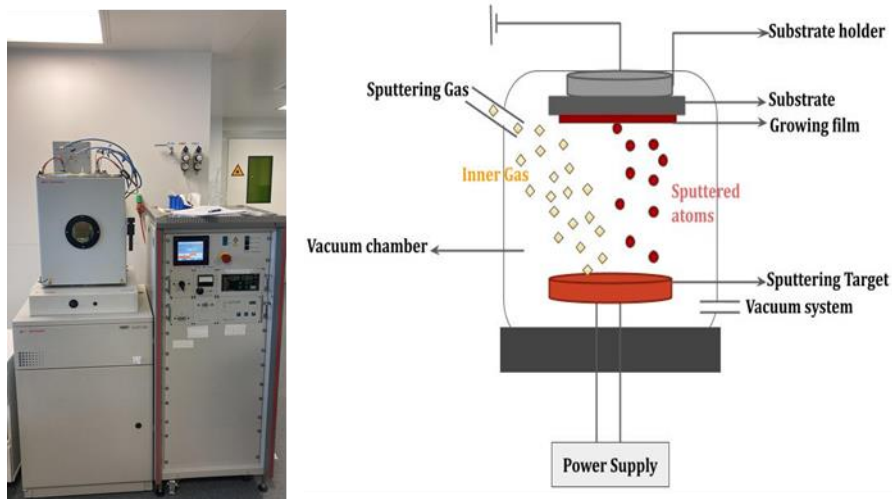


Figure 2: Schematic of thermal evaporation instrument.

2.2.2. Procedure of making thin film of CDs and NaYF₄: Er³⁺

Few μl of colloidal solution of nanocrystals was drop casted on the gap between 2 electrodes and left for drying in air until completely dried (**figure 3**). In order to get accurate readings, the device was then placed in vacuum for a number of hours.

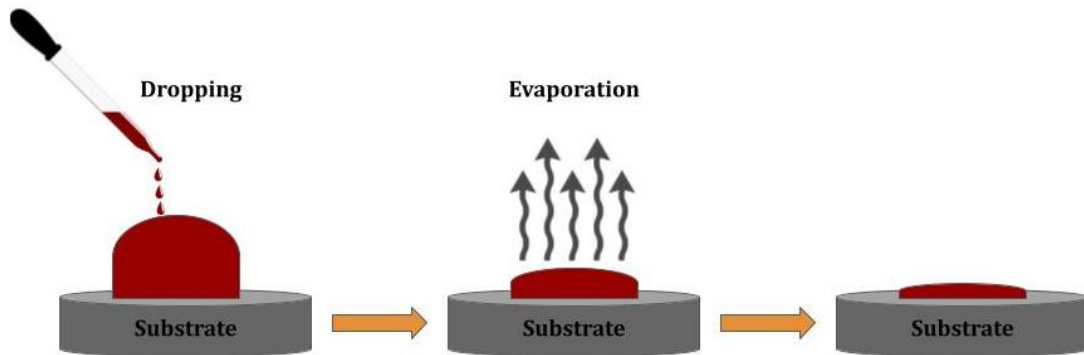


Figure 3: Schematic of making film by drop cast method.

2.3 Characterization Section

2.3.1. Structural and Optical Characterization

2.3.1.1 Atomic Force microscopy (AFM)

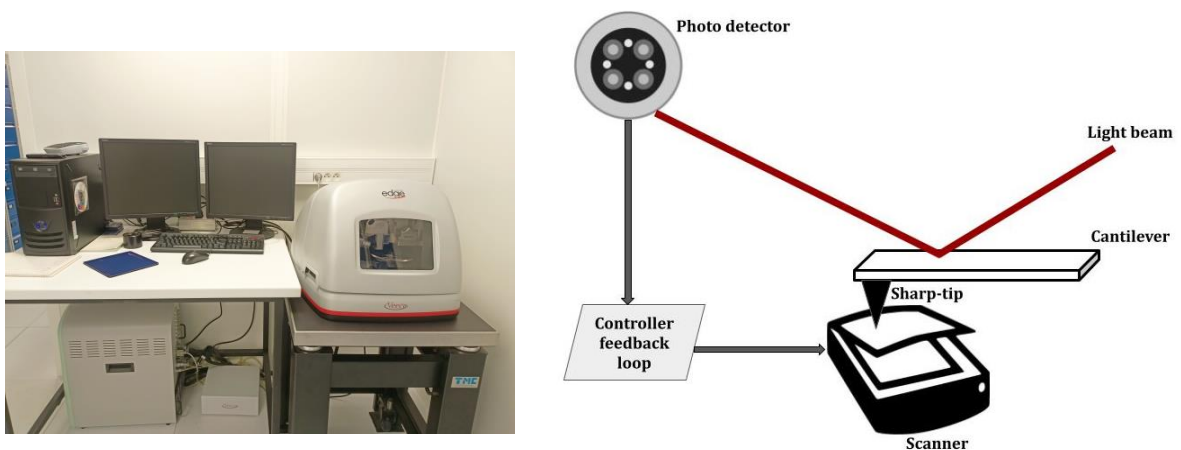


Figure 4: Schematic of Atomic Force Microscope (AFM).

AFM was performed using a dimension Icon from Bruker operating in non-contact mode with high-resolution probes (radius: 2nm) from Next-tip (**figure 4**). It is an imaging technique that uses a cantilever beam having sharp tip at the end. The commonly used materials for cantilever are Si or Si Nitride. Principle is explained by Hook's law which states that bringing the tip close to the test sample/specimen the contact between the sample surfaces deflects the cantilever. With appropriate data computation and processing, a 3D image of the sample surface can be formed and hence the surface topography can be determined. AFM produce 3D profile of the surface and there is no requirement of additional sample preparation. It can be used in ambient environment and even in liquid.

2.3.1.2 Scanning Electron Microscopy (SEM) and Energy Dispersive X-ray Spectroscopy

SEM Characterization was performed by FEI Magellan 400 system with a standard field emission gun source equipped with a EDX detector. The measurement is done on the surfaces of film by focusing and scanning specimens/films with beam of electrons moving at low energy. It operates on the principle of using kinetic energy to generate signals from electron interactions (**figure 5**). These electrons are diffracted backscattered electrons, secondary electrons and backscattered electrons used to view crystallized elements. An image is created by using secondary and backscattered electrons. Secondary electrons emitted from the specimen are responsible for detecting the topography and morphology of the specimen, whereas contrast of test sample elements is shown by backscattered electron.

Furthermore, the SEM is equipped with energy dispersive X-ray spectroscopy (EDX) which is used for elemental analysis of materials. A microanalysis system is capable of quantification and chemical mapping of different elements of the test sample. It shows the energy and intensity distribution of the electron's X-ray signals beam as hit the sample's surface. As a result, EDX is used to calculate chemical composition of the materials down to few micrometres in size. The apparatus can be used generate elemental composition maps on wide range of materials. We used EDX to examine, N-doped CDs to examine N, C, O in the material.

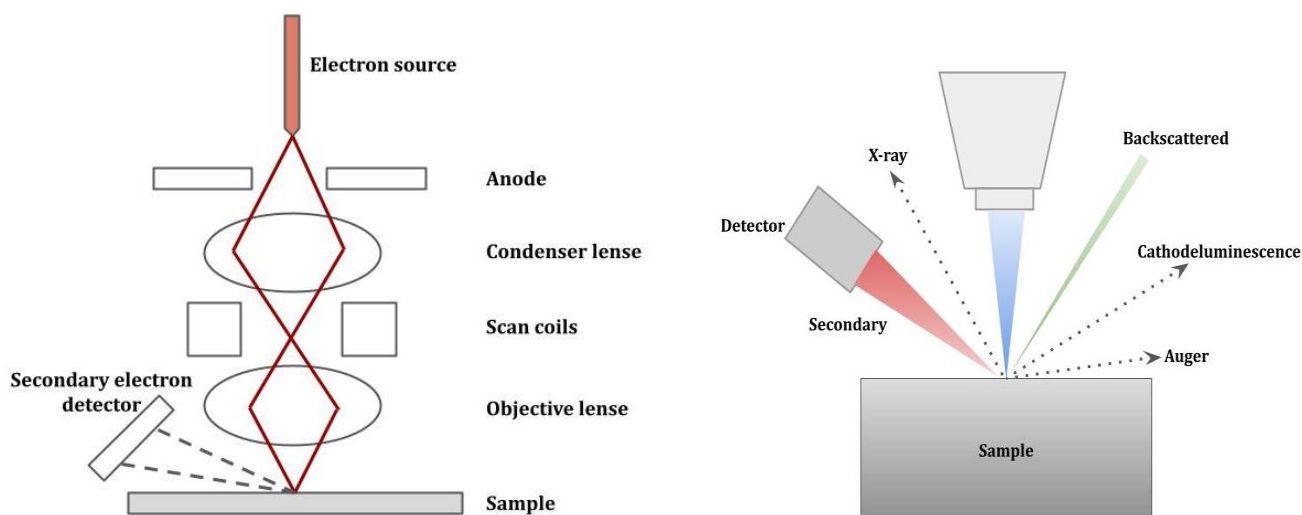


Figure 5: Schematic of Scanning electron Microscope.

2.3.1.3 Transmission electron microscope (TEM)

TEM is an advanced but sophisticated technique that employs and accelerated electron beam, we use this beam to visualize very small samples and create a highly magnified image and therefore structure and morphology can be analysed. The basic working principle same as light microscope, but TEM uses electron beam rather than light. We drop the CDs solution onto the carbon coated grid and let it dry. Then TEM is uses to study the size, morphology, composition and quality of the material.

2.3.1.4 UV-Visible spectroscopy

In this spectrum was measured by absorption mode by an Ocean Optics HL-2000 fibre-coupled tungsten halogen lamp and an Ocean Optics HR4000 spectrometer (200-1100 nm) (**figure 6**). UV-Vis spectroscopy is a technique that interprets electromagnetic radiation absorbed or emitted when molecules, atoms or ions change its energy states. In this spectroscopy particularly ultra-violet region (200-400 nm) is absorbed by the molecule.

UV-Vis spectroscopy is concerned with interaction of light with matter. When light is absorbed by matter, the energy content of atom or molecule increases and causing electron excitation to higher energy levels. Molecules with π -electrons or nonbonding electrons excited to higher anti-bonding molecular orbitals by absorbing energy in the form of UV

light. The longer the wavelength of light electron absorb more easily it can be excited. This absorption of UV light by the chemical compounds produces a unique spectrum that helps in the compound identification .

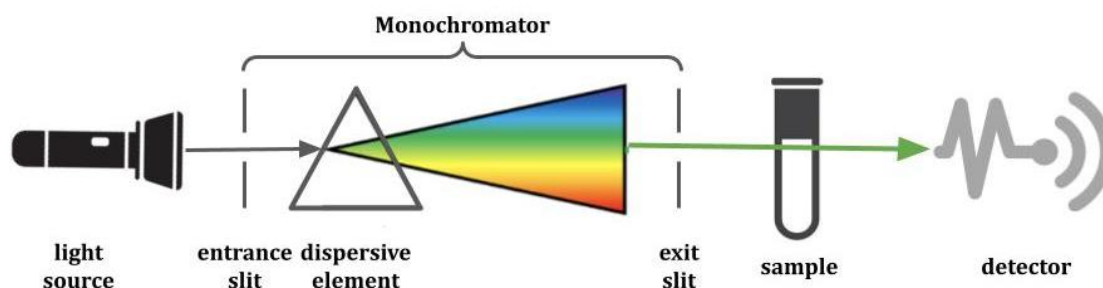


Figure 6: Schematic of UV-Vis Spectroscopy.

2.3.1.5 Photoluminescence (PL)

Steady-state photoluminescence (PL) was recorded in a reflection mode by same Ocean Optics spectrometer with an excitation source at 365 nm (Ocean Optics LLS-365) shown in **figure 7**. Rhodamine B solution in ethanol was used as control standard. The quantum yield (QY) of CDs were estimated by slope method.^{1,7} By comparing the intensity of integrated photoluminescence and absorbance value [many values (less than 0.1 at excitation wavelength) gave the curve] comparing the samples to the references. The used equation is:

$$\Phi_x = \Phi_{st} \left(\frac{K_x}{K_{st}} \right) \left(\frac{\eta_x}{\eta_{st}} \right)^2$$

Where Φ is the QY, K is the slope value determined by the curve and η is the refractive index. The subscript "x" refers to the Carbon dots and "st" refers to the standard reference samples. For aqueous solutions, $\frac{\eta_x}{\eta_{st}} = 1$.

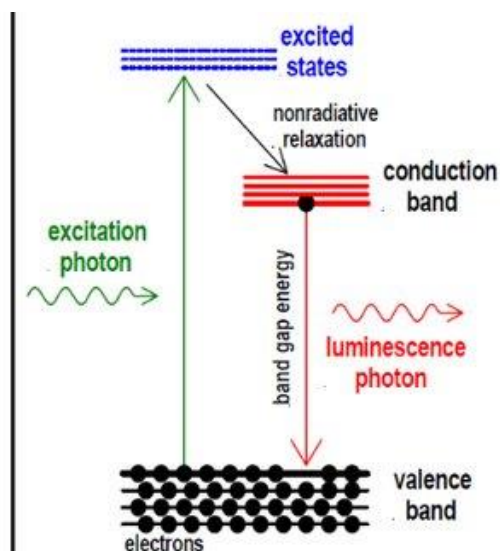


Figure 7: Photoluminescence instrument

2.3.1.6 Time resolved Photoluminescence (TRPL)

Fluorescence lifetime of material in nanosecond were measured by the time correlated single-photon counting (TCSPC) system. Ocean Optics spectrometer with an excitation source at 365 nm (Ocean Optics LLS-365, repetition rate 6 MHz) was use to excite the sample.

TRPL is the preferred method to study fast electronic deactivation process that led to photon emission, also known as fluorescence. The molecules in its lowest excited state typically ranges from few picoseconds to nanoseconds. The surroundings environment of molecules for example solvent, presence of quenchers or interaction with other molecules can affect the fluorescence lifetime.

In TCSPC, the time between sample excited by pulsed laser and the arrival of the emitted photon to the detector is measured. TCSPC needs a well-defined “start” signal, which is provided by laser pulse or photodiode, and also defined “stop” signal, which is measured by detection with single-photon sensitive detectors. This delay time is measured many times to check statistical nature of fluorophore emission. The delay times are organized into histogram, which plots the occurrence of emission after the excitation pulse over time. The PL decay curves are analyzed by fitting the following:

$$y = A_1 \cdot \exp(-x/\tau_1) + A_2 \cdot \exp(-x/\tau_2) + y_0 \quad (1)$$

The average lifetime can be calculated as follow:

$$\tau_{av} = \frac{\alpha_1 \tau_1^2 + \alpha_2 \tau_2^2}{\alpha_1 \tau_1 + \alpha_2 \tau_2} \quad (2)$$

2.3.1.7. Fluorescence experiment

This were performed by reflection mode on Er³⁺-doped NaYF₄ nanocrystals deposited on a glass substrate with an excitation source of source at the wavelength of $\lambda = 1.5 \mu\text{m}$ achieved by a single mode pigtailed laser diode (45 mW). Fluorescence was recorded by an Ocean Optics HR4000 spectrometer with an optical fibre. Fluorescence quantum yield measurements were performed on nanocrystal powders deposited on a home-made holder with an integrating sphere by a method established previously⁸ and recorded simultaneously by two spectrometers (Ocean Optics HR4000 spectrometer and Ocean Optics NIR-Quest 256 spectrometer). Kubelka–Munk function was calculated from the diffuse reflectance spectra obtained on nanocrystal powders deposited on a glass substrate measured by an Ocean Optics reflectance probe together with a Spectral on diffuse reflectance standard, a fibre-coupled tungsten halogen light source, and an Ocean Optics HR4000 spectrometer (for visible spectrum measurements) or an Ocean Optics NIR-Quest 256 spectrometer (for infrared spectrum measurements).

2.3.1.8. Raman Spectroscopy

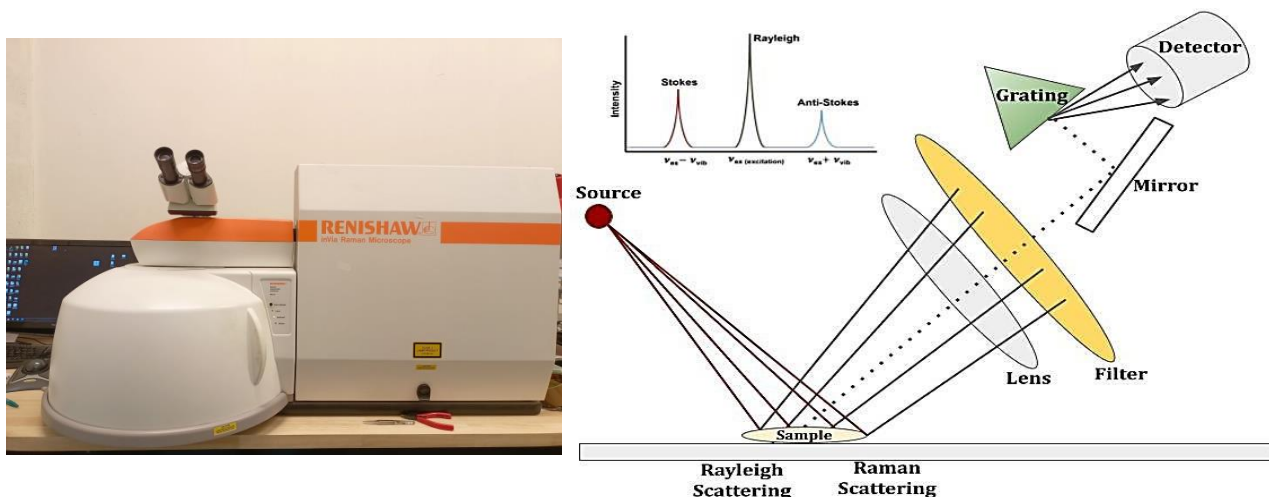


Figure 8: Schematic of Raman Spectra

The Raman spectrometer is a Renishaw InVia in backscattered configuration with a 532nm laser with back backscattering/reflection. Raman spectroscopy is a promising technique for determining molecular structure that is used in conjunction with infrared spectroscopy. Raman spectra are obtained by exciting a sample with a high-intensity laser beam and passing the scattered light through a spectrometer **shown in figure 8**. The Raman shift is the difference in energy between incident and scattered light. The vertical axis in the resulting spectrum represents the intensity of the scattered light, and the horizontal axis represents the Raman shift wavenumber (cm^{-1}).

2.3.1.9. X-ray Diffraction (XRD)

XRD spectrum was obtained by a PANalytical X'Pert X-ray diffractometer using $\text{Cu-K}\alpha$ radiation. XRD shown in **figure 9** used to analyse the diffraction pattern of a material to obtain information about its composition, structure or morphology of atoms or molecules. In general energy conversion are divided into three sections. When the scattered X-rays have same wavelength as the incident X-rays, diffraction occurs, i.e., the difference in optical range between crystal planes is an integer multiple of the wavelength. The diffraction pattern is compared using the standard diffraction pattern and specific to each crystal substance. The phase presents in the sample can be identified using three strong

peaks. Diffractometers for XRD are widely used to measure bulk materials such as single crystals, powders, liquids and polycrystals or crystals. It has advantage of quick detection, simple operation, and process data easily.

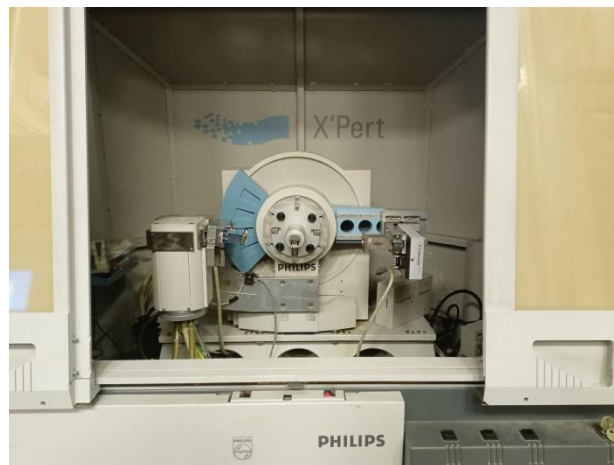
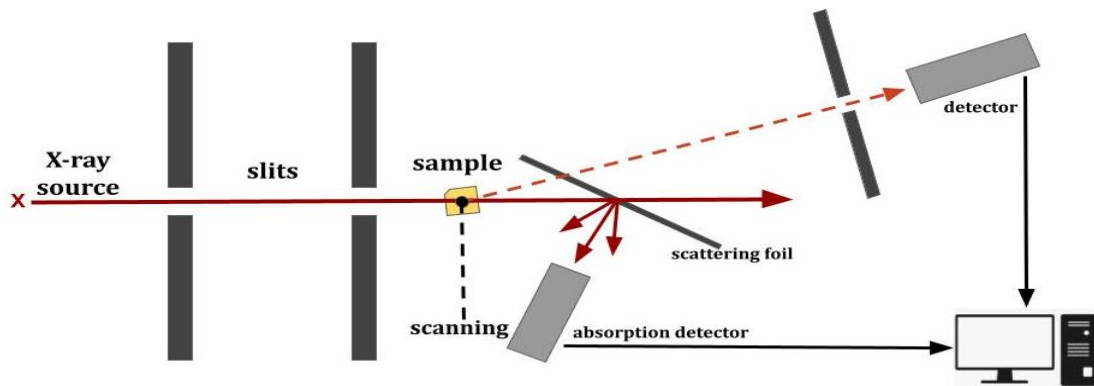


Figure 9: Schematic of X-ray diffraction.

The Bragg equation is the fundamental condition for X-ray diffracting in crystals and it shows the relationship between crystals structure and direction of diffraction line.

$$n\lambda = 2d \sin \theta$$

Where, λ represents the wavelength of x-ray, d is crystal layer spacing (path difference), θ is angle of incidence (i.e., angle between the incident ray and scatter plane), and n is an integer. When the sample is exposed to x-ray, it gets scattered by each atom in the crystals

interact and strong X-ray diffraction lines form in specific directions. When the sample exposed from various angles, diffraction took place at different crystal faces and the number of photons diffracted were counted by detector reflected from specific crystal face by creating a spectrogram of the angle-intensity relationship.

The Sherrer formula shows relationship between grain size and half-peak of the diffraction peak. Equation can be written as:

$$D = \frac{K\lambda}{\beta \cos 2\theta}$$

Where λ is the wavelength, β is the broadening of line at full width half maximum (FWHM), θ is the angle of diffraction and k is dimensionless shape factor which is having a value 0.89 that varies with shape of crystallites constant. The equation above depicts that smaller the grain size, the more diffuse and wider the diffraction line will observe.

2.3.1.10 Fourier-transform infrared spectroscopy (FTIR)

FTIR spectrum was obtained by PerkinElmer Spectrum Two FT-IR Spectrometer (**figure 10**). FTIR is a technique for investigating the physical properties of solids, liquids and gases. It enables the investigation of materials' absorptive and emissive properties. The selection of IR wavelengths in FTIR method is especially useful for studying chemical bonds that connects atoms. These bonds, it turns out, tend to vibrate at frequencies that corresponds to IR light, and can thus be easily excited by such radiations. IR spectroscopy typically covers wavenumber ranging from 200 to 4000 cm^{-1} . The Spectrum Two is a Fourier transform infrared (FTIR) spectrometer with attenuated total reflectance (ATR), transmission, specular and diffuse reflectance accessories.

- Universal ATR enables fast analysis of micron-scale thin films, opaque solids, liquids and powders from 450-4000 cm^{-1} (22 μm to 2.5 μm).
- Transmission accessory enables measurement of thin films (<100microns) on substrates that transmit mid-infrared or powders (mixed with KBr) from 400-4000 cm^{-1} (25 μm to 2.5 μm).

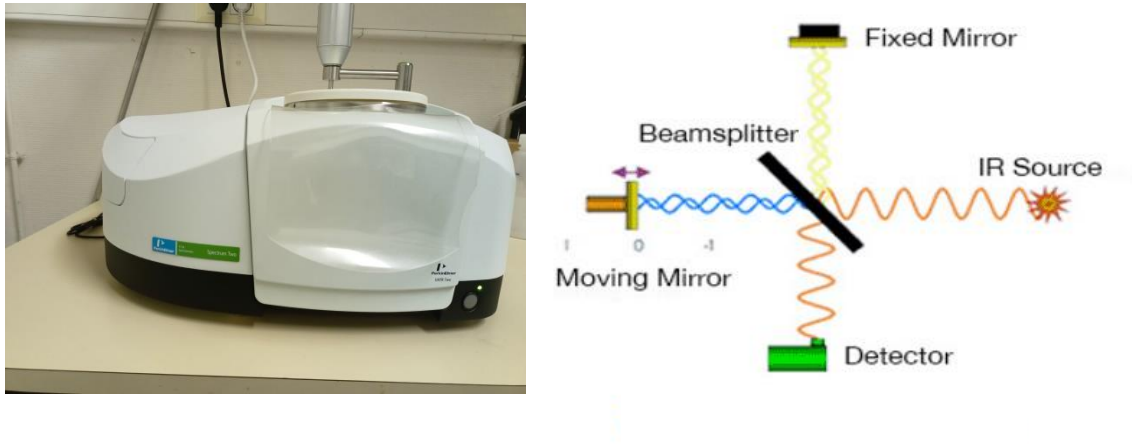


Figure 10: Schematic of FTIR.

2.4 Device Measurement

2.4.1. Memory Transistor Characterization

2.4.1.1 Current-Voltage Characteristics

Non-volatile memory transistor measurements were measured in small vacuum chamber by a computer-controlled Keithley 2612B source measurement unit (SMU). We measure three terminal devices with high gate and drain voltage and low source voltage. Devices were illuminated through the transparent glass of the chamber through which light is focused on channel. The light source of 365 nm is fixed with stand to get accurate measurements and good focus. The transfer characteristics were measured by equation as follow:⁹

$$\mu_{lin} = \frac{\partial I_{ds}}{\partial V_g} \cdot \frac{L}{WC_i V_{ds}}$$

2.4.1.2. Current-Time characteristics

Where P (W) is the power of light illumination. The memory retention measurements done by using programme but with current-time measurement up to several hours to check the retention properties of device.

2.4.2. Photoconductive switch Measurement

Both the hybrid (with nanocrystals) and the control devices (without UCNP) were characterized under top optical excitation by a 2 μm lensed fibre placed in a CASCADE Lightwave probe support and connected to a continuous wave (CW) single mode pigtailed laser operating at $\lambda = 1.55 \mu\text{m}$ (power density $\sim 12.9 \text{ mW } \mu\text{m}^{-2}$). Microwave performances of both type of devices with and without UCNP were evaluated by measuring the ON/OFF ratio ($R_{\text{ON/OFF}}$) versus the input microwave signal frequency. S-matrix coefficients of the devices were measured by using a ZVA 67 Rhode & Schwartz Vectorial Network Analyzer in the frequency range from 20 MHz to 20 GHz under the two working states, after a short-open-load through calibration with a 101–190 CASCADE calibration kit (with an Al_2O_3 substrate), in a FORM FACTOR co-planar waveguide probe test environment. Instrument accuracy on the transmission coefficient measurement of 0.005 dB was obtained with the standard co-planar line from calibration kit after an averaging technique on ten sequential measurements. The measurement is done by analysing following equations:

$$\frac{R_{\text{on}}}{\text{off}} = \frac{S_{21}(\text{On})}{S_{21}(\text{Off})} = R_{\text{on/off}} \cdot e^{j\Delta\varphi_{\text{on/off}}} \quad (1)$$

$$\text{with } S_{21}(\text{Off}) = \frac{j2\omega Z_0 C_g}{(1+j2\omega Z_0 C_g)} \quad (2)$$

$$S_{21}(\text{Onn}) = \frac{2Z_0 G_g (1+j\omega \frac{C_g}{G_g})}{(1+2Z_0 G_g) (1+\frac{j\omega 2Z_0 C_g}{(1+2Z_0 G_g)})} \quad (3)$$

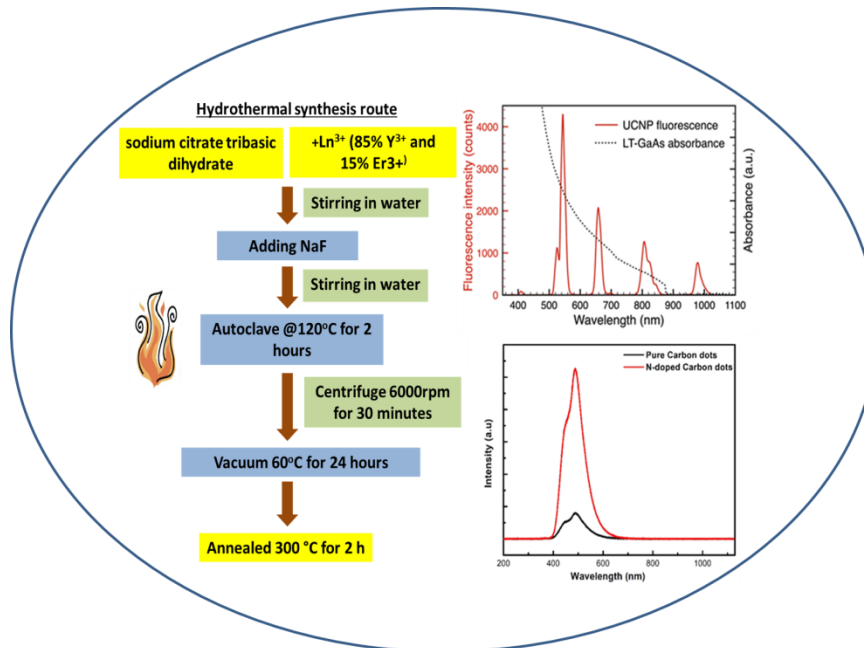
$$\text{And thus } \left| \frac{R_{\text{on}}}{\text{off}} \right| = \sqrt{\frac{(G_g^2 + C_g^2 \omega^2)(1 + 4C_g^2 Z_0^2 \omega^2)}{4C_g^4 Z_0^2 \omega^4 + C_g^2 (\omega + 2G_g Z_0 \omega)^2}} \quad (4)$$

2.5 References:-

1. Zhu, S. *et al.* Highly photoluminescent carbon dots for multicolor patterning, sensors, and bioimaging. *Angewandte Chemie - International Edition* **52**, 3953–3957 (2013).
2. Qu, S. *et al.* Toward Efficient Orange Emissive Carbon Nanodots through Conjugated sp²-Domain Controlling and Surface Charges Engineering. *Advanced Materials* **28**, 3516–3521 (2016).
3. Li, D. *et al.* Near-Infrared Excitation/Emission and Multiphoton-Induced Fluorescence of Carbon Dots. *Advanced Materials* **30**, (2018).
4. Jiang, L. *et al.* UV–Vis–NIR Full-Range Responsive Carbon Dots with Large Multiphoton Absorption Cross Sections and Deep-Red Fluorescence at Nucleoli and In Vivo. *Small* **16**, (2020).
5. Suk, J. W. *et al.* Transfer of CVD-grown monolayer graphene onto arbitrary substrates. *ACS Nano* **5**, 6916–6924 (2011).
6. Xiang, H., Hu, Z., Billot, L., Aigouy, L. & Chen, Z. Hybrid plasmonic gold-nanorod-platinum short-wave infrared photodetectors with fast response. *Nanoscale* **11**, 18124–18131 (2019).
7. Xu, X. *et al.* Electrophoretic analysis and purification of fluorescent single-walled carbon nanotube fragments. *J Am Chem Soc* **126**, 12736–12737 (2004).
8. Faulkner, D. O. *et al.* Measurement of absolute photoluminescence quantum yields using integrating spheres - Which way to go? *Laser and Photonics Reviews* **6**, 802–806 (2012).
9. Zaumseil, J. & Sirringhaus, H. Electron and ambipolar transport in organic field-effect transistors. *Chemical Reviews* vol. 107 1296–1323 (2007).

Chapter 3

Synthesis of Nanomaterials



Resume

Les méthodes de synthèse et les résultats des nanocristaux et CQDs NaYF₄:Er³⁺ à conversion ascendante obtenus sont décrits ainsi que leurs propriétés optiques. En particulier, lorsqu'ils sont excités par des photons SWIR avec un $\lambda = 1,5 \mu\text{m}$, les nanocristaux colloïdaux de NaYF₄:Er³⁺ présentent un spectre de fluorescence à pics multiples situé dans le spectre visible. Cette propriété optique d'upconversion sera exploitée pour fabriquer des commutateurs photoconducteurs actifs dans le SWIR dans le chapitre 4. Pour les CQDs, différents dopages peuvent être exercés dès la synthèse. Sous excitation UV, une fluorescence dans le spectre visible peut être obtenue. Les propriétés de piégeage des charges (associées aux conditions de dopage) seront exploitées pour la fabrication de mémoires optoélectroniques à base de FET dans le chapitre 5.

Chapter 3 Synthesis of Nanomaterials

3.1. Introduction

In this chapter, I discussed about the synthesis of carbon dots and colloidal nanocrystals for optoelectronic applications discussed in following chapters 4 and chapter 5. Firstly, the introduction of synthesis route has been discussed and the chemistry of formation of nanoparticles. Synthesis of $\text{NaYF}_4:\text{Er}^{3+}$ and CDs done to achieve multi-peak fluorescence spectrum in visible spectrum for SWIR ($\lambda = 1.5 \mu\text{m}$) range and under UV excitation fluorescence in visible spectrum can be obtained for CDs. Basic Optical and structural characterization of synthesized nanomaterials has been demonstrated in this chapter.

3.2 Experimental Section

All chemicals were purchased from sigma-Aldrich and Alfa Aesar unless indicated otherwise and used as received.

3.2.1. Method and chemistry

3.2.1.1. Hydrothermal method for synthesis of colloidal nanoparticles/crystals

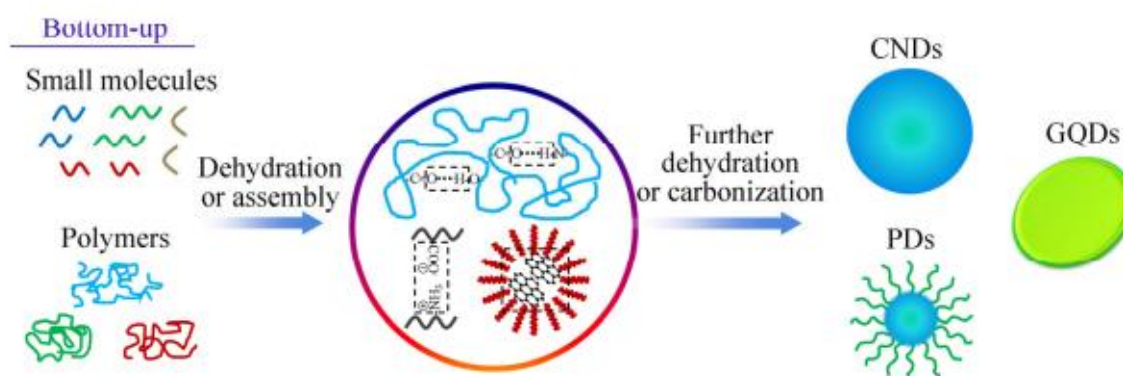


Figure 1: Bottom-up approach for the synthesis of CDs.¹

Hydrothermal synthesis (**figure 1**) is one of the most basic, cost-effective, and widely used synthetic routes for CDs. This method has the advantages of low instrumentation costs, low energy consumption, and ease of manipulation of synthesis parameters for the production of homogeneous and high-quality CDs.¹

Chapter 3 Synthesis of Nanomaterials

Et al., in 2007 Byrappa and Yoshimura proposed hydrothermal reaction as "any heterogeneous chemical reaction above room temperature and at pressure greater than one atmosphere in a closed system in the presence of a solvent (whether aqueous or nonaqueous)".² In a typical reaction, a precursor and a reagent capable of regulating crystal growth are mixed in a specific ratio with water. This mixture is placed in an autoclave to allow the reaction to continue at high temperatures and pressures. In hydrothermal synthesis, reactions take place inside the sealed and heated aqueous solution at temperature ($T > 25^{\circ}\text{C}$) and pressure ($P > 100\text{kPa}$) to crystalline particles form solution. In this approach pressure as high as 500MPa and temperature around 1000°C can be used to increase dissolution of reactants and simultaneously the nucleation and growth of different materials like single crystal oxides, CNT, semiconductor nanoparticles, Quantum dots (CDs). If synthesis occur in nonaqueous solution with organic solvents at high temperature it is called solvothermal synthesis and it depend on different types of solvent like ethylene, glycol, DMF, oleylamine etc.

The hydrothermal and solvothermal reaction carried out in sealed container (reactor or autoclave) or for subcritical and supercritical conditions of solvents high-pressure autoclave is used. The pressure generated in autoclave is proportional to the filling volume is 70% of the autoclave capacity to assure safety of the process). Teflon or alloy linings Teflon inserts are widely used to carry solution because they are inert to both acid and bases media. Teflon use at $T > 200^{\circ}\text{C}$ can creep and causes unwanted problems. In such cases alternative materials made high strength alloys are used to protect autoclave body from corrosive solvents like gold, silver.³

3.1.2.1. Surface and Colloid Chemistry of the Material in Aqueous Media and mechanism

Water is a non-hazardous material that is less expensive than other organic solvents. The density, surface tension, and viscosity of water will be lower under high temperature and pressure conditions in an autoclave, resulting in significantly higher ionic and molecular mobility of water than at ambient conditions. The ionic or chemical reactions of in dissolvable inorganic materials can be promoted under hydrothermal conditions at high

Chapter 3 Synthesis of Nanomaterials

temperature and pressure due to increased ionization of water caused by increased temperature.

During hydrothermal synthesis, nucleation and growth kinetics have a direct influence on size and morphology. The classical nucleation and growth theory states that as cation concentration increases, the number of nuclei increases due to increased saturation and nucleation frequency, and thus particle size decreases. moreover, if some of the nuclei are too small to survive, they dissolve and raise the saturation level, allowing other, larger nuclei to grow at the expense of those fine nuclei This type of growth is known as Ostwald ripening. Particle size increases as cation concentration increases in such systems. It has been demonstrated that the hydrothermal systems have a critical cation concentration (CCC) at Which nucleation and growth mechanisms are altered? While Ostwald's mechanism of ripening is effective at concentration more than the CCC. The CCC is affected by temperature, pH, pressure and other ion concentrations and other processing parameters.^{3,4}

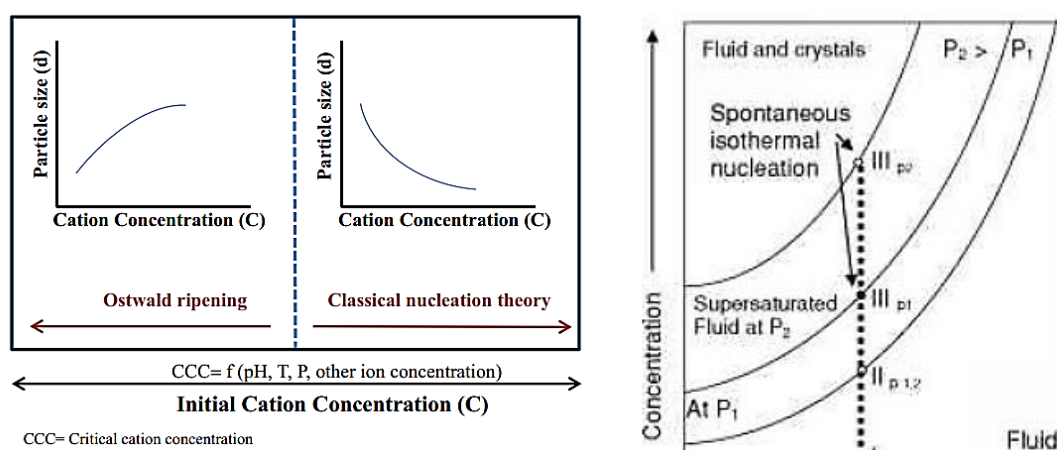


Figure 2: Effect of the initial cation concentration on the growth mechanism during the hydrothermal systems. (b) hydrothermal processing: At (I) only water and precursor materials are present. Between (I) and (III): time-dependent precursor material dissolution. Nucleation occurs spontaneously if point (III) is achieved. A subsequent crystal growth process may only take place in the field of saturated solution.^{2,3}

Also, **figure 2** depicts the various stages of the hydrothermal process, which include dissolution, supersaturation, and subsequent crystallization. Standard hydrothermal experiments are carried out without agitation under isothermal and isobar conditions. At

Chapter 3 Synthesis of Nanomaterials

the start of the experiment, the hydrothermal fluid is only made up of water and solid precursor materials.

3.2.2. Synthesis of Nanoparticles $\text{NaYF}_4:\text{Er}^{3+}$

3.2.2.1. Synthesis of $\text{NaYF}_4:\text{Er}^{3+}$:

Er^{3+} -doped NaYF_4 nanocrystals were synthesized by a previously reported hydrothermal route⁵ shown in **figure 3** with minor modifications. In a typical synthesis, a 3 mmol of sodium citrate tribasic dihydrate in 5 ml deionized (DI) water was used to react with 5 ml 1 mmol of Ln^{3+} (85% Y^{3+} and 15% Er^{3+}) aqueous solution under vigorous stirring until the formation of a white precipitate of lanthanide citrate. This is followed by a slow addition of a 5 ml aqueous solution of NaF (2.4 mol l^{-1}) and a subsequent stirring for 1 h. This precursor solution was then transferred into a 50 ml volume autoclave, which was sealed and placed into an oven preheated at $120 \text{ }^\circ\text{C}$ for a 2 h hydrothermal treatment. After this treatment finished and the autoclave being cooled down to room temperature, the synthesis products, $\text{NaYF}_4:15\%\text{Er}^{3+}$ UCNPs, were separated from their mother liquid by centrifugation (6000 rpm, 30 min) and decantation of supernatant. After being re-dispersed in DI water, the UCNPs were further purified by the above-mentioned centrifugation/decantation processes three times. The final UCNPs were first dried under vacuum at $60 \text{ }^\circ\text{C}$ for 24 h and then annealed at $300 \text{ }^\circ\text{C}$ for 2 h.

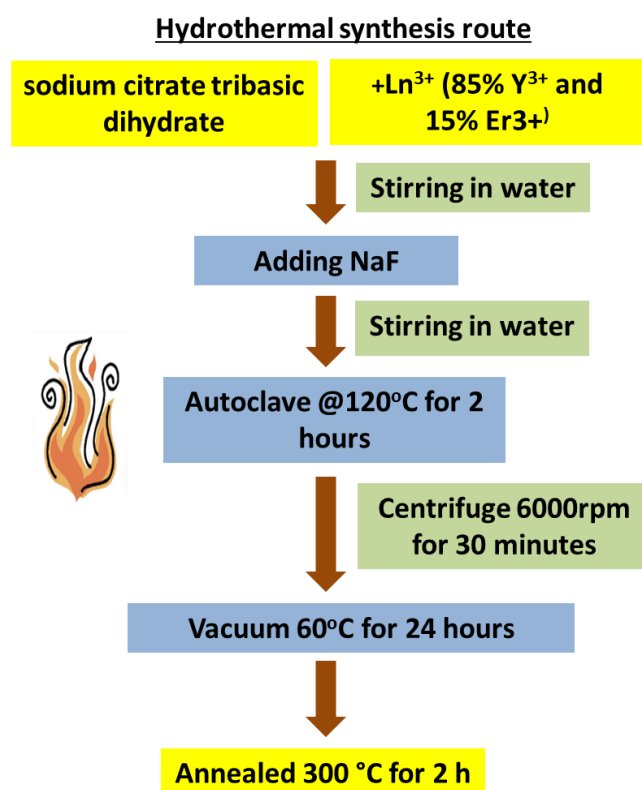


Figure 3: Hydrothermal synthesis of $\text{NaYF}_4:\text{Er}^{3+}$.

3.2.2.2. Results and Discussion

Structural and optical characterization has been discussed for synthesized $\text{NaYF}_4:\text{Er}^{3+}$ nanocrystals as follow:

3.2.2.2.1. Structural characterization

SEM characterization of UCNPs and device film as shown in **figure 4(a)** revealed these as-synthesized Er^{3+} -doped NaYF_4 nanocrystals exhibit a uniform morphology, with an average crystal dimension of $416 \text{ nm} \pm 26 \text{ nm}$. XRD in **figure 4 (b)** confirmed that these nanocrystals are highly crystalline with pure hexagonal $\beta\text{-NaYF}_4$ phase with reference pattern JCPDS no. 00-016-0334.

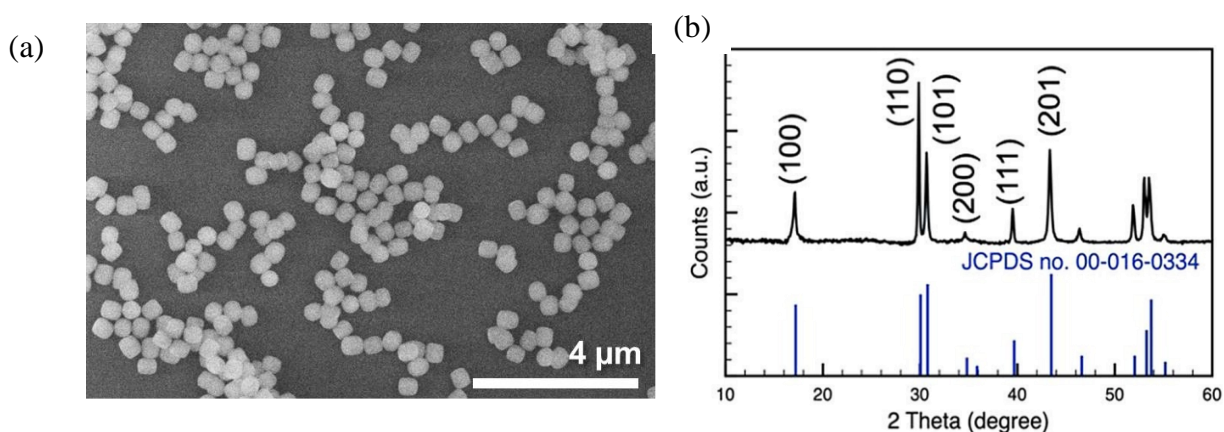


Figure 4: (a) SEM image of $\text{NaYF}_4:15\%\text{Er}^{3+}$, (b) XRD pattern of the UCNPs synthesized.

3.2.2.2.2. Optical property of UCNPs

Under the excitation of $\lambda = 1.5 \text{ m}$ laser, the obtained $\text{NaYF}_4:\text{Er}^{3+}$ exhibits strong room-temperature fluorescence. Multiple fluorescence peaks were observed in the fluorescence spectrum at this excitation, with their maximum intensity falling at the wavelengths of 980 nm (infra-red), 810 nm (infra-red), 650 nm (red), 545 nm (green), and 520 nm (green) shown in **figure 5**. A mechanism has been proposed to explain such photon upconversion in rare-earth-doped fluoride crystals.^{6,7} For example, in an oversimplified diagram, the red and two green emission lines result from a three-photon upconversion mechanism followed by de-excitations from the $^4\text{F}_{9/2}$, $^4\text{S}_{3/2}$, and $^2\text{H}_{11/2}$ states to the $^4\text{I}_{15/2}$ state (Figure 5).

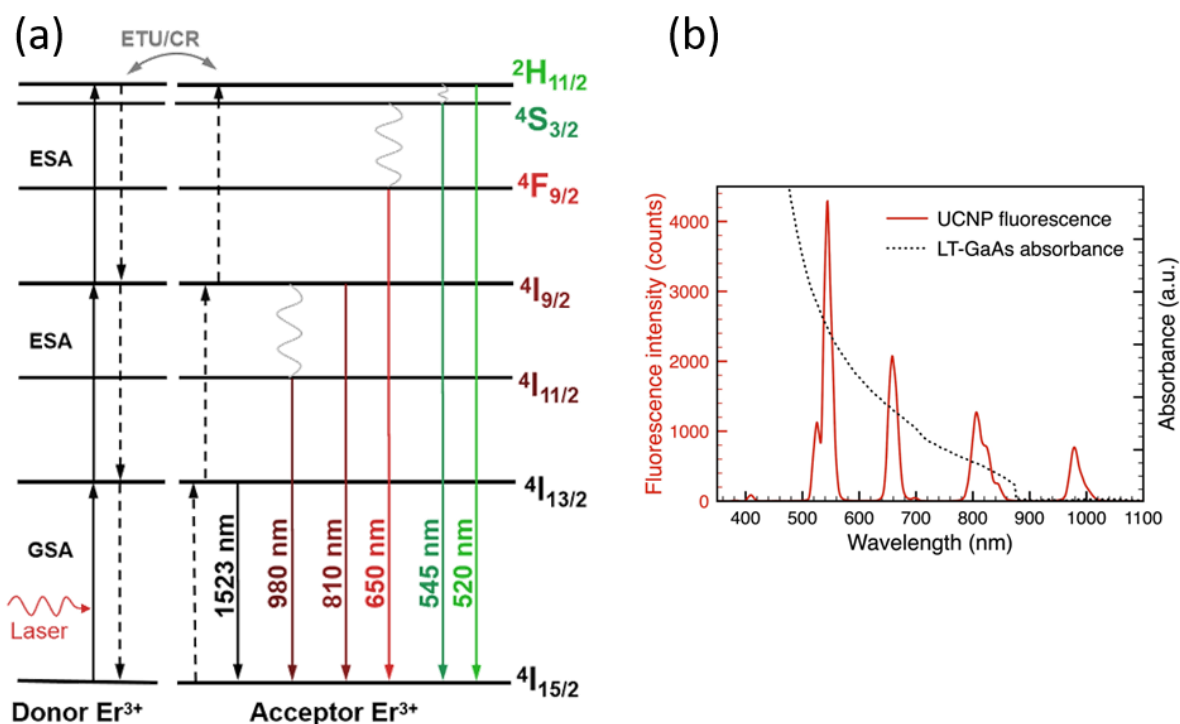


Figure 5: (a) Schematic illustrating the energy transitions corresponding to the upconversion fluorescence observed under the excitation of a $\lambda = 1.5 \mu\text{m}$ laser. ETU = energy-transfer upconversion, GSA = ground-state absorption, CR = cross-relaxation, ESA = excited-state absorption, (b) The upconversion fluorescence spectrum obtained for $\text{NaYF}_4:\text{Er}^{3+}$ and LT-GaAs under laser excitation wavelength of $1.5 \mu\text{m}$.

3.2.3. Synthesis of Carbon Dots

Hydrothermal synthesis of all synthesized carbon dots has been done described in **figure 6**.

Synthesis of Pure Carbon Dots (CDs):

CDs was synthesis according to literature using citric acid (1.0507g) was dissolved in 10ml of DI-water. The solution was poured to a poly (tetrafluoroethylene) (Teflon)-lined autoclave (30 mL) and heated at 200°C for 5 hours. The reactors were cooled to room temperature by water or naturally after the reaction. The product, which was brown-black and transparent, was dialyzed in order to obtain the CDs. The production yield was approximately 1%.

Synthesis of Carbon dots (CDs):

Carbon dots were made by,⁸ dissolving citric acid (1.0507 g) and ethylenediamine (335 μL) in DI-water (10 mL). The solution was then transferred to a poly (tetrafluoroethylene) (Teflon)-lined autoclave (30 mL) and heat for 5 hours at $150/200^\circ\text{C}$. After the reaction (**figure 7**), the

Chapter 3 Synthesis of Nanomaterials

reactors were cooled to room temperature by water or naturally. The brown-black or transparent product was dialyzed in to obtain the CDs. The production yield was approximately 39.4%.

Procedure for synthesis

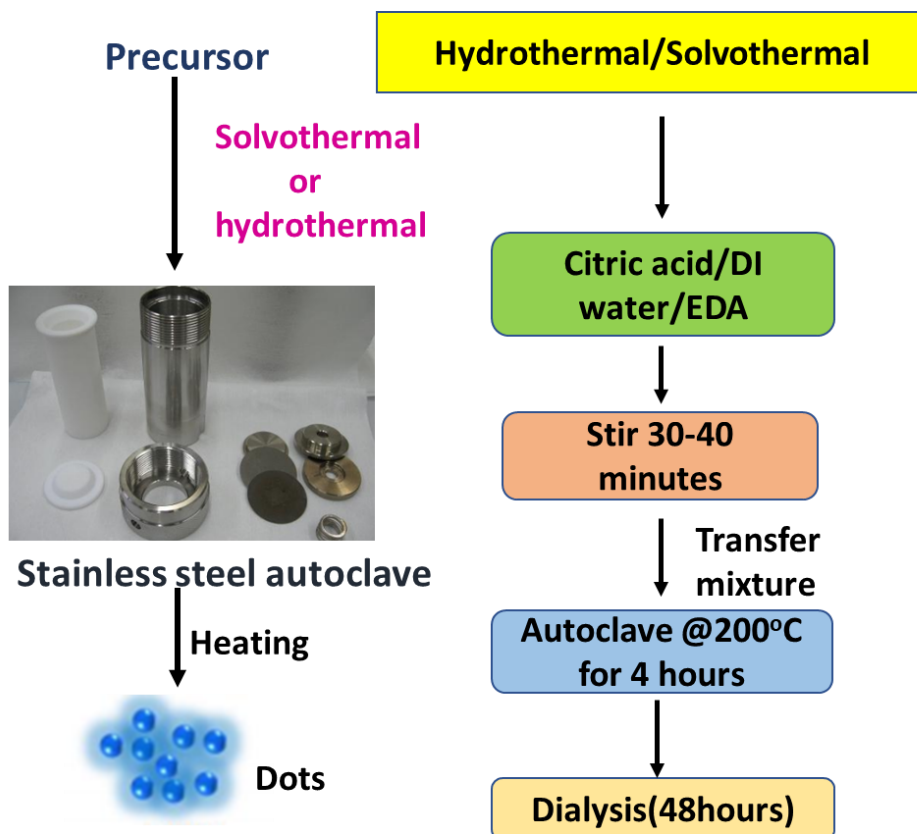


Figure 6: Hydrothermal synthesis of Carbon dots.

Chapter 3 Synthesis of Nanomaterials

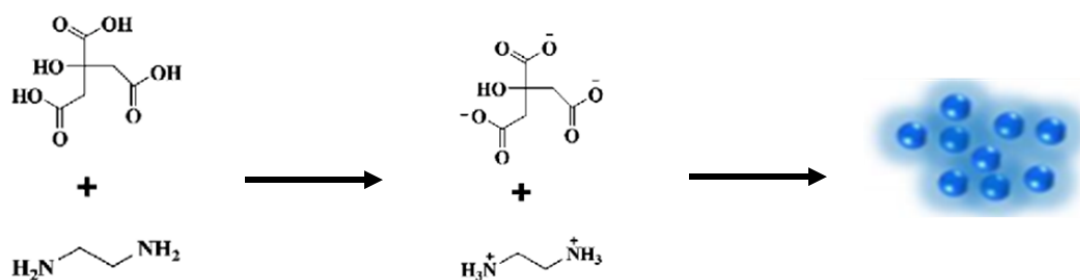


Figure 7: Schematic of synthesis of CDs.

In order to get long-wavelength emissive Carbon dots a bandgap transition of CDs is come from conjugate sp² domains. In literature it is suggest that bandgap of CDs can be tuned by modulating the size of conjugated sp² domain. Therefore, the doping and different solvent were used to modify the band-gap and absorption of CDs.

Synthesis of N-doped CDs in DMF:

The CDs were prepared using a previously described solvothermal procedure.⁹ Under solvothermal conditions, a mixture of citric acid (2.0 g), urea was prepared (4.0 g) and DMF (20 mL) in an autoclave for 6 hours at 160 °C (**figure 8**). Following cooling to room temperature NaOH aqueous solution (50 mg mL⁻¹, 40 mL) is added, and the resulting mixture is centrifuged (16000 r min⁻¹, 10 min). Following the removal of the supernatant solution, the precipitate is dissolved in dilute HCl aqueous solution (5 %, 50 mL) and stirred for 10 minutes before being centrifuged again (16000 r min⁻¹, 10 min). The precipitate is collected, dissolved in water, and centrifuged at a rate of 16000 r min⁻¹, 10 min) two times.

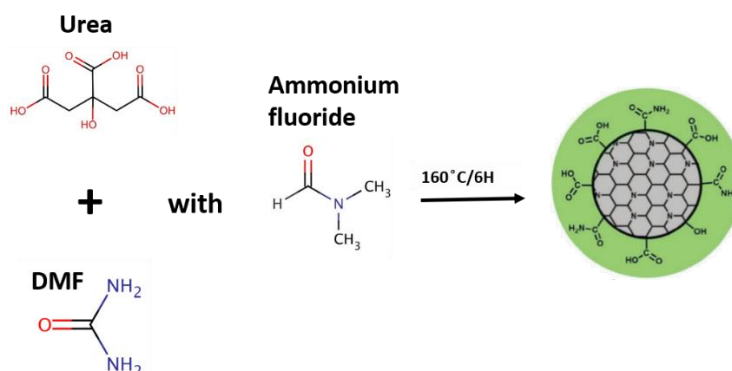


Figure 8: Schematic of N-doped CDs in DMF solvent.

Chapter 3 Synthesis of Nanomaterials

Urea and citric acid mixture form a nanoplate structure through intermolecular H-bonding. In solvothermal reactions, dehydrolysis process happened between citric acid and urea to form nitrogen rich CDs with the abundance of surface groups like carboxyl, hydroxyl, and amide groups.

In order to get metal-cation-functionalized CDs NaOH solution is added then carboxyl and phenolic hydroxyl groups were neutralized. Further to get non-metal-cation-functionalized CDs diluted HCL is used and it will remove the passivation layer.

Synthesis of N-S doped CDs:

The CDs were prepared using a previously described solvothermal procedure. Under solvothermal conditions, a mixture of citric acid (2.0 g), urea was prepared (4.0 g) and instead of DMF, DMSO (20 mL) is used for sulphur source in an autoclave for 6 hours at 160 °C. Following cooling to room temperature NaOH aqueous solution (50 mg mL⁻¹, 40 mL) is added, and the resulting mixture is centrifuged (16000 r min⁻¹, 10 min). Following the removal of the supernatant solution, the precipitate is dissolved in dilute HCl aqueous solution (5 %, 50 mL) and stirred for 10 minutes before being centrifuged again (16000 r min⁻¹, 10 min). The precipitate is collected, dissolved in water, and centrifuged at a rate of 16000 r min⁻¹, 10 min) two times.¹⁰

Also, CDs can be functionalized in DMSO by making the solution of N-doped CDs in DMSO solvent.

Synthesis of N-F doped CDs:

In a typical synthesis of colloidal nanocrystals, citric acid (2 g) and urea (4 g) were thoroughly dissolved in 20 mL of DMF.¹¹ Second, 0.195 g of NH₄F was added to the above solution and sonicated for 10 minutes. The solution was transferred to a Teflon-lined container stainless-steel autoclave, reacted at 180 °C for 4 hours, then cooled to room temperature naturally. Citric acid and urea combined to form N-doped carbon dots during the solvothermal synthesis as previously reported, and the decomposition of NH₄F occurred concurrently as follows: NH₄F = NH₃ + HF because NH₄F normally decomposes above 130 °C. Because the generated HF is a strong acid, it will more easily react with N-doped carbon dots to form Carbon dots with F, N co-doped (N-CDs-F). Third, the obtained red suspension was poured into a NaOH aqueous solution (pH = 13, 1.2 M), stirred for 10 minutes, and centrifuged at

Chapter 3 Synthesis of Nanomaterials

12,000 r min⁻¹ for 10 minutes, the black precipitate was obtained. The precipitate was washed with dilute HCl aqueous solution (pH = 2, 1.6 M) and ultrapure water several times. Finally, the dark colour precipitate was collected by Centrifugation (12,000 r min⁻¹, 10 minutes).

By using same procedure for synthesis of N-F doped CDs as shown in schematic 1

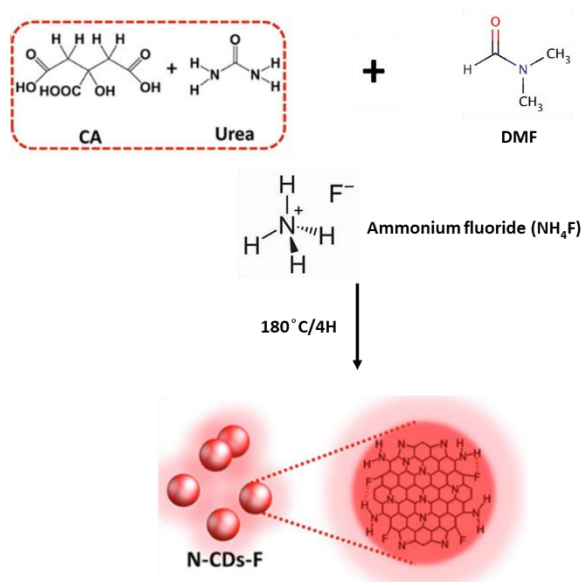


Figure 9: Schematic of N-F CDs synthesis.

Via hydrothermal one-pot solvothermal method with optimum condition of 180 °C for 4H in DMF the red emissive D- π -A conjugated N-F doped CDs. Where citric acid is carbon core and urea and ammonium fluoride (NH₄F) for N-F doping source. DMF molecule enable pseudo-hydrogen bonding with the C – F Bond and C = O modify the surface of CDs. There is formation of strong inter-dot hydrogen bond (N – H \cdots F) and plenty of inter and intra hydrogen bond. Carbon core is formed in graphitic carbon surrounded by all the molecules and bonds and called π -conjugated molecule. After incorporation N and F atoms into sp² hybridization. As a result, the optical band gap is affected, and electronic transitions are increased under NIR excitations.

The UV-Vis , photoluminescence and Quantum yield of N-doped in DMF, N,S-doped in DMF and N-F doped is represented in annex part of this thesis.

Chapter 3 Synthesis of Nanomaterials

3.2.3.1. Results and Discussion

The optical and structural characterization has been done to showcase internal properties of nanomaterials. **Figure 10 (a,b)** shows N-doped CDs and pure CDs shows absorption peak at 350 nm depicts that because of doping or surface states high absorption observed in N-doped CDs compared to pure CDs and carbonic core is obtained in both CDs. This clearly defines that doping plays a vital role to get high luminescence and optical absorption.

Figure 11, shows the tauc plot obtained from UV-Vis spectra of N-doped CDs to estimate the band-gap for HUMO and LUMO. From tauc plot we find out the bandgap of N-doped CDs was 3.1 eV.

Photoluminescence quantum yield for pure and N-doped CDs has been calculated and shown in **table 1**.

Figure 12 the Time resolved photoluminescence of N-CDs presented. The photoluminescence decay curve was measured with power: N-doped 6MHz, of integration time: 480sec under optical window: 40nm (from 500) giving average life time: 14.2ns Decay curve. **Table 2** represents values of 2 exponential decay.

Figure 13 FTIR spectrum of pure and N-doped CDs by comparing two spectrum generation of different peaks can be obtained because of Nitrogen doping.

Figure 14 the Raman spectra was obtained for CVD grown graphene layer that is transferred to the Si/SiO₂ to make graphene FET. The process of graphene transfer was explained in chapter 2 in figure 1.

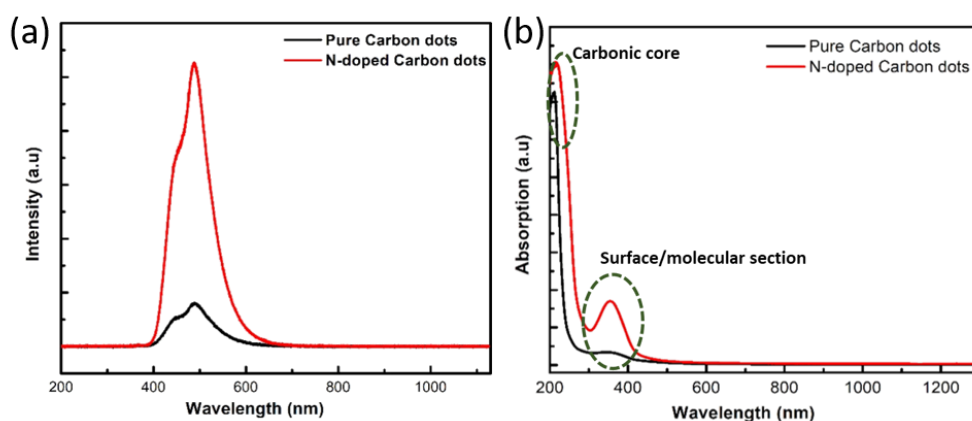


Figure 10:(a) Photoluminescence spectrum and (b) UV-Vis absorption spectra of pure and N-doped CDs.

Chapter 3 Synthesis of Nanomaterials

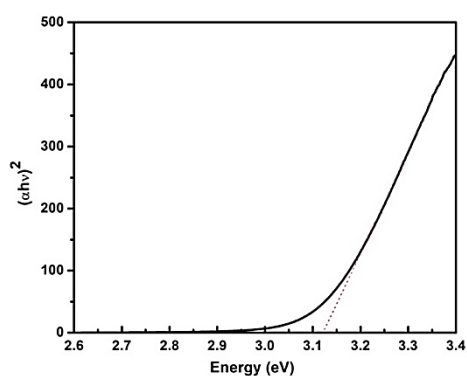


Figure 11: Tauc plot based on the UV-Visible optical absorbance data of the Fig. 1(b) of the main text. The red dotted line represents the linear extrapolation with its x-axis interception providing an estimation on the optical bandgap.

PLQE was determined by slope method by reference of rhodamine 6B: compared the integrated photoluminescence intensity (365 nm excitation) and absorbance value [several values (less than 0.1 at excitation wavelength) gave the curve] of the CDs samples with that of the references. Then by using formula shown in chapter 2 section 2.4.1.5 Photoluminescence (PL).

Table 1: Photoluminescence quantum yield of pure and N-doped CDs.

Serial	Rhodamine 6B	Pure CDs	N-doped CDs
K	4567	89	1995
Φ (%)	95%	1%	39.4%

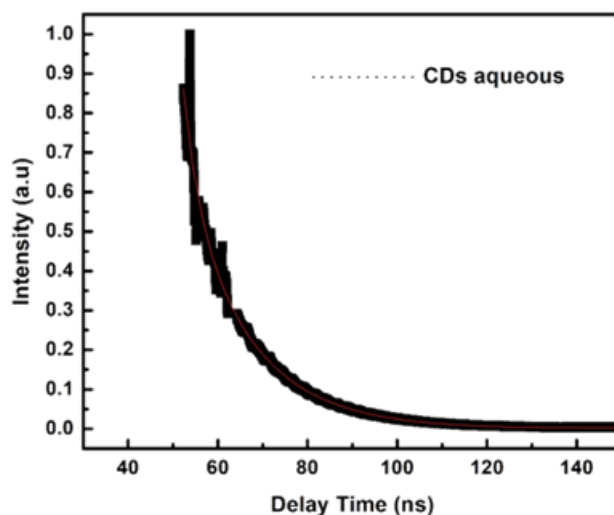


Figure 12: Time resolved photoluminescence of N-CDs.

Chapter 3 Synthesis of Nanomaterials

Table 2: Shows bi-exponential decay.

S.no	τ_1 (ns)	A1	τ_2 (ns)	A2	τ_2 (ns)
CDs	14.669	9.306136E5	3.418	4.16	14.2 ns

The fluorescence mechanism of CDs depends on intrinsic states and dark states. Wang group found that intrinsic states because of graphene core which attribute to low PL and short life time. The two radiative lifetimes τ_1 and τ_2 may be assigned to intrinsic recombination of initially populated core states and surface states. CDs exhibit tri- and biexponential decay with average lifetime of 14.2 ns. It is well-known that diverse fluorophores or energy levels present in the samples are responsible for their multiple lifetimes. We can compare this in the following paper.¹²

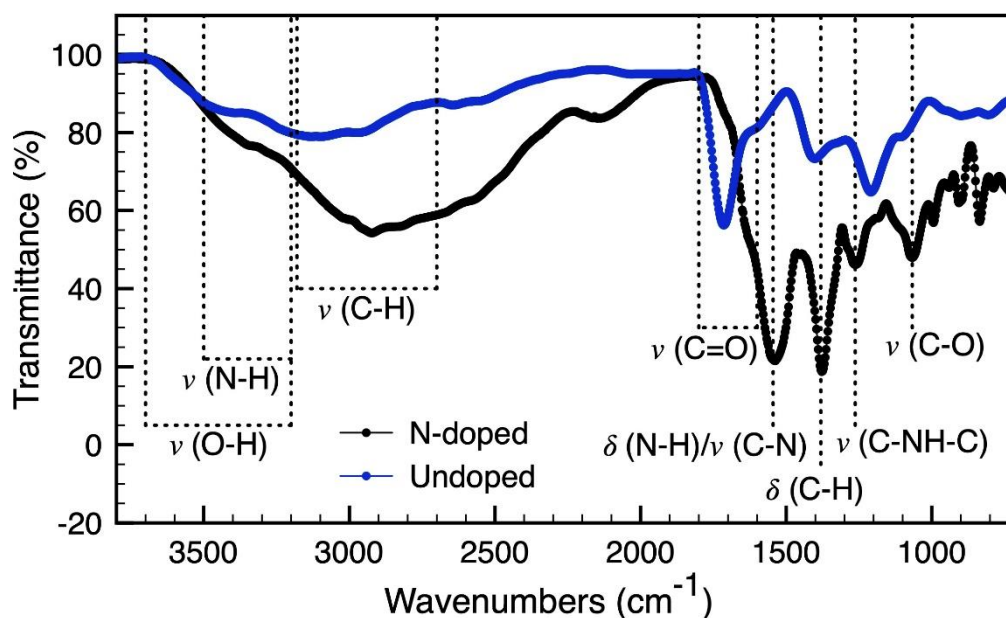


Figure 13: FTIR spectrum of CDs and N-CDs.

Chapter 3 Synthesis of Nanomaterials

The absorption peaks at 3340 cm^{-1} and 2914 cm^{-1} in the FTIR spectrum are attributed to the stretching vibrations of O-H and C-H, respectively, indicating incomplete formation carbonized molecule due to nitrogen doping. Also comparing the FT-IR spectra of N-doped CDs to that of pure CDs, it can be seen that there are two distinct peaks at 1379 cm^{-1} (NH) and 1545 cm^{-1} (C=O), which should be the result of the symmetric and asymmetric stretching vibrations of C=O. This was also explained by *et al.*, in 2017 Li Gao that incomplete formation of carbonic molecules led to formation N-doped CDs.^{13,14} For N-doped CDs the peaks obtained was analysed by using *et al.*, in 2013 Zhu S.¹⁴

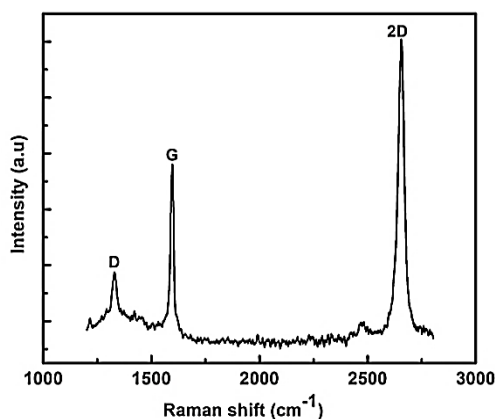


Figure 14: Raman spectrum of CVD graphene monolayer after lift off on Si substrate.

The Raman spectrometer is a Renishaw InVia in backscattered configuration with a 633nm laser of power 10mW. Single layer graphene with the ratio being around 2, Intensity ratio of $I(G)$ AND $I(2D)$ peak increases with number of layers broadening of 2D band sensitive to number of layer present. Analysis of peak compared from *et al.*, in 2018 Casimir D.¹⁵

$$I(2D)/I(G)=1.49$$

3.2.3.2. Device measurement I-V characteristics

Transfer characteristics has been measured to check change of I-V under the illumination of UV. **Figure 15 (a)** depicts no change in graphene FET under dark and light, and in **figure 15 (b)** the I-V curve change from P-type to N-type after depositing N-CDs on the graphene FETs.

Chapter 3 Synthesis of Nanomaterials

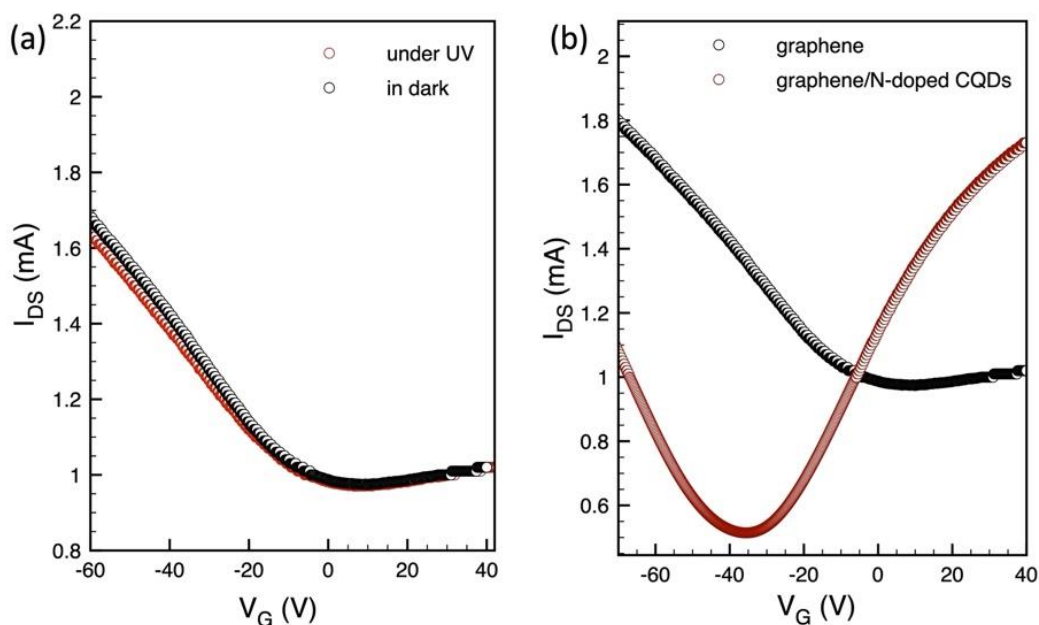


Figure 15: Transfer characteristics measured at $V_{DS} = 0.5$ V on the same graphene FET shown in the main text (a) in dark and under UV illumination (irradiance $E_a = 0.7$ mW cm⁻²). (b) The comparison of the transfer characteristics of this device (measured at $V_{DS} = 0.5$ V) before and after depositing the N-doped CQDs.

3.2.4. Summary

In summary, synthesis of colloidal nanomaterials has been done through hydrothermal route. The procedure of synthesis has been explained in details for each material. Structural and optical characterization has been shown that NaYF₄:Er³⁺ give excellent response under $\lambda = 1.5$ μ m and CDs under UV light that make these colloidal nanomaterials suitable to be used in microwave photo-conductive switch explained in chapter 4 and for the formation optical memory formation by exploiting the charge trapping ability of N-doped CDs explained in chapter 5. Some basic optoelectronic measurement of graphene FET has been done to show (a) graphene FET is non-responsive under dark and light illumination, (b) by depositing N-doped CDs the I-V curve changes from P-type to N-type.

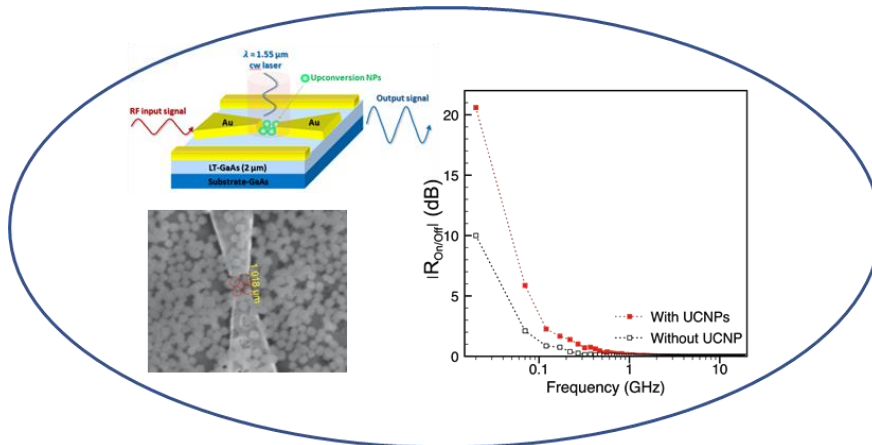
Chapter 3 Synthesis of Nanomaterials

3.3 References:

1. Zhu, S. *et al.* The photoluminescence mechanism in carbon dots (graphene quantum dots, carbon nanodots, and polymer dots): current state and future perspective. *Nano Research* vol. 8 355–381 Preprint at <https://doi.org/10.1007/s12274-014-0644-3> (2015).
2. Byrappa, K. & Adschiri, T. Hydrothermal technology for nanotechnology. *Progress in Crystal Growth and Characterization of Materials* vol. 53 117–166 Preprint at <https://doi.org/10.1016/j.pcrysgrow.2007.04.001> (2007).
3. Suvaci, E. & Özel, E. Hydrothermal synthesis. in *Encyclopedia of Materials: Technical Ceramics and Glasses* vols 1–3 59–68 (Elsevier, 2021).
4. Thejas, R. *et al.* Effect of cation concentration on structural, morphology, optical properties of Zinc-Nickel ferrite nanoparticles. *Materials Letters: X* **15**, 100156 (2022).
5. Xiang, H., Hu, Z., Billot, L., Aigouy, L. & Chen, Z. Hybrid plasmonic gold-nanorod-platinum short-wave infrared photodetectors with fast response. *Nanoscale* **11**, 18124–18131 (2019).
6. Ivanova, S. & Pellé, F. *Strong 1.53 μ m to NIR-VIS-UV upconversion in Er-doped fluoride glass for high-efficiency solar cells.* (2009).
7. Ivaturi, A. *et al.* Optimizing infrared to near infrared upconversion quantum yield of β -NaYF₄:Er³⁺ in fluoropolymer matrix for photovoltaic devices. *J Appl Phys* **114**, (2013).
8. Zhu, S. *et al.* Highly photoluminescent carbon dots for multicolor patterning, sensors, and bioimaging. *Angewandte Chemie - International Edition* **52**, 3953–3957 (2013).
9. Li, D. *et al.* Near-Infrared Excitation/Emission and Multiphoton-Induced Fluorescence of Carbon Dots. *Advanced Materials* **30**, (2018).
10. Wang, K. *et al.* Effects of elemental doping on the photoluminescence properties of graphene quantum dots. *RSC Adv* **6**, 91225–91232 (2016).
11. Jiang, L. *et al.* UV–Vis–NIR Full-Range Responsive Carbon Dots with Large Multiphoton Absorption Cross Sections and Deep-Red Fluorescence at Nucleoli and In Vivo. *Small* **16**, (2020).
12. Du, Q., Zheng, J., Wang, J., Yang, Y. & Liu, X. The synthesis of green fluorescent carbon dots for warm white LEDs. *RSC Adv* **8**, 19585–19595 (2018).
13. Gao, L. *et al.* Simple method for: O -GlcNAc sensitive detection based on graphene quantum dots. *RSC Adv* **7**, 31204–31211 (2017).
14. Zhu, S. *et al.* Highly photoluminescent carbon dots for multicolor patterning, sensors, and bioimaging. *Angewandte Chemie - International Edition* **52**, 3953–3957 (2013).
15. Casimir, D., Ahmed, I., Garcia-Sanchez, R., Misra, P. & Diaz, F. Raman Spectroscopy of Graphitic Nanomaterials. in *Raman Spectroscopy* (InTech, 2018). doi:10.5772/intechopen.72769.

Chapter 4

Colloidal upconversion nanocrystals enable low-temperature-grown GaAs photoconductive switch operating at $\lambda = 1.55 \mu\text{m}$



Resume

Les commutateurs photoconducteurs hyperfréquences, permettant un contrôle optique sur l'amplitude et la phase des signaux hyperfréquences à transmettre, sont des composants importants pour de nombreuses applications optoélectroniques. Ces dernières années, il y a des demandes importantes pour développer des commutateurs photoconducteurs fonctionnels dans la fenêtre du spectre des ondes courtes et de l'infrarouge (par exemple $\lambda=1.3-1.55 \mu\text{m}$) mais la plupart des semi-conducteurs de l'état de l'art pour les commutateurs photoconducteurs ne peuvent pas atteindre cet objectif. Dans ce travail, nous proposons une nouvelle approche, par l'utilisation de nanocristaux colloïdaux à upconversion traités en solution et déposés directement sur de l'arséniure de gallium cuit à basse température (LT-GaAs), pour réaliser des commutateurs photoconducteurs micro-ondes fonctionnels à une illumination $\lambda=1,55 \mu\text{m}$. Un commutateur photoconducteur hybride à conversion ascendante de nanocristaux de NaYF₄ dopés à l'Er³⁺ et de LT-GaAs a été fabriqué. Sous un éclairage laser à onde continue $\lambda=1,55 \mu\text{m}$ (densité de puissance $\sim 12,9 \text{ mW } \mu\text{m}^{-2}$), grâce au transfert d'énergie par upconversion à partir des nanocristaux, une valeur plus de 2 fois plus grande en décibels a été mesurée pour le rapport ON/OFF sur le dispositif hybride nanocristaux/LT-GaAs par rapport au dispositif de contrôle sans

upconversion. par rapport au dispositif de contrôle sans nanoparticules à upconversion. Un rapport ON/OFF maximal atteignant 20,6 dB a été mesuré sur le dispositif hybride nanocrystal/LT-GaAs à une fréquence de signal d'entrée de 20 MHz.

4.1 Introduction

Microwave photoconductive switches belong to a type of electrical switch that allows an optical control on the magnitude and phase of the microwave signals to be transmitted. . The operation of such devices relies on the change of electrical conductance induced by illumination, for example, due to the generation of electrons and holes in semiconductors upon above-bandgap photoexcitation contributing to the increased conductivity. Photoconductive switches are highly demanded for a wide range of applications, such as electrical signal switching¹⁻⁷, signal sampling⁸⁻¹⁰, voltage pulse^{11,12}, waveform generation¹³⁻¹⁵, and terahertz emitters¹⁶. So far, popular choices of semiconductors to achieve microwave photoconductive switches are chromium-doped gallium arsenide⁶, low-temperature-grown gallium arsenide (LT-GaAs)¹⁷⁻²⁰, indium phosphide (InP)^{1,3}, silicon (Si) and its derivatives^{4,5,8,10,11,13} (e.g. amorphous Si and Si on sapphire). Among them, LT-GaAs was developed with a growth temperature less than 200 °C in order to have abundant arsenic antisite-related deep states which lead to subpicosecond carrier lifetime in the samples. Besides the short carrier lifetime which is necessary to reduce the recovery time of the switch, LT-GaAs also exhibits high carrier mobility and high dark resistivity, all of which are factors contributing to the intensive research so far performed on photoconductive switches based on this material¹⁷⁻²⁰. Nevertheless, the operation of LT-GaAs-based photoconductive switches is limited to an optical excitation source with a wavelength (λ) shorter than 800 nm due to the direct bandgap of GaAs ($\sim 1.42 \text{ eV}$ ²¹ at room temperature), while common optical communications are typically operated at wavelengths of 1.3 or 1.55 μm . In fact, photoconductive switches based on most of the above-mentioned material systems cannot achieve functionality at these short-wave infrared wavelengths.

Some research efforts have therefore been dedicated to the development of

photoconductive switches functional in the short-wave-infrared spectrum window (e.g. $\lambda = 1.3\text{--}1.55 \mu\text{m}$). For example, attempts have been made to exalt the trap-assisted two-photon absorption (TPA) in LT-GaAs to provide photoconductive switch under $\lambda = 1.55 \mu\text{m}$ illumination but the performance of the device was limited by the low TPA coefficient in LT-GaAs.²⁰ Another approach consists to reduce the band gap of GaNAsSb to 0.8 eV by increasing the concentration of nitrogen and antimony doping²². Photoconductive switch of GaNAsSb functional at $\lambda = 1.55 \mu\text{m}$ was then realized exhibiting an ON–OFF ratio of 9 dB at microwave signal with a frequency of 1.5 GHz. Towards similar objectives, photoconductive switches based on two-dimensional materials such as exfoliated black phosphorus were also fabricated, providing a maximum ON/OFF ratio of 17.2 dB for microwave signal at 1 GHz.²³

To harvest near-infrared and short-wave-infrared photons, in the past years, many colloidal upconversion nano- particles (UCNPs) have been synthesized^{24–28}, typically containing trivalent lanthanide dopants in an inorganic crystalline host with low lattice phonon energies and low nonradiative loss and involving a multi-photon absorption process²⁹. Here, upconversion refers to the capability of materials to absorb and convert low-energy photons to high-energy photons. Most of these previous UCNPs applied a co-doping of Yb^{3+} and Er^{3+} in order to upconvert near-infrared light with a wavelength shorter than $1.0 \mu\text{m}$ (e.g. upconversion from 808 or 975 nm to visible photons). Recently, attempts to upconvert $\lambda = 1.5 \mu\text{m}$ illumination to visible photons by colloidal nanomaterials have emerged leading to potential optoelectronic applications: for example, photodetectors based on Er^{3+} -doped silicate nano sheets/ hybrid perovskite halide³⁰, Er^{3+} -doped NaYF_4 nanocrystal/conjugated polymer^{24,31}, and Er^{3+} -doped NaYF_4 nanocrystal/ Si^{32} were fabricated recently exhibiting promising photoresponse characteristics under $\lambda = 1.5 \mu\text{m}$ illumination. Yet, no attempts have been done so far, to our best knowledge, to apply upconversion nanocrystals on micro- wave photoconductive switches to achieve functionality under $\lambda = 1.5 \mu\text{m}$ illumination. In this work, we investigated an alternative approach by applying solution-processed colloidal upconversion nanocrystals directly on LT-GaAs to achieve hybrid photoconductive switches functional at $\lambda = 1.55 \mu\text{m}$ illumination.

4.2 Experimental

Er^{3+} -doped NaYF_4 nanocrystals were synthesized by a previously reported hydrothermal route^{24,32} with minor modifications. In a typical synthesis, a 3 mmol of sodium citrate tribasic dihydrate in 5 ml deionized (DI) water was used to react with 5 ml 1 mmol of Ln^{3+} (85% Y^{3+} and 15% Er^{3+}) aqueous solution under vigorous stirring until the formation of a white precipitate of lanthanide citrate. This is followed by a slow addition of a 5 ml aqueous solution of NaF (2.4 mol l^{-1}) and a subsequent stirring for 1 h. This precursor solution was then transferred into a 75 ml volume autoclave, which was sealed and placed into an oven preheated at $120 \text{ }^\circ\text{C}$ for a 2 h hydrothermal treatment. After this treatment finished and the autoclave being cooled down to room temperature, the synthesis products, $\text{NaYF}_4:15\%\text{Er}^{3+}$ UCNPs, were separated from their mother liquid by centrifugation (6000 rpm, 30 min) and decantation. After being re-dispersed in DI water, the UCNPs were further purified by the above-mentioned centrifugation/decantation processes three times. The final UCNPs were first dried under vacuum at $60 \text{ }^\circ\text{C}$ for 24 h and then annealed at $300 \text{ }^\circ\text{C}$ for 2 h.

SEM characterizations were performed by a FEI Magellan 400 system with a standard field emission gun source equipped with a EDX detector. XRD spectra were obtained by a PANalytical X'Pert x-ray diffractometer using $\text{Cu K}\alpha$ radiation. UV– visible absorbance spectra were carried out by a Jasco V-770 UV/VIS/NIR Spectrophotometer. Fluorescence experiments were performed by a reflection mode on Er^{3+} -doped NaYF_4 nanocrystals deposited on a glass substrate with an excitation source at the wavelength of $\lambda = 1.5 \mu\text{m}$ achieved by a single mode pigtailed laser diode (45 mW). Fluorescence was recorded by an Ocean Optics HR4000 spectrometer with an optical fiber. Fluorescence quantum yield measurements were performed on nanocrystal powders deposited on a home-made holder with a integrating sphere by a method established previously³³ and recorded simultaneously by two spectrometers (Ocean Optics HR4000 spectrometer and Ocean Optics NIR-Quest 256 spectrometer). Kubelka-Munk function was calculated from the diffuse reflectance spectra obtained on nanocrystal powders deposited on a glass

substrate measured by an Ocean Optic reflectance probe together with a Spectralon diffuse reflectance standard, a fiber-coupled tungsten halogen light source, and an Ocean Optics HR4000 spectrometer (for visible spectrum measurements) or an Ocean Optics NIR-Quest 256 spectrometer (for infrared spectrum measurements).

LT-GaAs layer on a bulk GaAs substrate was grown using a standard MBE method and post annealing on which 150 nm thick gold electrodes (with 10 nm thick Ti adhesive layer) were then defined by E-beam lithography to complete the photo-conductive switch fabrication. Er^{3+} -doped NaYF_4 nanocrystals were first dispersed in isopropanol with the help of sonication and such solution was then drop-cast onto the surface of the above-mentioned LT-GaAs photoconductive switches. SEM characterizations were performed before and after nanocrystal deposition. Both the hybrid (with nanocrystals) and the control devices (without UCNPs) were characterized under top optical excitation by a 2 μm lensed fiber placed in a CASCADE Lightwave probe support and connected to a continuous wave (CW) single mode pigtailed laser operating at $\lambda = 1.55 \mu\text{m}$ (power density $\sim 12.9 \text{ mW } \mu\text{m}^{-2}$). Microwave performances of both types of devices with and without UCNPs were evaluated by measuring the ON/OFF ratio (RON/OFF) versus the input microwave signal frequency. S-matrix coefficients of the devices were measured by using a ZVA 67 Rhode & Schwartz Vectorial Network Analyzer in the frequency range from 20 MHz to 20 GHz under the two working states, after a short-open-load-through calibration with a 101–190 CASCADE calibration kit (with an Al_2O_3 substrate), in a FORM FACTOR co-planar waveguide probe test environment. Instrument accuracy on the transmission coefficient measurement of 0.005 dB was obtained with the standard co-planar line from calibration kit after an averaging technique on ten sequential measurements.

4.3 Results and discussion

The device structure of the LT-GaAs photoconductive switch under study and its topography view are exhibited in **figure 1**. On such a device, a 2 μm thick LT-GaAs layer was grown on a bulk GaAs substrate. On the top surface of LT-GaAs, gold electrodes were defined to form transmission (or signal) lines with a tip width of 1 μm and separated by a

gap of $1.02 \mu\text{m}$ (**figure 1(b)**). Two ground planes were also defined next to the signal lines. The equivalent circuit model of the active region (the region between the gap) of such photoconductive switches has been established previously^{34,35} and shown in **figure 1(c)** similarly to a microwave high pass filter. Based on such a model, the active region is dominated by the gap conductance (G_g) and gap capacitance (C_g) connected in parallel, where the value of G_g depends on the illumination intensity and wavelength. They are further connected in series with the two circuits, where the shunt conductance (G_s) and the shunt capacitance (C_s), both associated with the region outside the gap, is connected in parallel. For high resistivity materials like LT-GaAs, G_s is typically extremely small and can be neglected. The microwave photoconductive ON/OFF ratio (with and without illumination) can be determined by the S21 transmission coefficient measured by a network analyzer:

$$\mathfrak{R}_{On/Off} = S_{21}(On)/S_{21}(Off) = R_{On/Off} \cdot e^{j\Delta\varphi_{On/Off}} \quad (1)$$

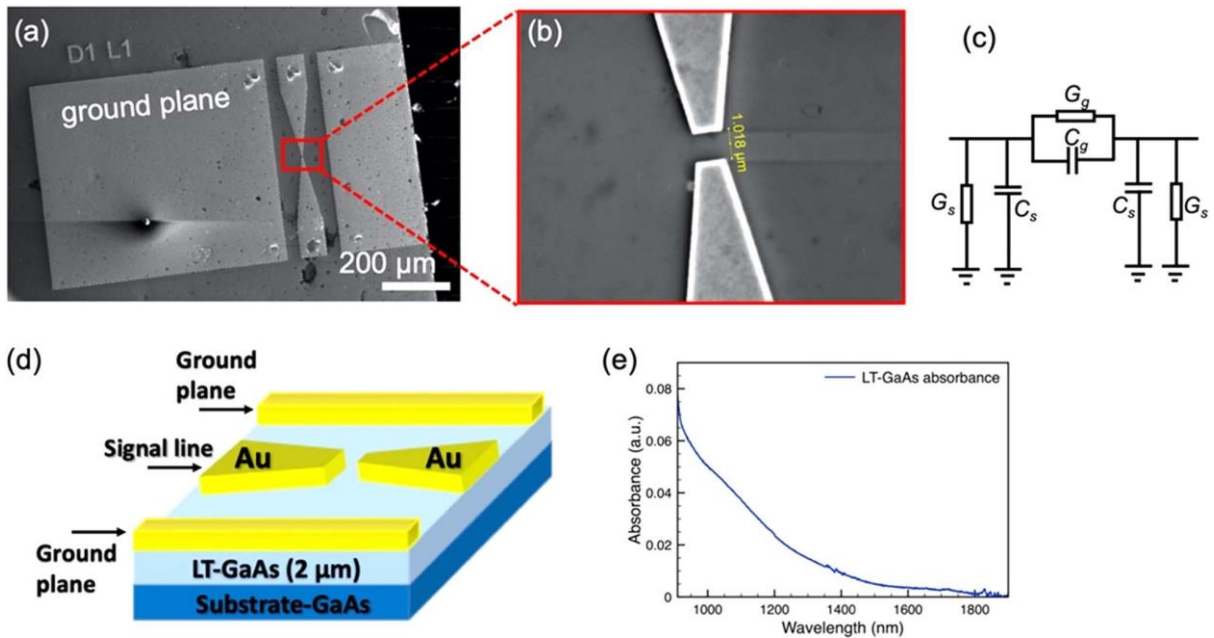


Figure 1: (a) Scanning electron microscopy (SEM) image of the LT-GaAs/GaAs photoconductive switch under study. (b) Zoom-in SEM image of the same device in (a) allowing a measurement of the gap distance. (c) Equivalent circuit model of such types of photoconductive switches. G and C refer respectively to conductance and capacitance, while the subscript of ‘ g ’ and ‘ s ’ refer respectively ‘gap’ and ‘shunt’. (d) The schematic representation of the device structure of the LT-GaAs/GaAs

photoconductive switch under study. (e) The optical absorbance of the LT-GaAs/GaAs sample under study in the near-infrared spectrum revealing limited optical density.

$$\text{with } S_{21}(\text{Off}) = \frac{j2\omega Z_0 C_g}{(1 + j2\omega Z_0 C_g)} \quad (2)$$

$$\text{and } S_{21}(\text{On}) = \frac{2Z_0 G_g (1 + j\omega C_g / G_g)}{(1 + 2Z_0 G_g)(1 + j\omega 2Z_0 C_g / (1 + 2Z_0 G_g))} \quad (3)$$

$$\text{and thus } |R_{\text{On/off}}| = \sqrt{\frac{(G_g^2 + C_g^2 \omega^2)(1 + 4C_g^2 Z_0^2 \omega^2)}{4C_g^4 Z_0^2 \omega^4 + C_g^2 (\omega + 2G_g Z_0 \omega)^2}} \quad (4)$$

where ω is the angular frequency in radians per second of the input electrical signal, Z_0 is the characteristic impedance of the input and output accesses of the device ($= 50 \Omega$), G_g and C_g is the gap conductance and gap capacitance described above, respectively.

The optical absorbance measured on our LT-GaAs/GaAs sample at $\lambda = 1.55 \mu\text{m}$ was found to be very small with an optical density ≤ 0.005 (**figure 1(e)**). Such sub-bandgap light absorption in LT-GaAs likely originates from defect (e.g. As defects) absorption³⁶. In order to render our LT-GaAs photoconductive switches responsive under $\lambda=1.55 \mu\text{m}$ illumination, we synthesized upconversion Er^{3+} -doped NaYF_4 nanocrystals by colloidal routes.

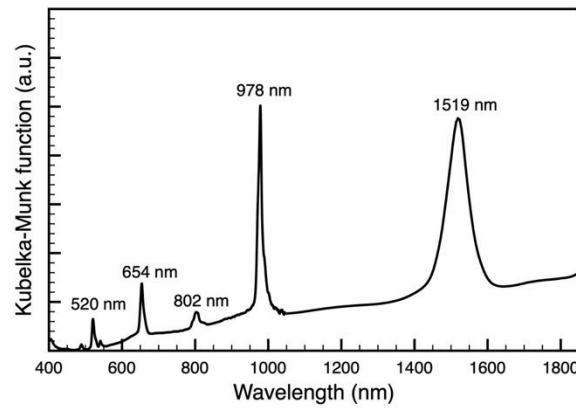


Figure 2: The Kubelka-Munk function obtained from the diffuse reflectance spectra on the Er^{3+} -

doped NaYF₄ nanocrystals deposited on a glass substrate, revealing qualitatively the optical absorption characteristics of these nanocrystals. The optical absorption coefficient (k) of the nanopowders can be considered to be proportional to the Kubelka-Munk function (k/s) under the assumption of scattering coefficient (s) being a constant.

The optical absorption of the Er³⁺-doped NaYF₄ nanocrystals can be verified qualitatively by measuring the diffuse reflectance spectra of the nanocrystal powders and the Kubelka–Munk function obtained from the diffuse reflectance spectra (**Figure 2** (available online at stacks.iop.org/NANO/32/45LT01/mmedia)). Revealed by SEM characterizations, these as-synthesized Er³⁺-doped NaYF₄ nanocrystals exhibit a uniform morphology, with an average crystal dimension of 416 nm±26 nm (**figure 3(a)**). Powder x-ray diffraction confirmed that these nanocrystals are highly crystalline with a pure hexagonal β -NaYF₄ phase (in good agreement with JCPDS no. 00-016-0334) (**figure 3(b)**). Importantly, under $\lambda=1.55 \mu\text{m}$ laser excitation, five strong fluorescence peaks were observed with their peak intensity located at wavelengths of $\lambda=525 \text{ nm}$, 544 nm, 658 nm, 806 nm, and 979 nm, respectively (**figure 3(c)**). The upconversion mechanism can be approximated through the electronic transitions depicted in **figure 3(d)**, where the Er³⁺ dopants act as both the sensitizers (responsible for optical absorption at $\lambda = 1.55 \mu\text{m}$) and emitters. For example, the fluorescence emissions at $\lambda = 525 \text{ nm}$, 544 nm and 658 nm require a three-photon absorption process and subsequent de-excitation transitions from the ²H_{11/2}, ⁴S_{3/2}, and ⁴F_{9/2} states to ⁴I_{15/2}, respectively. By comparison, the fluorescence emissions with their maximum located at $\lambda = 806 \text{ nm}$ and 979 nm involve a TPA process and de-excitation from ⁴I_{9/2} and ⁴I_{11/2} to ⁴I_{15/2}, respectively. By a previously-established method employing an integrating sphere³³, the fluorescence quantum yield of the current Er³⁺-doped NaYF₄ nanocrystals under $\lambda = 1.55 \mu\text{m}$ (at 45 mW) was measured to be about 2.5%. From the measured fluorescence emissions of these nanocrystals under $\lambda = 1.55 \mu\text{m}$ excitation as shown in **figure 3(c)**, one can see that the majority of them, such as the fluorescence peaks at $\lambda = 525, 544, 658, \text{ and } 806 \text{ nm}$, can largely overlap with the bandgap and above-bandgap absorptions of LT-GaAs. Such an overlap between the nanocrystal fluorescence emissions and the optical absorption of LT-GaAs suggests efficient resonant energy transfer rates between the two materials upon $\lambda = 1.55 \mu\text{m}$ photoexcitation (**figure 3(d)**), which enables the nanocrystal/LT-GaAs hybrid

photoconductive switch to response under such illumination.

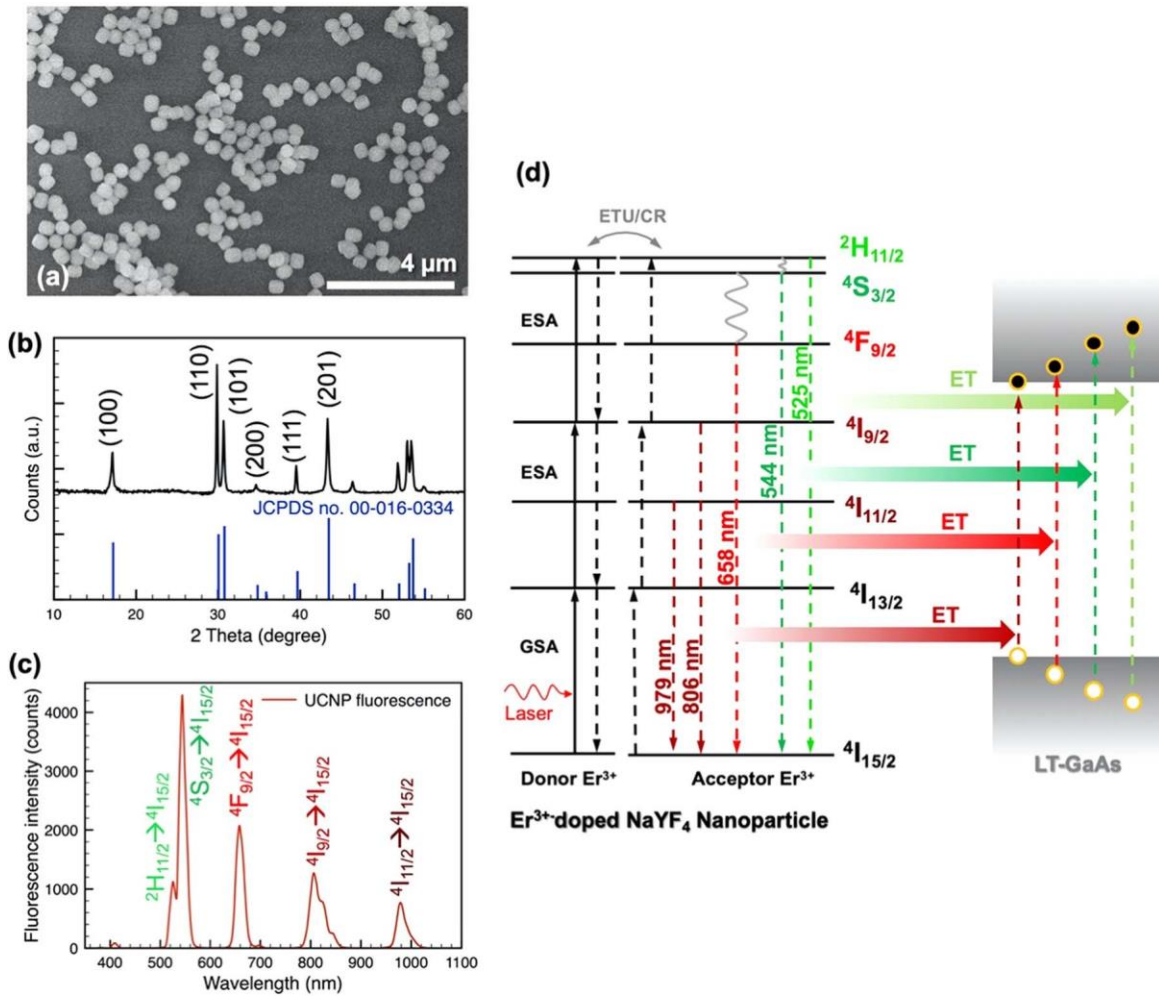


Figure 3 : (a) SEM image, (b) power x-ray diffraction pattern, and (c) the fluorescence spectrum under $\lambda = 1.55 \mu\text{m}$ laser excitation (power $\sim 45 \text{ mW}$) of the Er^{3+} -doped NaYF_4 nanocrystals synthesized in this work. (d) Schematic illustrating the energy transitions leading to the upconversion fluorescence observed under $\lambda = 1.5 \mu\text{m}$ photoexcitation.

ETU = energy-transfer upconversion, GSA = ground-state absorption, CR = cross-relaxation, ESA = excited-state absorption, and ET = energy transfer.

Chapter 4 Colloidal upconversion nano crystals enable low-temperature grown GaAs photovonductive switch operating at $\lambda=1.55 \mu\text{m}$

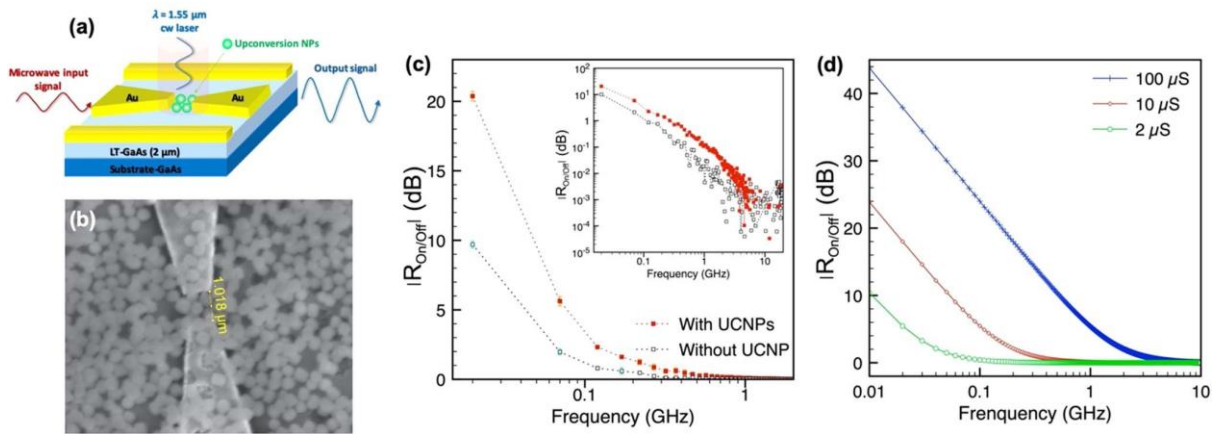


Figure 4: (a) Schematic of the hybrid upconversion Er^{3+} -doped NaYF_4 nanocrystals/LT-GaAs photoconductive switch where the upconversion energy transfer between the nanocrystals and the LT-GaAs enables the optical control of microwave signal transmission under $\lambda = 1.55 \mu\text{m}$ illumination. (b) SEM image of the gap region of the hybrid nanocrystal/LT-GaAs photoconductive switch. (c) Plot of the ON/OFF ratio ($|R_{\text{On/Off}}|$) of the hybrid upconversion nanocrystal/LT-GaAs photoconductive switch with versus frequency for a $\lambda = 1.55 \mu\text{m}$ laser illumination with a power of 45 mW (power density $\sim 12.9 \text{ mW } \mu\text{m}^{-2}$). Error bars represent standard deviation. Inset shows the best $|R_{\text{On/Off}}|$ data plotted in logarithm scale up to 20 GHz. (d) Simulated $|R_{\text{On/Off}}|$ over input frequency for different values of G_g induced by illumination ($G_g = 100 \mu\text{S}$, $10 \mu\text{S}$, and $2 \mu\text{S}$ respectively for blue, red, and green symbols), considering a fixed C_g value of 10 fF and a dark conductance $G_{g,\text{dark}}$ of 10 pS.

The Er^{3+} -doped NaYF_4 nanocrystals were then carefully deposited onto the LT-GaAs photoconductive switch (the resultant device configuration is shown in **figure 4(a)**). After deposition, a uniform film of Er^{3+} -doped NaYF_4 nanocrystals, containing a mono- to bi-layers of nanocrystals, was observed by SEM on these devices (**figure 4(b)**). Between the 1 μm gap of the signal line, there were approximately nine Er^{3+} -doped NaYF_4 nanocrystals arranged under a bi-layer configuration but only four of them were in the bottom layer and in direct contact with the LT-GaAs underneath (**Figure 5**). As the theoretical Förster resonance energy transfer rate decays rapidly ($\propto 1/r^6$, r = distance) over the distance between the (energy) donor and the acceptor. Here, we therefore estimate that the four bottom layer nanocrystals are the main agents responsible for optical absorption and energy transfer to the LT-GaAs underneath upon $\lambda = 1.55 \mu\text{m}$ photoexcitation.

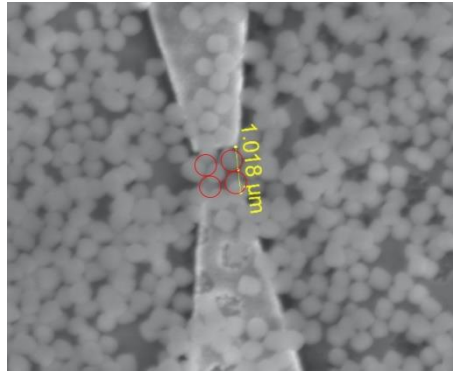


Figure 5: SEM image of the gap region of the hybrid Er^{3+} -doped NaYF_4 nanocrystals/LT-GaAs photoconductive switch under study. Red circles indicate the 4 nanocrystals located at the bottom layer (in direct contact with LT-GaAs) and inside the gap region.

Interestingly, even with such a limited number of Er^{3+} -doped NaYF_4 nanocrystals located in the gap and in direct contact with LT-GaAs, the energy transfer from the nanocrystals to LT-GaAs was important enough to result in a significant increase of gap conductance of LT-GaAs which contributes to the microwave transmission ON/OFF ratio ($|R_{\text{On/Off}}|$). **Figure 4(c)** shows the evolution of the $|R_{\text{On/Off}}|$ over the input microwave signal frequency under a CW $\lambda = 1.55 \mu\text{m}$ laser illumination (power density $\sim 12.9 \text{ mW } \mu\text{m}^{-2}$). Simultaneous measurements of identical samples with and without UCNPs are necessary to differentiate the optical upconversion process compared to natural TPA occurring in LT-GaAs layer at the operating wavelength. The functioning of these photoconductive switch devices can be understood as follows: microwave frequency band operation is directly governed by the C_g/G_g product of the device or precisely by G_g if the value of C_g is fixed. This tunable cut-off frequency behavior controlled by light absorption is validated by feed-back circuit simulations^{34,37} performed with the Keysight Advanced Design System software applying different values of G_g , as depicted in **figure 4(d)**, considering a fixed C_g value of 10 fF and a dark conductance $G_{g,\text{dark}}$ of 10 pS. The simulation input value of C_g has been taken from previous calculations and measurements on devices of similar dimensions.³⁸⁻³⁹ For $G_{g,\text{dark}}$, calculations have been done applying the substrate dark resistivity value integrated in space considering at light/matter interaction volume during excitation. As the frequency of the input signal increases, the ON/OFF ratio of both devices (with and without UCNPs) decrease and eventually converge together at the frequency beyond 3 GHz (**figure 4(c)**). This can be

explained by the reduced gap capacitance reactance as the frequency (f) increases. If one considers the equivalent electrical elements modeling the gap itself, such as the RC parallel circuit shown in **figure 1(c)**, as frequency increases, it appears that total impedance of the circuit will be progressively dominated by the capacitance reactance instead of the resistance. Nevertheless, in a quasi-DC regime at low frequency, i.e. such as at an input signal frequency of 20 MHz, a maximum ON/OFF ratio reaching 20.6 dB was measured on the nanocrystal/LT-GaAs sample (**figure 4(c)**), which represents a more than 2-fold larger value in decibel (or > 11-fold larger in absolute value) by comparison to the control device without UCNPs. Throughout the whole frequency range between 20 MHz up to about 3 GHz, one can clearly observe an increase of ON/OFF ratio due to the existence of the photoexcited upconversion nanocrystals (inset of **figure 4(c)**). This clearly indicates the effect of the increase gap conductance in LT-GaAs thanks to the energy transfer from the four Er^{3+} -doped NaYF_4 nanocrystals located inside the gap upon photoabsorption at $\lambda = 1.55 \mu\text{m}$. The measurement results of another device with a larger gap distance ($2.08 \mu\text{m}$) and five UCNPs located inside the gap was shown in **figure 6**. Due to the effect of the larger gap distance and the resultant larger gap capacitance⁴⁰, a slightly smaller ON/ OFF ratio of this device was observed by comparison to the device shown **figures 4(b) and (c)**. Nevertheless, the same trend of enhancement in the measured ON/OFF ratio was observed between the situation with and without UCNPs under $\lambda = 1.55 \mu\text{m}$ laser illumination, highlighting the upconversion effect of the UCNPs on the hybrid device. The maximum ON/OFF ratio of 20.6 dB measured on the current upconversion nanocrystal/LT-GaAs photoconductive switch is comparable to that measured previously on photo- conductive switch based on exfoliated black phosphorus²³ and GaNASb ²², while the current device gains advantage in terms of simplified fabrication thanks to the solution-processability of the colloidal nanocrystals.

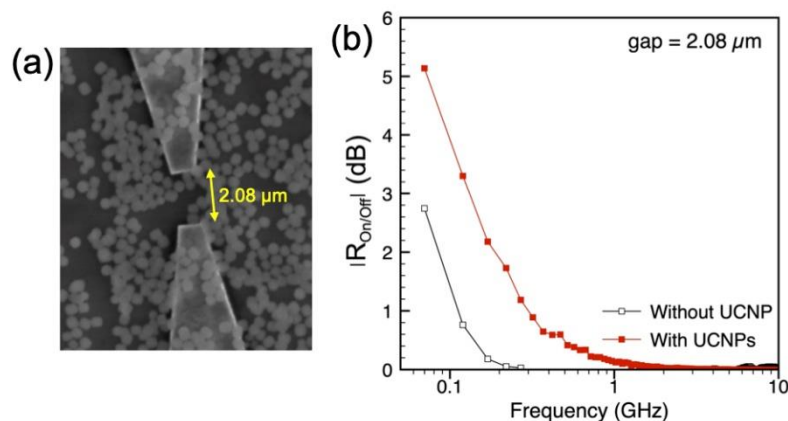


Figure 6: (a) SEM image of the gap region of another hybrid nanocrystal/LT-GaAs photoconductive switch (with a gap distance of $2.08 \mu\text{m}$). (c) Plot of the ON/OFF ratio ($|R_{\text{On/Off}}|$) of this hybrid upconversion nanocrystal/LT-GaAs photoconductive switch with versus frequency for a $\lambda = 1.55 \mu\text{m}$ laser illumination with a power of 45 mW (power density $\sim 12.9 \text{ mW } \mu\text{m}^{-2}$).

4.4 Conclusion

In this work, we propose an alternative approach to achieve microwave photoconductive switches functional at $\lambda = 1.55 \mu\text{m}$ illumination by the use of solution-processed colloidal upconversion nanocrystals deposited directly onto LT-GaAs. For this purpose, Er^{3+} -doped NaYF_4 nanocrystals were synthesized by colloidal routes resulting in uniform morphologies and dimensions together with a pure hexagonal $\beta\text{-NaYF}_4$ phase. Under $\lambda = 1.55 \mu\text{m}$ laser excitation, on these nanocrystals, five strong fluorescence peaks were observed with their peak intensity located at wavelengths of $\lambda = 525 \text{ nm}$, 544 nm , 658 nm , 806 nm , and 979 nm , respectively, among which the first four fluorescence emission peaks can overlap largely with the optical absorption of LT-GaAs suggesting efficient resonant energy transfer. Hybrid Er^{3+} -doped NaYF_4 nanocrystal/LT-GaAs photoconductive switch was then fabricated, with four Er^{3+} -doped NaYF_4 nanocrystals located inside the gap of the photoconductive switch and in direct contact with LT-GaAs. Under a CW $\lambda=1.55 \mu\text{m}$ laser illumination (power density $\sim 12.9 \text{ mW } \mu\text{m}^{-2}$), thanks to the upconversion energy transfer from the nanocrystals, a significant increase of ON/OFF ratio was observed in the upconversion nanocrystal/LT-GaAs hybrid device. A maximum ON/OFF ratio reaching 20.6

dB was measured on the hybrid device at an input signal frequency of 20 MHz. Such an ON/OFF ratio was more than 2-fold higher in decibel (or > 11-fold higher in absolute value) by comparison to the control device without UCNPs. Together with the advantage of solution-processing, the current Er^{3+} -doped NaYF_4 nanocrystal/LT-GaAs photoconductive switch by photon upconversion represents a novel solution-processed path to achieve optical control of microwave signals by $\lambda = 1.55 \mu\text{m}$ illumination.

4.5 References

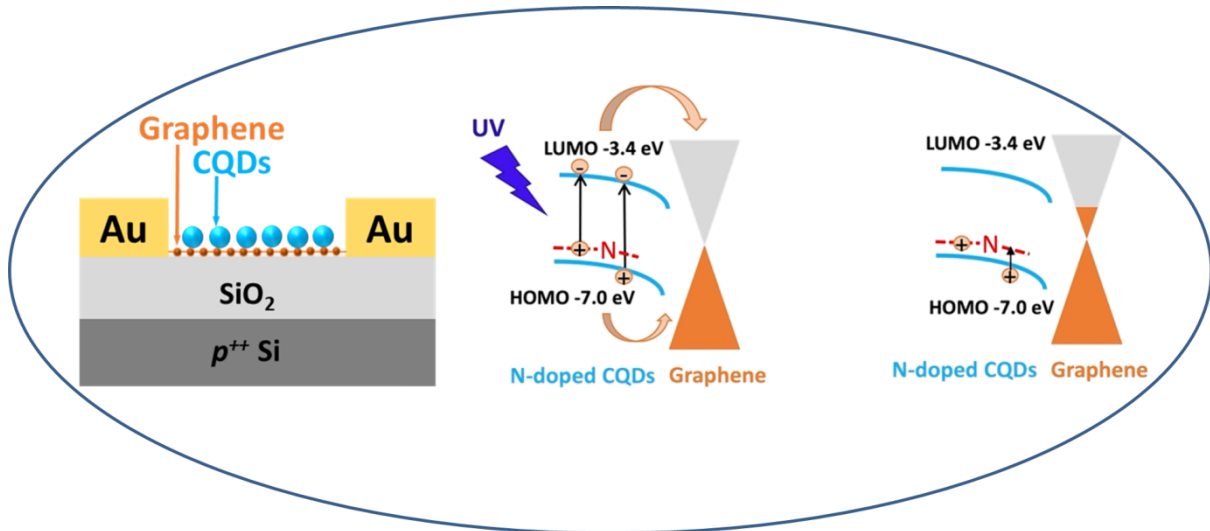
1. Andersson I and Eng S T 1987 ESSDERC '87 17th Eur. Solid State Device Res. Conf. (Bologna, Italy) pp 1073–6 <https://ieeexplore.ieee.org/document/5436836/citations#citations>
2. Andersson I and Eng S T 1987 Solid. State. Electron. 30 133
3. Leonberger F J and Moulton P F 1979 Appl. Phys. Lett. 35 712
4. Platte W and Appelhans G 1976 Electron. Lett. 12 270
5. Auston D H 1975 Appl. Phys. Lett. 26 101
6. Lawton R A and Scavanne A 1975 Electron. Lett. 11 74
7. Johnson A and Auston D 1975 IEEE J. Quantum Electron. 11 283
8. Auston D H, Johnson A M, Smith P R and Bean J C 1980 Appl. Phys. Lett. 37 371
9. Antonetti A, Migus A, Malley M M and Mourou G 1977 Opt. Commun. 21 211
10. Low A J and Carroll J E 1978 IEE J. Solid-State Electron Devices 2 185
11. LeFur P and Auston D H 1976 Appl. Phys. Lett. 28 21
12. Lee C H 1977 Appl. Phys. Lett. 30 84
13. Proud J M and Norman S L 1978 IEEE Trans. Microw. Theory Tech. 26 137
14. Mourou G, Stancampiano C V and Blumenthal D 1981 Appl. Phys. Lett. 38 470
15. Paulus P, Brinker W and Jager D 1986 IEEE J. Quantum Electron. 22 108
16. Lee Y-S 2008 Principles of Terahertz Science and Technology (Boston, MA: Springer US) pp 1–66
17. Smith F W, Le H Q, Diadiuk V, Hollis M A, Calawa A R, Gupta S, Frankel M, Dykaar D R, Mourou G A and Hsiang T Y 1989 Appl. Phys. Lett. 54 890
18. Delord J-M, Roux J-F, Coutaz J-L, Canseliet C, Krotkus A, Formont S and Chazelas J 2007 2007 Eur. Conf. Lasers Electro-Optics Int. Quantum Electron. Conf. (Piscataway, NJ: IEEE) p 1
19. Urata K M, R, Miller D A B and Harria J S 2004 IEEE J. Quantum Electron. 40 800
20. Erlig H, Wang S, Azfar T, Udupa A, Fetterman H R and Streit D C 1999 Electron. Lett. 35 173

Chapter 4 Colloidal upconversion nano crystals enable low-temperature grown GaAs photovonductive switch operating at $\lambda=1.55 \mu\text{m}$

21. Schlesinger T E 2001 Encyclopedia of Materials: Science and Technology (Oxford: Elsevier) pp 3431–5
22. Tan K H et al 2010 IEEE Photonics Technol. Lett. 22 1105
23. Penillard A, Tripon-Canseliet C, Rosticher M, Maksimovic I, Liu Z and Géron E 2016 J. Appl. Phys. 119 024506
24. Xiang H, Hu Z, Billot L, Aigouy L, Zhang W, McCulloch I and Chen Z 2019 ACS Appl. Mater. Interfaces 11 42571
25. Schäfer H, Ptacek P, Eickmeier H and Haase M 2009 Adv. Funct. Mater. 19 3091
26. Ghosh P and Patra A 2008 J. Phys. Chem. C 112 3223
27. Zhao J J, Sun Y, Kong X, Tian L, Wang Y, Tu L, Zhao J J and Zhang H 2008 J. Phys. Chem. B 112 15666
28. Wang F, Han Y, Lim C S, Lu Y, Wang J, Xu J, Chen H, Zhang C, Hong M and Liu X 2010 Nature 463 1061
29. Auzel F 2004 Chem. Rev. 104 139
30. Zhang X et al 2017 Adv. Mater. 29 1604431
31. Zhao X, Song L, Zhao R and Tan M C 2019 ACS Appl. Mater. Interfaces 11 2344
32. Xiang H, Zhou L, Lin H-J, Hu Z, Zhao N and Chen Z 2020 Nanotechnology 31 495201
33. Faulkner D O, McDowell J J, Price A J, Perovic D D, Kherani N P and Ozin G A 2012 Laser Photon. Rev. 6 802
34. Faci S, Tripon-Canseliet C, Algani C, Deshours F, Alquie G, Formont S and Chazelas J 2005 2005 Eur. Microw. Conf. (Piscataway, NJ: IEEE) p 4
35. Andersson I L and Eng S T 1989 IEEE Trans. Microw. Theory Tech. 37 729
36. Jooshesh A, Fesharaki F, Bahrami-Yekta V, Mahtab M, Tiedje T, Darcie T E and Gordon R 2017 Opt. Express 25 22140
37. Tripon-Canseliet C and Chazelas J 2014 Nanoscale Microwave Engineering (Hoboken: Wiley) (<https://doi.org/10.1002/9781118925386>)
38. Tripon-Canseliet C et al 2016 Electron. Lett. 52 237
39. Simons R N 2001 Coplanar Waveguide Circuits, Components, and Systems (New York: Wiley) (<https://doi.org/10.1002/0471224758>)
40. Tripon-Canseliet C, Faci S, Pagies A, Magnin V, Formont S, Decoster D and Chazelas J 2012 J. Light. Technol. 30 3576

Chapter 5

N-Doped Carbon Quantum Dots on Graphene for Field-Effect Transistor Optoelectronic Memories



Resume

Le développement de mémoires optoélectroniques non volatiles à base de transistors à effet de champ (FET) est vital pour les innovations nécessaires à l'amélioration de nos systèmes informatiques. Dans ce travail, pour la première fois, nous avons exploité les propriétés uniques de piégeage et de rétention des charges des points quantiques de carbone (CQD) colloïdaux dopés à l'azote (dopés N) traités en solution pour réaliser des mémoires optoélectroniques fonctionnelles programmables par illumination UV et avec une possibilité d'écriture multi-niveaux. En particulier, une fonction mémoire durable peut être obtenue grâce aux vastes sites de piégeage de trous fournis par ces CQDs et à l'effet de photo-gating résultant exercé sur le FET en graphène, tandis que l'effacement de la mémoire peut être réalisé via une polarisation positive de la grille qui fournit suffisamment de porteurs pour la recombinaison des charges. Cette étude met en évidence la possibilité de concevoir des mémoires optoélectroniques non volatiles à base de FET tout-carbone de haute performance en manipulant et en couplant les propriétés de piégeage de charge des CQD colloïdaux et du graphène.

5.1 Introduction

Innovations on memory components are essential to improve the current computer system, the performance of which is limited by the "von Neumann bottleneck".^{1,2} As the developments of Internet of Things (IoT) and big data processing are growing rapidly, there is a high demand for solutions towards ultrahigh-density non-volatile storage. Towards the development of high-performance memories, much research effort are currently being carried out, leading to the achievements on different types of non-volatile memories such as capacitor-type memories, resistor-based memories, and transistor-based memories.³ A major workhorse of transistor-based memories is composed of floating-gate field-effect transistors (FETs) which show advantages in terms of reliability, scalability, power consumption, non-volatility, and compatibility. They lead to the formation of non-volatile flash memories which are compatible to the complementary metal-oxide-semiconductor (CMOS) technology. In this field of non-volatile flash memories, while silicon-based memories have played a significant role so far,⁴ in order to overcome the limits of this technology, further research is still needed to identify new material and device systems alternative to silicon-based memories with new abilities to combine characteristics such as low material cost, without heavy-metal toxic elements, adaptability in large-area fabrication, mechanical flexibility, and low-power consumption.^{3,5-7}

In this regard, colloidal nanocrystals or nanoparticles have aroused much interest to serve as the charge-trapping or charge-retaining material in non-volatile memory devices.^{8,9} This is due to either their rich surface properties providing abundant charge traps¹⁰⁻¹⁴ and/or different available engineering approaches leading to formation of core-shell^{12,15} or other nanoparticle/dielectric structures^{7,12} all of which capable to secure and store charges within the nanoparticle. In addition, many direct-bandgap semiconductor nanoparticles possess strong light absorption coefficients together with absorption/emission properties tunable by synthetic controls either over their dimension or surface properties. These particular properties were thus harnessed to achieve FET-based optoelectronic memories, where the programming and/or erasing are attained by light illumination instead of by electrical bias. Such optoelectronic memories therefore exhibit advantages in terms of

power consumption and compatibility with optical circuits and artificial neuromorphic applications.¹⁶⁻²⁰ Motivated by these benefits, over the past years, attempts were made by cadmium and zinc chalcogenide QDs and related core/shell structures,^{12,15} rare-earth-doped upconversion fluoride nanocrystals,²¹ perovskite quantum dots (QDs),²² as well as TiO₂ dielectric nanoparticles²³ to achieve functional FET-based optoelectronic memories. For example, by embedding Yb³⁺/Er³⁺-co-doped NaYF₄ colloidal nanocrystals inside a layer of poly(3-hexylthiophene) within a FET architecture, Zhou et al. demonstrated flexible multilevel optoelectronic memories programable by near-infrared illumination at $\lambda = 980$ nm.²¹ Nevertheless, rare-earth materials are not sustainable and their low absorption coefficient limits the responsivity of the device. Other similar examples, programable by visible illumination, were also demonstrated by organic conjugated molecules and polymers.^{24,25} Yet, typically, a relatively large lateral source-drain bias (e.g. > 10 V) is necessary for their functioning. In addition to optoelectronic memories that utilize visible illumination, ultraviolet (UV)-triggered memories can exhibit advantages avoiding interference from solar irradiation and indoor lighting.²⁶ Towards this direction, Han et al. sandwiched charge-trapping CdSe/ZnS core-shell QDs between dielectric layers to achieve flexible UV-controlled FET-based photonic memories.¹² Star et al. applied CVD-grown carbon nanotubes for charge storage in a polymer thin film FET leading to UV-writable optoelectronic memories.⁷ On both examples, besides the source-drain voltage, typically an important gate bias is also necessary to work together with the UV illumination to achieve programming. Recently, Sun et al. decorated the surface of graphene FETs by nitrogen-doped-TiO₂ nanocrystals to achieve highly promising UV-writable multilevel optoelectronic memories which exhibit negligible current loss ten hours after UV programming.²³ While these nitrogen-doped-TiO₂ nanocrystal-based optoelectronic memories are highly encouraging, the synthesis of such TiO₂ nanocrystals required flammable and dangerous precursor (titanium(IV) butoxide) due to its high sensitivity to air and moisture. Towards the further development of this field, alternative solution-processed material candidates with environmentally benign and stable characteristics can potentially lead to further progresses.

To this aim, colloidal carbon quantum dots (CQDs),^{27,28} highly luminescent nanoparticles of carbon, one of the most abundant elements in our planet, could be excellent candidates. They can be readily synthesized by various natural carbon sources such as citric acid,²⁹

orange peels,³⁰ and pomegranate³¹ together with relatively mild synthesis temperature (≤ 200 °C) by hydrothermal, solvothermal or microwave routes, giving nanoparticles with dimensions ranging from a few to a few tens of nanometers. Instead of controlled by their nanoparticle dimension, their optical properties are controlled by their rich surface chemical groups which can be tuned from the synthetic routes and the choice of reactants.^{32,33} Attracted by their favourable properties such as high optical absorbance and fluorescence, chemical stability, biocompatibility, and low toxicity,^{34,35} previous works have successfully applied them in bio-imaging,³⁶ drug delivery,³⁷ photocatalytic conversion,³⁸ and photovoltaic devices.^{39–41} Towards FET-base memories, Zhang et al. has embedded CQDs inside the active layer of polyvinyl pyrrolidone (PPV)-based FET.⁴² Nevertheless, such CQD/PPV FET-memories are not optically enable and the programming of which necessities a high electrical bias (60 V). To our best knowledge, there is not yet any demonstration by applying colloidal CQDs in optoelectronic memories. Herein, for the first time, we harnessed the unique charge-trapping and retention properties of solution-processed nitrogen-doped (N-doped) CQDs to achieve functional UV-enable and visible-blind optoelectronic memories with multilevel writing possibilities. These memories are achieved by combining the optical and charging-trapping properties of CQDs and the resultant photo-gating effect on graphene FETs. After UV-programming, prolonged charge retention can be obtained exhibiting > 96 % of its initial programmed photocurrent value for a period of 10 hours and can be erased with a positive gate bias. Together with their facile colloidal synthesis, abundant nature, environmental-friendly compositions, and their excellent memory functionalities, these fully carbon-base non-volatile optoelectronic memories thus provide bright perspectives for the further development of this field.

5.2 Experimental

Synthesis of colloidal CQDs. N-doped CQDs were synthesized by a previously reported hydrothermal route.³⁴ Citric acid (1.0507g) and ethylenediamine (EDA, 335 μ L) was dissolved in 10 mL of deionized (DI) water under vigorous stirring for 30 minutes. The resultant precursor solution was poured into a poly(tetrafluoroethylene) (PTFE)-lined autoclave. After

sealing the autoclave, it was placed in an oven at 200 °C for 5 hours. The autoclave was then allowed to naturally cool down to room temperature. The resulting product was a transparent brown-color solution containing CQDs. To purify these CQDs, dialysis was performed in 2K molecular-weight cut off (MWCO) dialysis cassettes in DI water for 48 hours. For the purpose of comparison, CQDs without nitrogen doping were also synthesized according to a previously published procedure.³⁴ Their synthesis and purification procedures were identical to those stated above on N-doped CQDs except that the N-source, amine (EDA), was not added into the reaction.

Fabrication of CQDs/graphene FET-based optoelectronic memories. CVD-grown monolayer graphene on copper (Cu) foils was obtained from Graphene Semiconductor SLU. It is then transferred by a method established previously⁴³ onto heavily *p*-doped Si substrates on which a 300-nm-thick thermal SiO₂ layer as grown as the gate dielectrics. To perform the graphene transfer, poly(methyl methacrylate) (PMMA) was first dissolved in butyl-acetate with a concentration of 40 mg/mL. This PMMA solution was then spun onto the graphene/Cu sample at a spin speed of 2000 rpm for 120 seconds followed by solvent drying at 80°C for 30 minutes. PMMA-protected graphene/Cu foil was then cut into a desired dimension large enough to build the FETs mentioned below. They were then carefully placed onto the surface of an etchant formed by 10 wt% of FeCl₃ aqueous solution in order to dissolve entirely the Cu foil, leaving the PMMA-protected graphene film floating on the solution's surface. The PMMA/graphene layer was then transferred (with the help of a glass slide) onto three different clean DI-water baths to remove residual etchant for a duration of 10 minutes in each bath. A thoroughly cleaned Si/(300-nm)SiO₂ substrate was then dipped into the last water bath to pick up the floating PMMA/graphene layer, resulting in a smooth film on the Si/SiO₂ surface. This sample was then allowed for a > 12-hour heat treatment at 150 ° C to promote graphene adhesion onto the substrate. After cooled down to room temperature, the PMMA layer of the sample was removed by acetone rinsing. After graphene transfer, gold source and drain electrodes were then thermally evaporated through a shadow mask onto the graphene layer, defining a conductive channel with a channel width (W) and length (L) dimension of W = 3 mm and L = 0.25 mm. A drop (about 36 μL) of CQD DI-water solution with a concentration of about 12 mg/ml was then drop-casted onto the surface of graphene FET followed by drying off the solvent in air.

Material and device characterization methods. Transmission electron microscopy (TEM) characterizations were performed by a JEOL 2010 TEM microscope operated at 200 kV. UV-Visible absorbance measurements were performed by a JASCO V770 UV-Vis spectrometer. Excitation-dependent photoluminescence and photoluminescence excitation (PLE) spectra of N-doped CQD solutions were obtained by a Edinburgh Instruments FLS900 Fluorescence spectrometer. Fourier-transform infrared (FT-IR) spectroscopy was measured on CQDs by a PerkinElmer Spectrum Two instrument in an attenuated total reflection (ATR) infrared mode. The Raman spectrum of CQDs was obtained by a Anton Paar Cora 5001 Raman spectrometer with a $\lambda = 785$ nm laser. Atomic force microscopy (AFM) characterizations were performed by a Bruker Dimension Icon atomic force microscope in tapping mode. X-ray diffraction (XRD) spectrum was measured on CQDs deposited onto a glass substrate by a PANalytical X'Pert X-ray diffractometer (with Cu-K α radiation). Graphene FET (before CQD deposition) and CQD-decorated graphene FET-base memories were placed in a probe-station in vacuum (with a transparent top window allowing illumination when necessary) where their current/voltage and current-time characteristics were measured by a computer-controlled Keithley 2634 source measurement unit (SMU). To program the memories under test, an UV LED lamp ($\lambda = 365$ nm) from Ocean Optics with a fiber-coupled output was shed onto the device through the top window. To measure the transfer characteristics, light illumination at different irradiance was kept for one minute before measurement.

5.3 Results and discussion

The N-doped CQDs under study were synthesized by a reported hydrothermal route with mild synthesis temperature (200 °C) by condensing citric acid together with EDA.³⁴ TEM images of as-synthesized N-doped CQDs exhibit nanoparticles with a diameter mainly between 2 - 10 nm (**Figure 1(a)**). When characterized by high-resolution TEM (HRTEM), some of them exhibit clear lattice fringes as the one shown in the inset of **Figure 1(a)**, where a 0.21-nm interplane distance can be measured corresponding well to the (100) plane distance in graphitized carbon (JCPDS no. 41-1487). When deposited onto a clean Si substrate, these N-doped CQDs reveal a typical height of 2 - 5 nm by AFM characterizations (**Figure 1(d) and (e)**), confirming the formation of nanoparticles with a few layer graphite-like structure. The XRD spectrum of these N-doped CQDs shows only a broad diffraction

peak at $2\theta \sim 21.5^\circ$ which is at a lower diffraction angle than the (001) diffraction expected for crystalline graphite ($2\theta = 26.4^\circ$, JCPDS no. 41-1487) (**Figure 1(c)**). This is likely due to the presence of a high disordering along the C-axis and/or the presence of surface groups enlarging the interplane distance along this axis. The above analysis is coherent with the Raman spectrum obtained on the current N-doped CQD water solution (**Figure 1(f)**), where two Raman bands, located at the Raman shift of 1355 cm^{-1} and 1645 cm^{-1} , can be observed and assigned as the D and G bands, respectively. The ratio between these two Raman bands (I_D/I_G), typically considered as an indicator of disordering and as the ratio between sp^3/sp^2 carbons,^{44,45} was measured to be ~ 3.2 on the current sample, suggesting graphite-like structure but with disordering to a large extent. In terms of optical properties, N-doped CQDs exhibit two major absorption peaks in the UV spectrum with one located at $\lambda \approx 256\text{ nm}$ and another broad peak located at $\lambda \approx 356\text{ nm}$ (**Figure 1(b)**), corresponding respectively to $\pi-\pi^*$ and $n-\pi^*$ transitions.^{46,47} Analysing the on-set of optical absorption by a Tauc plot allows us to determine the optical bandgap as $\sim 3.1\text{ eV}$ (**Figure 11**, shown in chapter 3). Strong blue photoluminescence can be observed when these N-doped CQDs are excited by different UV illuminations with a wavelength smaller than 400 nm (**Figure 1(b)**). At a longer excitation wavelengths with $\lambda > 400\text{ nm}$, the observed photoluminescence becomes negligible due to the limited absorption of the CQDs at the visible spectrum.

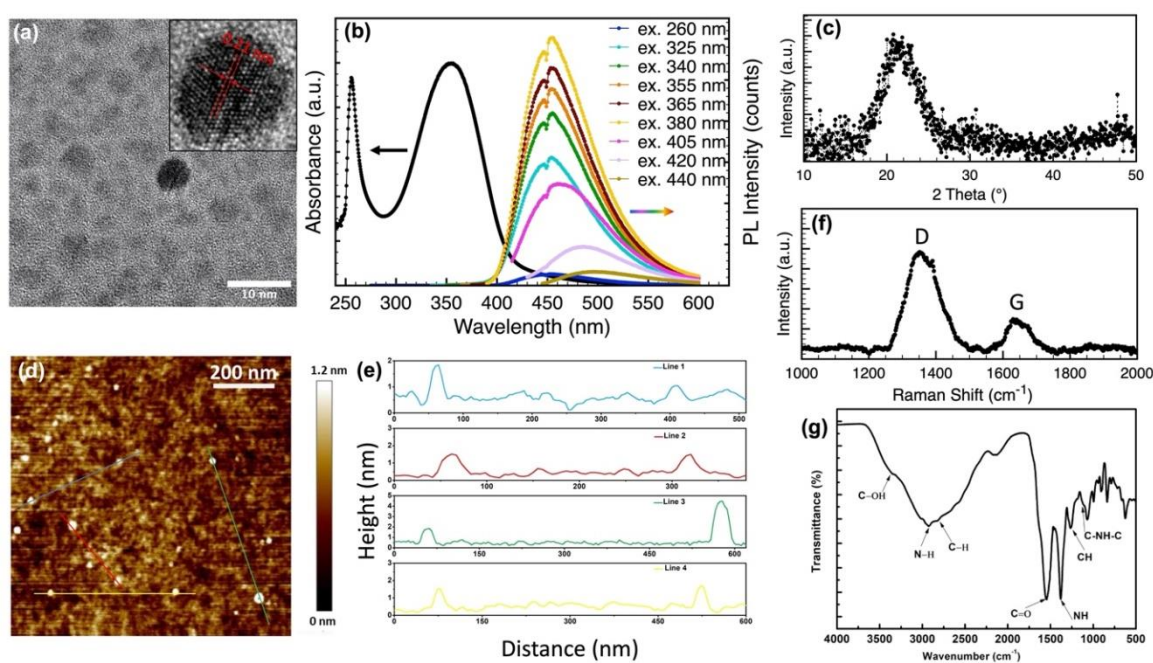


Figure 1: (a) TEM image of N-doped CQDs. The inset is the zoom-in view of the HRTEM image of a N-doped CQDs. (b) Optical UV-Visible absorbance and excitation wavelength dependant photoluminescence of N-doped CQDs in water solution. (c) XRD spectrum of as-synthesized N-doped CQDs. (d) AFM image of N-doped CQDs deposited onto a clean Si substrate and (e) the height profiles of the different lines in (d). (f) Raman spectrum of N-doped CQD solution in water under laser excitation of $\lambda = 785$ nm. (g) FT-IR transmission spectrum of N-doped CQDs.

At $\lambda = 365$ nm, the photoluminescence quantum yield of the N-doped CQDs in water was measured to be about 40%. The presence of EDA as a reactant in the N-doped CQD synthesis leads to the formation of N-doping, which was found to contribute to a higher photoluminescence quantum yield by comparison to CQDs synthesized without EDA.³⁴ According to previous XPS experiments,³⁴ nitrous carbon groups were previously identified together with oxygenated carbon and graphitic or aliphatic (C=C and C-C) carbon groups. This is coherent with our measured FT-IR spectrum on N-doped CQDs, where vibrations corresponding to C-OH and C-H stretching, C-NH-C asymmetric stretching, N-H bending, and C=O vibrational absorption can be identified (**Figure 1(g)**).

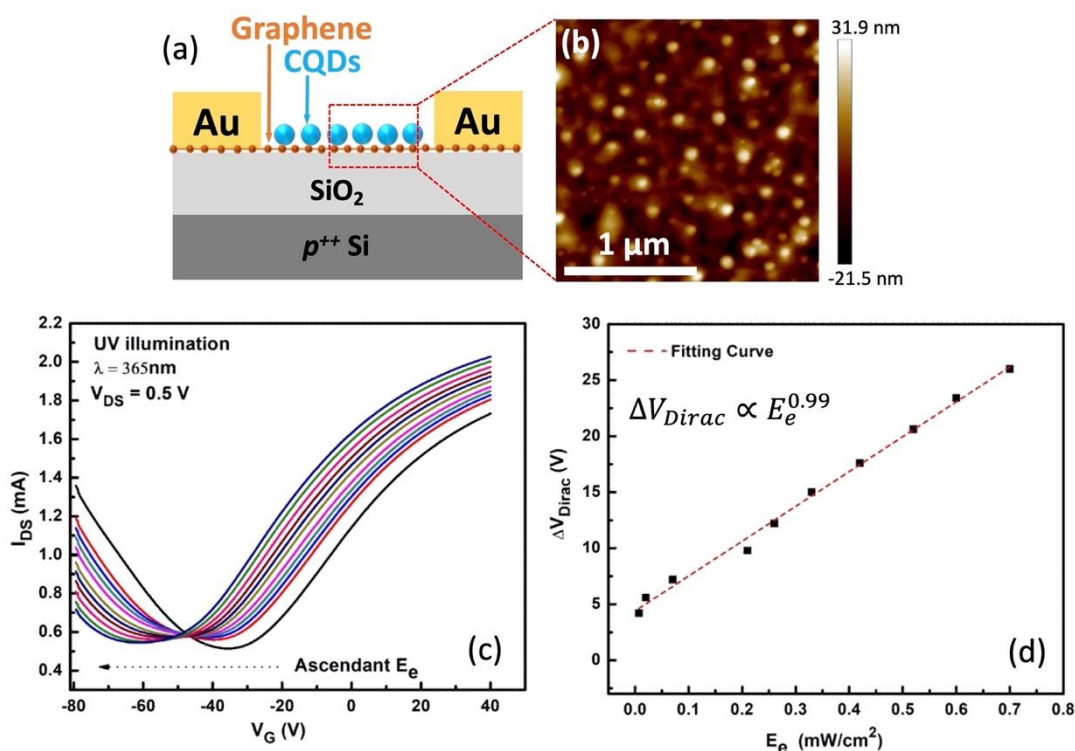


Figure 2: (a) Schematic of the CQD-decorated graphene FET-based optoelectronic memory device structure. (b) AFM image in an area inside the FET channel revealing the decoration of N-doped CQDs on top of the graphene. (c) Transfer characteristics of a N-doped CQD-decorated graphene transistor under UV illumination with a power density (E_e) of 0, 0.007, 0.02, 0.07, 0.21, 0.26, 0.33, 0.42, 0.52, 0.60, 0.70 mW/cm². The arrow indicates the shift direction of the transfer characteristics as E_e increases. (d) The shift of the Dirac point voltage (ΔV_{Dirac}) as E_e increases.

The device architecture of the N-doped CQD-decorated graphene FET-based memory was shown in Figure 2(a), where a bottom-gate-top-contact FET structure was applied. The Raman spectrum of the graphene transferred onto the Si/SiO₂ substrate suggested the existence of a single-layer graphene with a similar quality as previously reported CVD-grown graphene (**Figure 11**, shown in chapter 3).⁴⁸ After depositing N-doped CQDs on the surface of graphene, AFM characterizations inside the FET channel confirm well their existence, mostly as isolated nanoparticles and few-nanoparticle clusters (**Figure 2(b)**). Comparing the transfer characteristics of the graphene FET measured in dark before and after depositing N-doped CQDs, a shift of the Dirac point towards negative gate voltages was observed due to the deposition of N-doped CQDs (**Figure 14**, shown in chapter 3). Such a *n*-type doping behavior is likely due to the interactions between the surface groups and/or defects of the CQDs and the free charges inside the graphene FET channel. Importantly, the existence of N-doped CQDs enable a clear photoresponse of the graphene FET under UV illumination: A series of UV illuminations (at $\lambda = 365$ nm) of different power densities (E_a) was shone from above onto the N-doped-CQD-decorated device. As shown in **Figure 2(c)**, the UV illumination induced a further shift of the Dirac point of the transfer characteristics towards more negative gate voltages. The magnitude of this shift in Dirac point voltage increases as a larger E_a was applied and the direction of this shift also indicates a *n*-type doping behavior on the graphene due to the photoexcited N-doped CQDs. This observed UV-sensitivity is clearly different from that observed on graphene FETs without any CQDs, as the same device before depositing N-doped CQDs exhibited negligible shift in terms of Dirac point voltage under the UV illumination (**Figure 15**, shown in chapter 3). This thus confirms that the observed UV photoresponse should be attributed to the UV absorption by the N-doped CQDs and the interactions between the photoexcitation QDs and the graphene layer.

The shift of the Dirac point voltage (ΔV_{Dirac}) in the transfer characteristics of the N-doped-CQD device under different UV illumination power densities (E_a) with reference to the Dirac point measured in dark is plotted in Figure 2(d). In previous works of phototransistors and phototransistor-based memories,^{10,48–50} such a $\Delta V_{Dirac}-E_a$ relationship has been successfully modeled by power law with $\Delta V_{Dirac} = aE_a^\beta$, where α and β are both constants with β typically of values between 0 and 1. A β value much smaller than 1 can, for example, originate from a saturation of the charge transfer processes between the photo-absorber and the graphene as the illumination irradiance increases due to an increased extent of charge recombination offsetting the increased charge generation. Here, an exceptional near-linear relationship between ΔV_{Dirac} and E_a was observed with β fitted as 0.99 (**Figure 2(d)**), indicating a non-saturated photoresponse under the illumination irradiances of this study. Taken into account the HOMO and LUMO values measured previously³⁴ on similar N-doped CQDs and the observed shift of ΔV_{Dirac} over E_a , we attribute the physical mechanism behind the current N-doped CQD/graphene device as the photo-gating effect, equivalent to a change in terms of effective gate voltage due to the existence of light (**Figure 3**). Such a photo-gating effect has been observed in other hybrid graphene FET-based devices where the graphene was decorated or coupled with another photo-absorber such as PbS quantum dots,⁵¹ a perovskite halide layer,⁵² black phosphorus nanosheets,⁵³ and TiO₂ nanocrystals.¹⁰ Here, as shown in **Figure 3(a)**, upon UV absorption, while both types of photoexcited carriers in the N-doped CQDs can be transferred to graphene due to the favorable energy alignments, the observed *n*-type doping behavior upon illumination suggests a more significant electron transfer than hole transfer to the graphene. This is possible because holes may be transferred to the graphene either less efficiently or hindered by the existence of traps.⁵⁰ As N dopants were found previously forming mid-gap deep hole traps for other types of nanoparticles^{54–56} and the current CQDs are N-doped, we thus conjecture that the N-dopants in the current case should serve equally as hole traps. This will be further discussed below when we compare the device behavior with non-N-doped CQDs. As a consequence, the net remaining holes left behind the N-doped CQDs attract more electrons in the graphene due to coulomb interactions, leading to a more negative gate voltage to be necessary to reach the Dirac point of the FET (**Figure 3(b)**). The fact that a large and near-unity β was found above in the $\Delta V_{Dirac} - E_a$

relationship suggests the ample availability of hole traps in the N-doped CQDs so that the charge transfer processes are less limited by charge recombinations at the current irradiance range.

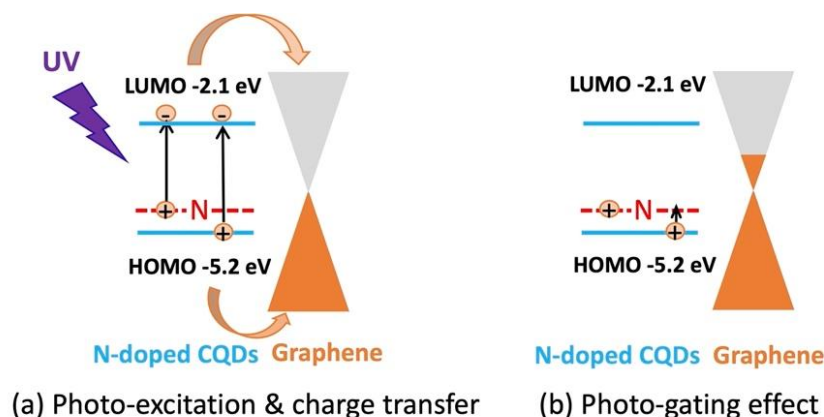
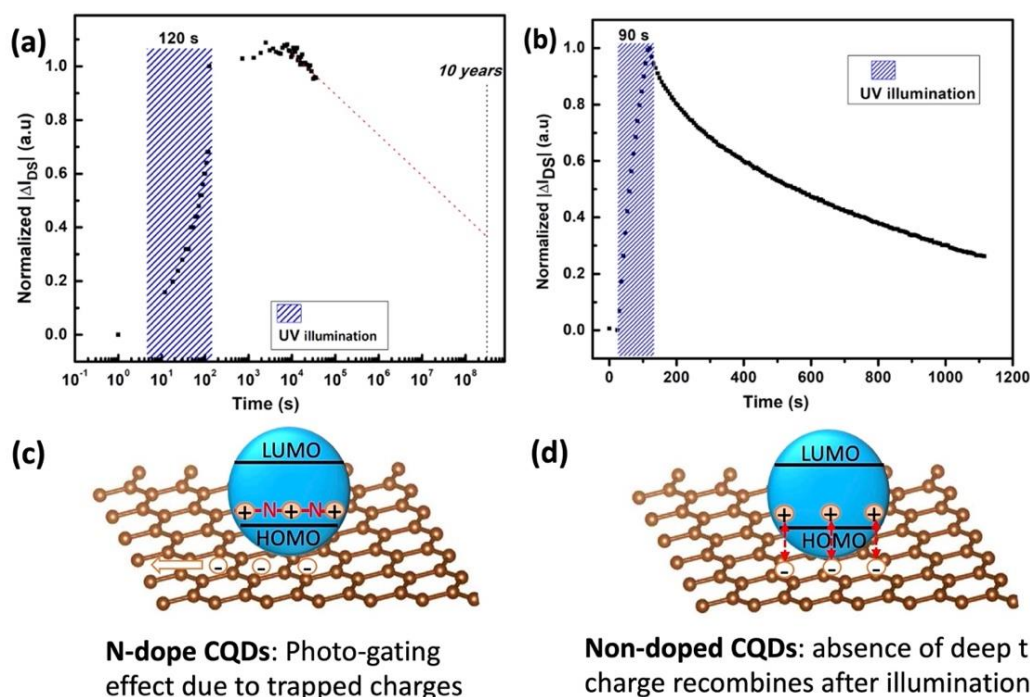


Figure 3: Schematic of (a) the photoexcitation in N-doped CQDs, the subsequent charge transfer processes between CQDs and graphene, and (b) the the photo-gating effect due to the remaining of one type of photo-excited carriers in CQDs.

Coherent with the photo-gating mechanism and nitrogen hole-trapping proposed above, in N-doped-CQD-decorated graphene devices an exceptional charge retaining behavior was observed (**Figure 4**). When the mobility remain unchanged (which is the case in **Figure 2(a)**), the Dirac point shift (ΔV_{Dirac}) triggered by UV illumination translates into photocurrents following the relation of $\Delta I_{DS} = \frac{W}{L} C_i \mu \Delta V_{Dirac} V_{DS}$ assuming the FET in the linear regime, where C_i is the capacitance per unit area of the gate dielectric, W and L are respectively the channel width and channel length, I_{DS} and V_{DS} are respectively the source-drain current and the source-drain voltage, and the photocurrent ΔI_{DS} is the change of I_{DS} triggered by illumination by comparison to the $I_{DS, dark}$ measured in dark. The evolution of ΔI_{DS} over time of the N-doped CQD device was monitored at a gate voltage $V_G = 0$ V and a source-drain voltage $V_{DS} = 0.5$ V while a UV light ($\lambda = 365$ nm, $E_a = 0.7$ mW cm⁻²) was shone onto the device from the top for a duration of 120 s. As shown in **Figure 4(a)**, upon UV illumination, a rapid increase of photocurrent was observed without any trend of saturation. Importantly, after the UV illumination being switched off, the I_{DS} was maintained at nearly the same programmed level with a slight further increasing trend (up to ~ 8%) during the

first two hours after switching off the light. Such a slight increase of I_{DS} is likely due to the device instability and/or bias-stress experienced by the device. Beyond this time window, the I_{DS} starts to decrease very slowly, reaching back to 96% of its initial value (i.e. the I_{DS} value right after switching off the light) ten hours after switching off the light. Based on the observed trend of how the I_{DS} decreases over time, extrapolation suggests > 37 % of charge retention can be obtained ten years after switching off the light. The observed rapid increase of I_{DS} during illumination and the subsequent exceptional charge retention ability after removing the illumination is coherent with mechanism proposed above, where vastly available hole traps, likely due to nitrogen-dopants, exist in N-doped CQDs serving to firmly immobilize photoexcited holes preventing them from recombination and leading to a long-lasting photo-gating effect (**Figure 4(c)**). While such a behaviour is somewhat similar to those reported on FET-based memories with a graphene active layer decorated by N-doped TiO₂ nanocrystals,¹⁰ the charge retention capability observed in the current N-doped CQD device is remarkable, maintaining ≥ 100 % of the programmed state (I_{DS}) for 7 hours after switching off the light. In order to probe whether nitrogen dopants are indeed the origins of the hole traps and the observed memory retention, another batch of CQDs were synthesized by the same method but without any nitrogen sources (EDA) added into the synthesis (named below as “non-doped CQDs”). Near identical device as mentioned-above was fabricated except that non-doped CQDs were applied to decorate the graphene in non-doped devices. The evolution of ΔI_{DS} over time of a non-doped device under UV illumination was monitored also by fixing V_G at 0 V and V_{DS} at 0.5 V. As shown in **Figure 4(b)**, the observed evolution exhibits a behaviour which is very different from that observed in N-doped CQD device. Notably, in non-doped CQD devices, the photocurrent decreases slowly down to less than 30 % of the highest level within only about a thousand seconds after switching off the light. In another word, in non-doped devices, the memory function in terms of charge retention, if existed, is rather poor resulting in a more than 70% of loss of programmed state within a thousand seconds (i.e. \sim half of an hour) after memory writing. Indeed, as mentioned above, CQDs synthesized by the current method have rich surface chemical groups. Even without nitrous carbon groups, in non-doped CQDs other surface groups and/or defects may also serve as traps for the photoexcited carriers leading to photoresponse also by the photo-gating effect. Likely charge trapping also happens in non-doped devices explaining the non-

instantaneous decay of the photoresponse after switching of the UV. Nevertheless, in the absence of deep traps capable to retain charges firmly, the photo-gating effect will progressively diminish after switching off the illumination due to carrier recombination (**Figure 4(d)**). The comparison of the photocurrent (ΔI_{DS}) evolution over time upon and after UV illumination between the N-doped and the non-doped CQD device confirms the vital role of N-dopants in terms of effective hole traps to provide a long-lasting non-volatile memory



function.

Figure 4: (a) The photoresponse to UV illumination ($\lambda = 365$ nm, $E_a = 0.7$ mW cm $^{-2}$) in terms of the change of source-drain current I_{DS} by comparison to I_{dark} of a graphene device decorated by N-doped CQDs. The dotted line represents the linear extrapolation of I_{DS} based on the trend observed. (b) The photoresponse to the same UV illumination as (a) of a graphene device decorated by non-doped-CQDs. The photocurrents shown in (a) and (b) were measured by fixing $V_G = 0$ V and $V_{DS} = 0.5$ V. (c) The schematic corresponding to the situation shown in (a) where holes are trapped and stored in N-doped CQDs (blue spheres) inducing more electrons in the graphene FET channel by the photo-gating effect. Red lines inside the bandgap represents hole traps likely due to the nitrogen dopants. (d) The schematic corresponding to the situation shown in (b) where non-doped CQDs were not able

to trap and storage firmly holes which recombines subsequently with the electrons in the graphene after UV illumination.

Coherent with the N-induced hole-trapping and photo-gating mechanisms proposed above, in N-doped CQD devices, the achieved memory after UV programming can be successfully erased by applying a positive gate voltage. **Figure 5(a)** exhibits a complete UV-writing and V_G -erasing cycle, where the I_{DS} of the device (measured at $V_G = 0$ V and $V_{DS} = 0.5$ V) was first increased to a high level thanks to a UV illumination ($\lambda = 365$ nm, $E_a = 0.7$ mW cm^{-2}) for a duration of 30 seconds. Then a positive gate voltage of +50 V was applied on the device for another duration of 30 seconds, which results in a drop of I_{DS} back to a level very close to its initial value before UV programming. The schematic proposing the erasing process is shown in **Figure 5(b)**. When a large positive gate voltage is applied onto the device, strong electron accumulation was resulted in the FET and the fermi level of the graphene was raised. This leads to a large amount of electrons being transferred back from the graphene to the N-doped CQDs to recombine with the trapped holes and thus to erase the programmed state.

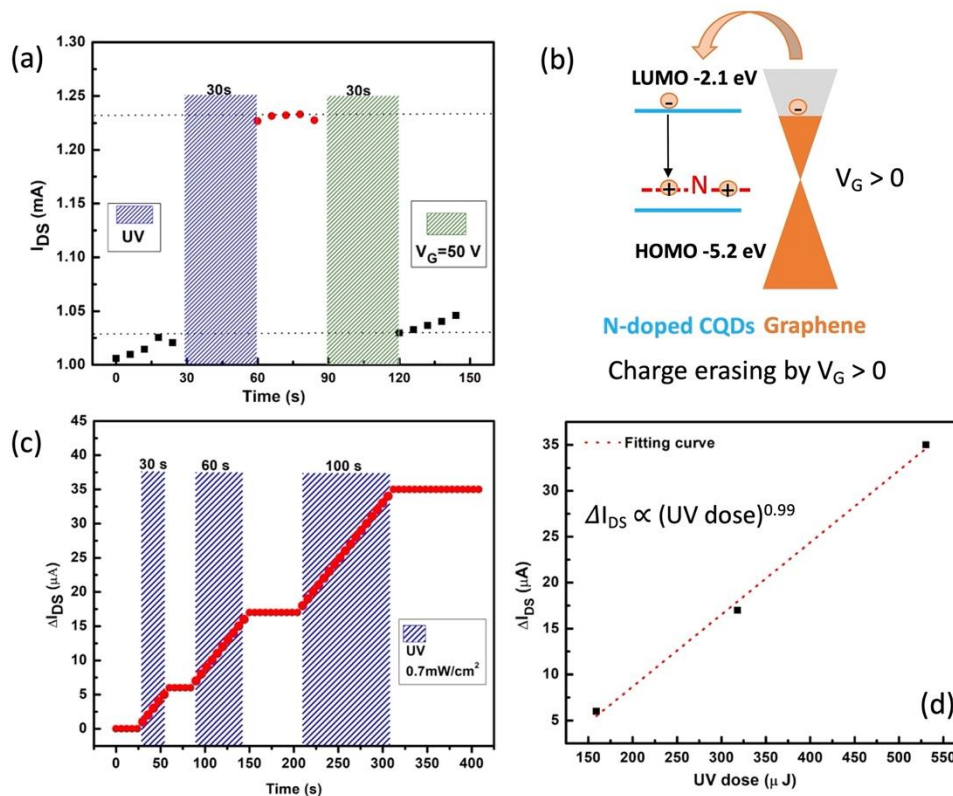


Figure 5: (a) The evolution of I_{DS} of a N-doped CQD device upon a 30-second UV ($\lambda = 365$ nm, $E_a = 0.7$ mW cm⁻²) programming and upon an erasing operation by the application of a +50 V gate voltage (V_G). (b) Schematic of the memory erasing mechanism on a N-doped CQD device when a positive gate voltage is applied. (c) Instant photocurrent response of the N-doped CQD device to UV illumination ($\lambda = 365$ nm, $E_a = 0.7$ mW cm⁻²) with different durations. Both The data shown in (a) and (c) were measured by setting $V_G = 0$ V and $V_{DS} = 0.5$ V. (d) The evolution of ΔI_{DS} over different incident UV doses extracted from (c). The red dotted line represents the numerical fitting.

Finally, by modifying the dose of the illumination, we demonstrate that multilevel memory retention can be achieved in the current N-doped CQD devices. As shown in **Figure 5(c)**, upon receiving three consecutive UV illuminations of the same irradiance (0.7 mW cm⁻²) but a different illumination duration, the device exhibits a stepwise increase of photocurrent (ΔI_{DS}). Such a distinctive multilevel writing capability can be potentially translated into memory applications for multi-bit information storage. Taking into account the illumination duration, the power density, and the active channel area of the device, one can calculate the illumination dose in the unit of joule. The dose information was then plotted together with the corresponding photocurrent shown in **Figure 5(d)**. A nearly linear relationship can be obtained between the measured photocurrent and the illumination dose, which is in agreement with the observed $\Delta V_{Dirac}-E_a$ behaviour shown in **Figure 2(d)** where the dose was modified by changing the power density of the illumination instead of duration.

5.4 Conclusion

FET-based non-volatile multilevel optoelectronic memory is demonstrated by coupling graphene transistors and colloidal N-doped CQDs. Due to the bandgap of the N-doped CQDs, the hybrid CQD/graphene memory devices are sensitive to UV photons such as those with a wavelength of 365 nm. Upon UV illumination, the photo-excited N-doped CQDs result in electron transfers from the CQDs to the graphene, leaving the photo-excited holes trapped behind by the nitrogen dopants in the N-doped CQDs. This leads to a prominent photo-gating effect and a *n*-type doping of the graphene FET. The observed long-lasting memory behaviour in these N-doped CQD devices likely originates from the vast and deep

hole traps provided by the N-dopants, as in non-doped CQD devices only poor charge retention capability was observed. Importantly, on N-doped CQD devices, multilevel memory functions are demonstrated by UV illumination with a controlled dose under a gate bias of 0 V. Upon UV programming, the I_{DS} of the device can be maintained at a high level (> 96 % of the I_{DS} value right after switching off the light) for ten hours after switching off the light. Such a memory function was further shown to be erasable by a positive gate bias, which induces strong electron accumulation in the graphene FET and the removal of hole-retention in CQDs through charge recombination. Taking into account the abundant availability of carbon elements, the facile solution synthesis routes and the demonstrated long-lasting non-volatile memory function, these fully carbon-based CQD/graphene devices provide interesting perspectives for the further development of transistor-based optoelectronic memories.

5.5 References:

1. Nonvolatile Memories— Materials, Devices and Applications. *Chemical & Engineering News Archive* **91**, 35 (2013).
2. Wulf, Wm. A. & McKee, S. A. Hitting the memory wall. *ACM SIGARCH Computer Architecture News* **23**, 20–24 (1995).
3. Han, S. T., Zhou, Y. & Roy, V. A. L. Towards the development of flexible non-volatile memories. *Advanced Materials* vol. 25 5425–5449 Preprint at <https://doi.org/10.1002/adma.201301361> (2013).
4. Grajower, M., Mazurski, N., Shappir, J. & Levy, U. Non-Volatile Silicon Photonics Using Nanoscale Flash Memory Technology. *Laser Photon Rev* **12**, 1700190 (2018).
5. Lv, Z. *et al.* Semiconductor Quantum Dots for Memories and Neuromorphic Computing Systems. *Chemical Reviews* vol. 120 3941–4006 Preprint at <https://doi.org/10.1021/acs.chemrev.9b00730> (2020).
6. Zhu, Z., Guo, Y. & Liu, Y. Application of organic field-effect transistors in memory. *Materials Chemistry Frontiers* vol. 4 2845–2862 Preprint at <https://doi.org/10.1039/d0qm00330a> (2020).

Chapter 5 N-Doped Carbon Quantum Dots on Graphene for Field-Effect Transistor Optoelectronic Memories

7. Star, A., Lu, Y., Bradley, K. & Grüner, G. Nanotube Optoelectronic Memory Devices. *Nano Lett* **4**, 1587–1591 (2004).
8. Yang, J., Choi, M. K., Kim, D.-H. & Hyeon, T. Designed Assembly and Integration of Colloidal Nanocrystals for Device Applications. *Advanced Materials* **28**, 1176–1207 (2016).
9. Liu, M. *et al.* Colloidal quantum dot electronics. *Nat Electron* **4**, 548–558 (2021).
10. Sun, Z., Li, J., Liu, C., Yang, S. & Yan, F. Trap-Assisted Charge Storage in Titania Nanocrystals toward Optoelectronic Nonvolatile Memory. *Nano Lett* **21**, 723–730 (2021).
11. Bakulin, A. A. *et al.* Charge trapping dynamics in pbs colloidal quantum dot photovoltaic devices. *ACS Nano* **7**, 8771–8779 (2013).
12. Han, S.-T. *et al.* CdSe/ZnS core–shell quantum dots charge trapping layer for flexible photonic memory. *J Mater Chem C Mater* **3**, 3173–3180 (2015).
13. Kumari, P., Ko, J., Rao, V. R., Mhaisalkar, S. & Leong, W. L. Non-Volatile Organic Transistor Memory Based on Black Phosphorus Quantum Dots as Charge Trapping Layer. *IEEE Electron Device Letters* **41**, 852–855 (2020).
14. Ambrosio, F., Meggiolaro, D., Mosconi, E. & de Angelis, F. Charge localization and trapping at surfaces in lead-iodide perovskites: the role of polarons and defects. *J Mater Chem A Mater* **8**, 6882–6892 (2020).
15. Jeong, Y. J., Yun, D.-J., Noh, S. H., Park, C. E. & Jang, J. Surface Modification of CdSe Quantum-Dot Floating Gates for Advancing Light-Erasable Organic Field-Effect Transistor Memories. *ACS Nano* **12**, 7701–7709 (2018).
16. Lin, Y., Li, G., Yu, P., Ercan, E. & Chen, W. Organic liquid crystals in optoelectronic device applications: <scp>Field-effect</scp> transistors, nonvolatile memory, and photovoltaics. *Journal of the Chinese Chemical Society* (2022) doi:10.1002/jccs.202200061.
17. Rios, C. *et al.* Integrated all-photonic non-volatile multi-level memory. *Nat Photonics* **9**, 725–732 (2015).
18. Yu, Y. *et al.* Small-Molecule-Based Organic Field-Effect Transistor for Nonvolatile Memory and Artificial Synapse. *Advanced Functional Materials* vol. 29 Preprint at <https://doi.org/10.1002/adfm.201904602> (2019).

Chapter 5 N-Doped Carbon Quantum Dots on Graphene for Field-Effect Transistor Optoelectronic Memories

19. Shao, L. *et al.* Optoelectronic Properties of Printed Photogating Carbon Nanotube Thin Film Transistors and Their Application for Light-Stimulated Neuromorphic Devices. *ACS Appl Mater Interfaces* **11**, 12161–12169 (2019).
20. Ling, H. *et al.* Electrolyte-gated transistors for synaptic electronics, neuromorphic computing, and adaptable biointerfacing. *Applied Physics Reviews* vol. 7 Preprint at <https://doi.org/10.1063/1.5122249> (2020).
21. Zhou, Y. *et al.* An upconverted photonic nonvolatile memory. *Nat Commun* **5**, 4720 (2014).
22. Wang, Y. *et al.* Photonic Synapses Based on Inorganic Perovskite Quantum Dots for Neuromorphic Computing. *Advanced Materials* **30**, (2018).
23. Sun, Z., Li, J., Liu, C., Yang, S. & Yan, F. Trap-Assisted Charge Storage in Titania Nanocrystals toward Optoelectronic Nonvolatile Memory. *Nano Lett* **21**, 723–730 (2021).
24. Guo, Y. *et al.* Multibit Storage of Organic Thin-Film Field-Effect Transistors. *Advanced Materials* **21**, 1954–1959 (2009).
25. Zhang, L. *et al.* Large-area, flexible imaging arrays constructed by light-charge organic memories. *Sci Rep* **3**, 1080 (2013).
26. Peng, L., Hu, L. & Fang, X. Low-Dimensional Nanostructure Ultraviolet Photodetectors. *Advanced Materials* **25**, 5321–5328 (2013).
27. Reckmeier, C. J., Schneider, J., Susha, A. S. & Rogach, A. L. Luminescent colloidal carbon dots: optical properties and effects of doping [Invited]. *Opt Express* **24**, A312 (2016).
28. Cao, L. *et al.* Carbon dots for energy conversion applications. *J Appl Phys* **125**, 220903 (2019).
29. Zhu, S. *et al.* Highly Photoluminescent Carbon Dots for Multicolor Patterning, Sensors, and Bioimaging. *Angewandte Chemie* **125**, 4045–4049 (2013).
30. Hu, X. *et al.* Green one-step synthesis of carbon quantum dots from orange peel for fluorescent detection of Escherichia coli in milk. *Food Chem* **339**, 127775 (2021).
31. Vyas, Y., Chundawat, P., Dharmendra, Punjabi, P. B. & Ameta, C. Green and Facile Synthesis of Luminescent CQDs from Pomegranate Peels and its Utilization in the Degradation of Azure B and Amido Black 10B by Decorating it on CuO Nanorods. *ChemistrySelect* **6**, 8566–8580 (2021).
32. Yuan, T. *et al.* Carbon quantum dots: an emerging material for optoelectronic applications. *J Mater Chem C Mater* **7**, 6820–6835 (2019).

Chapter 5 N-Doped Carbon Quantum Dots on Graphene for Field-Effect Transistor Optoelectronic Memories

33. Mintz, K. J., Zhou, Y. & Leblanc, R. M. Recent development of carbon quantum dots regarding their optical properties, photoluminescence mechanism, and core structure. *Nanoscale* **11**, 4634–4652 (2019).
34. Zhu, S. *et al.* Highly photoluminescent carbon dots for multicolor patterning, sensors, and bioimaging. *Angewandte Chemie - International Edition* **52**, 3953–3957 (2013).
35. Yan, F. *et al.* The fluorescence mechanism of carbon dots, and methods for tuning their emission color: a review. *Microchimica Acta* vol. 186 Preprint at <https://doi.org/10.1007/s00604-019-3688-y> (2019).
36. Gomez, I. J., Arnaiz, B., Cacioppo, M., Arcudi, F. & Prato, M. Nitrogen-doped carbon nanodots for bioimaging and delivery of paclitaxel. *J Mater Chem B* **6**, 5540–5548 (2018).
37. Nair, A., Haponiuk, J. T., Thomas, S. & Gopi, S. Natural carbon-based quantum dots and their applications in drug delivery: A review. *Biomedicine & Pharmacotherapy* **132**, 110834 (2020).
38. Zhang, W. *et al.* Carbon-dot-modified TiO_{2-x} mesoporous single crystals with enhanced photocatalytic activity for degradation of phenol. *Research on Chemical Intermediates* **44**, 4797–4807 (2018).
39. Huang, P. *et al.* Carbon quantum dots improving photovoltaic performance of CdS quantum dot-sensitized solar cells. *Opt Mater (Amst)* **110**, 110535 (2020).
40. Wang, S., Zhu, Y., Liu, B., Wang, C. & Ma, R. Introduction of carbon nanodots into SnO₂ electron transport layer for efficient and UV stable planar perovskite solar cells. *J Mater Chem A Mater* **7**, 5353–5362 (2019).
41. Li, Z. *et al.* Efficient perovskite solar cells enabled by ion-modulated grain boundary passivation with a fill factor exceeding 84%. *J Mater Chem A Mater* **7**, 22359–22365 (2019).
42. Zhang, W., Guo, X., Yin, J. & Yang, J. Organic Field-Effect Transistor Memory Device Based on an Integrated Carbon Quantum Dots/Polyvinyl Pyrrolidone Hybrid Nanolayer. *Electronics (Basel)* **9**, 753 (2020).
43. Suk, J. W. *et al.* Transfer of CVD-grown monolayer graphene onto arbitrary substrates. *ACS Nano* **5**, 6916–6924 (2011).
44. Li, H., Kang, Z., Liu, Y. & Lee, S.-T. Carbon nanodots: synthesis, properties and applications. *J Mater Chem* **22**, 24230 (2012).

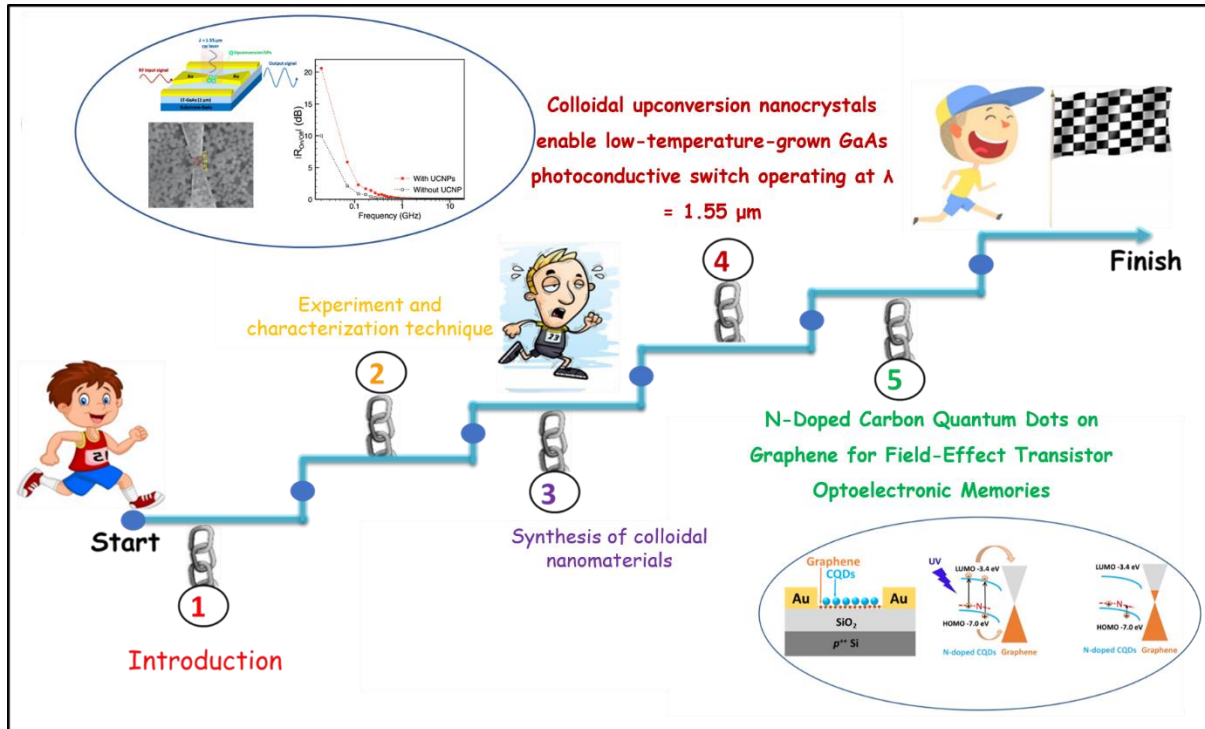
Chapter 5 N-Doped Carbon Quantum Dots on Graphene for Field-Effect Transistor Optoelectronic Memories

45. Ming, H. *et al.* Large scale electrochemical synthesis of high quality carbon nanodots and their photocatalytic property. *Dalton Transactions* **41**, 9526 (2012).
46. Kwon, W., Do, S., Kim, J.-H., Seok Jeong, M. & Rhee, S.-W. Control of Photoluminescence of Carbon Nanodots via Surface Functionalization using Para-substituted Anilines. *Sci Rep* **5**, 12604 (2015).
47. Permatasari, F. A., Aimon, A. H., Iskandar, F., Ogi, T. & Okuyama, K. Role of C–N Configurations in the Photoluminescence of Graphene Quantum Dots Synthesized by a Hydrothermal Route. *Sci Rep* **6**, 21042 (2016).
48. Wen, J., Yan, C. & Sun, Z. The Application of a High- κ Polymer Dielectric in Graphene Transistors. *Adv Electron Mater* **6**, 2000031 (2020).
49. Fang, H. & Hu, W. Photogating in Low Dimensional Photodetectors. *Advanced Science* **4**, 1700323 (2017).
50. Sun, Z. *et al.* Infrared Photodetectors Based on CVD-Grown Graphene and PbS Quantum Dots with Ultrahigh Responsivity. *Advanced Materials* **24**, 5878–5883 (2012).
51. Sun, Z. *et al.* Infrared photodetectors based on CVD-grown graphene and PbS quantum dots with ultrahigh responsivity. *Advanced Materials* **24**, 5878–5883 (2012).
52. Serhan, M. *et al.* Total iron measurement in human serum with a smartphone. in *AIChE Annual Meeting, Conference Proceedings* vols 2019-November (American Institute of Chemical Engineers, 2019).
53. Zhou, G., Li, Z., Ge, Y., Zhang, H. & Sun, Z. A self-encapsulated broadband phototransistor based on a hybrid of graphene and black phosphorus nanosheets. *Nanoscale Adv* **2**, 1059–1065 (2020).
54. Li, D. *et al.* Near-Infrared Excitation/Emission and Multiphoton-Induced Fluorescence of Carbon Dots. *Advanced Materials* **30**, (2018).
55. Jiang, L. *et al.* UV–Vis–NIR Full-Range Responsive Carbon Dots with Large Multiphoton Absorption Cross Sections and Deep-Red Fluorescence at Nucleoli and In Vivo. *Small* **16**, (2020).
56. Nazri, N. A. A., Azeman, N. H., Luo, Y. & A Bakar, A. A. Carbon quantum dots for optical sensor applications: A review. *Optics and Laser Technology* vol. 139 Preprint at <https://doi.org/10.1016/j.optlastec.2021.106928> (2021).

Chapter 5 N-Doped Carbon Quantum Dots on Graphene for Field-Effect Transistor
Optoelectronic Memories

Chapter 6

Conclusion and Perspective



My thesis research examined the current state of optoelectronic devices and their technological prospects, demonstrating the potential of solution-processed nanocrystals in next-generation optoelectronic applications such as microwave photoconductive switches and optical memories.

In my project, I used two types of colloidal nanocrystals for this purpose: 1) Colloidal NaYF₄:Er³⁺ upconversion nanocrystals solution-processed exhibit sensitivity to SWIR photons with wavelengths of 1.5 μm ; 2) luminescent carbon quantum dots (CQDs) and CDs exhibit charge trapping abilities in the UV range at 365 nm.

To achieve microwave photoconductive switches that function at $\lambda = 1.55 \mu\text{m}$ illumination, an alternative approach was devised by depositing solution-processed colloidal upconversion nanocrystals directly onto LT-GaAs. The SEM image of device with upconversion nanocrystals shows hybrid device contain a mono- to bi-layers of nanocrystals. To that end, Er³⁺-doped NaYF₄ nanocrystals were synthesized via colloidal routes, yielding uniform

morphologies and dimensions as well as a pure hexagonal β -NaYF₄ phase. Five strong fluorescence peaks were observed on these nano-crystals under $\lambda = 1.55 \mu\text{m}$ laser excitation, with their peak intensity located at wavelengths of = 525 nm, 544 nm, 658 nm, 806 nm, and 979 nm, respectively, among which the first four fluorescence emission peaks can overlap largely with the optical absorption of LT-GaAs, indicating efficient resonance energy transfer. After that, a hybrid Er³⁺-doped NaYF₄ nanocrystal/LT-GaAs photoconductive switch was created, with four Er³⁺-doped NaYF₄ nanocrystals located inside the photoconductive switch gap and in direct contact with LT-GaAs. As the theoretical Förster resonance energy transfer rate decays rapidly ($\propto 1/r^6$, r = distance) over the distance between the (energy) donor and the acceptor. Here, we therefore estimate that the four bottom layer nanocrystals are the main agents responsible for optical absorption and energy transfer to the LT-GaAs underneath upon $\lambda = 1.55 \mu\text{m}$ photoexcitation. Under CW = 1.55 μm laser illumination (power density 12.9 mW m⁻²) a significant increase in the ON/OFF ratio was observed in the upconversion nanocrystal/LT-GaAs hybrid device due to the upconversion energy transfer from the nanocrystals. At an input signal frequency of 20 MHz, the hybrid device achieved a maximum ON/OFF ratio of 20.6 dB. Comparison between the control device without UCNPs and device with UCNPs was measured and shows the ON/OFF ratio was more than 2-fold higher in decibels (or more than 11-fold higher in absolute value) for hybrid device with UCNPs. The current Er³⁺-doped NaYF₄ nanocrystal/LT-GaAs photoconductive switch by photon upconversion represents a novel solution-processed path to achieve optical control of microwave signals by = 1.55 μm illumination.

Secondly, the N-doped carbon dots has been used to make FET-based non-volatile multilevel optoelectronic memory by using graphene as charge transport layer in transistors and colloidal N-doped CQDs as photoresponsive/charge trapping layer under UV illumination. The hybrid CQD/graphene memory devices are sensitive to UV photons with a wavelength of 365 nm due to the bandgap of the N-doped CQDs. Optical properties can be harvested by illuminating UV that causes electron transfers from photo-excited N-doped CQDs to graphene, leaving photo-excited holes trapped behind by the nitrogen dopants in the N-doped CQDs. The mechanism of forming a non-volatile memory can be explained by this prominent photo-gating effect where holes were trapped in N-doped CDs and making graphene FET n-type. The observed long-lasting memory behaviour in these N-doped CQD

devices is most likely due to the vast and deep hole traps provided by the N-dopants because of surface states and functional groups formed during synthesis of N-doped CDs, as only poor charge retention capability was observed in non-doped CQD devices. Importantly, multilevel memory functions on N-doped CQD devices were demonstrated using UV illumination with a controlled dose (power density 0.7 Mw/cm^2) and a gate bias of 0 V. After UV programming, the device's photocurrent (I_{DS}) can be kept at a high level ($> 96\%$ of the I_{DS} value obtained immediately after turning off the light) for ten hours. To further delete the memory a positive gate bias was applied, which induces strong electron accumulation in the graphene FET and the removal of hole retention in CQDs via charge recombination and erase the memory function. Given the abundance of carbon elements, the ease of solution synthesis, and the demonstrated long-lasting non-volatile memory function, these fully carbon-based CQD/graphene devices offer promising prospects for the future development of transistor-based optoelectronic memories.

Perspective

Here, we also give some ideas on future development for these hybrid devices. In terms of the perspective to further improve the performance of these $\text{NaY}_4:\text{Er}^{3+}/\text{LT-GaAs}$ based devices, possible direction includes using plasmonic nanomaterials which is very trending materials used to harvest energy in SWIR spectrum range to make microwave photoconductive switch working at $\lambda = 1.5 \text{ }\mu\text{m}$. Plasmonic or Au NRs have enormous absorption and field enhancement, focus light in gap and enhance the performance. Possible directions for improvement can include improving the quantum yield of UCNPs by surface modification and looking for more efficient light absorber example gold nanorods.

Secondly, Emerging non-volatile optical memory technologies are promising candidates for near-/in-memory computing applications to overcome memory walls and improve computing system performance. For that different semiconductor nanocrystals can be studied further by tuning their band gap and enhancing their absorption intensity.

Optical memories can also be formed in different optical windows of EM spectrum from UV-Vis to Infrared wavelength. We can also use the same coupling of device to create flexible memory because graphene is flexible and CDs did not produce continuous film.

APPENDIX

Optical Characterizations of CDs

Different batches of CDs have synthesized by using different dopant materials and modifying them by different solvent. The aim here to get CDs that absorb SWIR wave i.e., 1.2 μm to 1.5 μm and give emission in visible range.

Figure 1 shows the UV-Vis absorption and states different absorption because of creation of different surface groups, functionalization of CDs metallic and non-metallic. (b) shows emission in visible range upon excitation with 365 nm laser source. No emission spectrum observed with 1.3 and 1.5 μm light source.

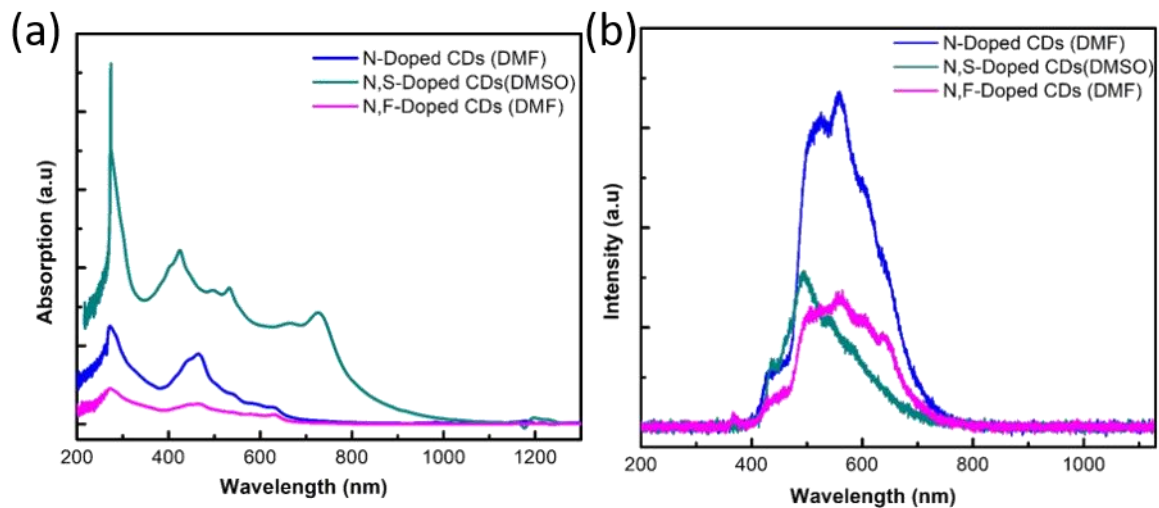


Figure 1: UV-Vis absorption spectrum and (b) Photoluminescence spectrum of N, N,S and N,F doped CDs.

Further modification has also been done to achieve to SWIR absorption of CDs. The following **figure 2** shows the UV-Vis and absorption and PL of solvent modified and doped CDs.

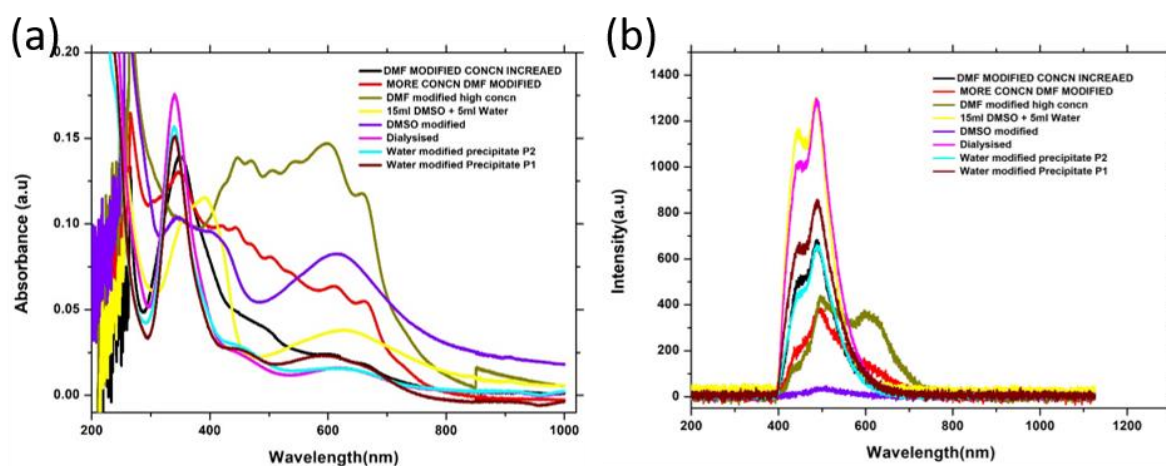


Figure 2: UV-Vis and (b) PL of modified CDs.

Table 1: Precursors used for Carbon Dots synthesis, QY

Carbon source	Nitrogen source	solvent	Time/Temperature	QY	Purification
Citric acid	EDA(ethylenediamine)	Water	6H/160°C	29.5%	Dialysis
Citric acid	Urea	DMF	6H/160°C	13%	Centrifuge, dialysis, filtration
Citric acid	Urea	Water	24H/160°C		Centrifuge, dialysis
Citric acid	Urea	DMF	24H/160°C		Centrifuge
Modified sample	Modification solvents		QY		
Citric acid/ Urea/DMF	DMF(Dimethylformamide)		17%(P1) DMF		
	WATER		7%(P2) WATER		
	DMF increased concentration		8% (P2)DMF		
Citric acid/urea/water	DMSO+ Water (Dimethyl sulfoxide)		7.5%(P1)		
	DMF		7%(PPT3) DMF		
	Water modified		10%(ppt3)		
	Water(Dialysis)		14%(P1)		

RÉSUMÉ

L'optoélectronique est un domaine technologique en croissance rapide qui implique l'utilisation d'appareils électroniques pour générer, détecter et contrôler la lumière. Ces dispositifs peuvent être utilisés dans une variété d'applications telles que les commutateurs photoconducteurs, les systèmes de contrôle d'accès automatique, les télécommunications, la mémoire et bien d'autres. Parce qu'il s'agit d'un domaine si vaste, la variété des dispositifs qui relèvent de l'optoélectronique est vaste. Dans ce Thèse de doctorat, Je suis particulièrement intéressé dans traitable en solution nanomatériaux colloïdaux qui peuvent permettre les interactions lumière-matière. Pour commencer, je me suis d'abord concentré sur la synthèse colloïdale. La travailler sur cette partie rendements deux types différents de nanocristaux colloïdaux : (1) NaYF₄ dopé Er³⁺ nanocristaux, capables d'absorberait up-converti photons infrarouges à ondes courtes tels que ceux avec $\lambda = 1,5 \mu\text{m}$ aux photons visibles ; (2) points quantiques de carbone (CQD) avec dopage à l'azote, capable d'absorber les photons UV et les rétrograder en visible fluorescence. Dès l'obtention du résultat souhaité colloïdal nanocristaux aux propriétés optiques adaptées, j'ai ensuite les a appliqués dans deux types de dispositifs optoélectroniques : (i) Commutateurs thermo conducteurs, qui permettent un contrôle optique de l'amplitude et de la phase des signaux micro-ondes à transmettre. Pour obtenir des commutateurs photoconducteurs micro-ondes fonctionnels à $\lambda = 1,55 \mu\text{m}$ éclairage, le NaYF₄ dopé Er³⁺ mentionné ci-dessus nanocristaux de conversion ascendante étaient déposé directement sur l'arséniure de gallium cultivé à basse température (LT-GaAs) pour réaliser des interrupteurs photoconducteurs. Les propriétés de ces appareils ont ensuite été caractérisé. Grâce aux propriétés d'upconversion des photons de ces nanocristaux, l'exposition sur les interrupteurs photoconducteurs hybrides un Rapport marche/arrêt plus de 2 fois plus élevé en décibels que l'appareil de commande sans nanocristaux appliqué. (ii) Effet de champ mémoires optoélectroniques à base de transistors (FET). Dans ce champ, le support de stockage de charge joue un rôle critique Aude la mémoire performance. Dans cette partie, j'exploite les propriétés uniques de piégeage et de rétention de charge de le sus mentionnées CQD colloïdaux dopés à l'azote (dopé N) pour réaliser des mémoires optoélectroniques fonctionnelles programmables par illumination UV et avec une possibilité d'écriture à plusieurs niveaux. En particulier, une fonction de mémoire de longue durée peut être obtenue grâce aux vastes sites de piégeage de trous fournis par ces CQD et à l'effet de photo-gating qui en résulte. Exerciez sur le graphène FET, tandis que l'effacement de la mémoire peut être réalisé via une polarisation de grille positive qui fournit suffisamment de porteurs pour la recombinaison de charge. Le résultat de cette thèse de doctorat points forts les contrôles techniques et chimiques pour obtenir haute performance dispositifs optoélectroniques tels que micro-ondes commutateurs photoconducteurs et mémoires optoélectroniques à base de FET non volatiles tout carbone par manipulation et récolte la propriétés optiques et électroniques des nanomatériaux colloïdaux.

MOTS CLÉS

Commutateurs photoconducteurs, commutation micro-ondes, conversion ascendante, nanocristaux colloïdaux, mémoires non volatiles, points de carbone, stockage de charge.

ABSTRACT

Optoelectronics is a rapidly growing technology field that involves the use of electronic devices to source, detect, and control light. These devices can be used in a variety of applications such as photoconductive switches, automatic access control systems, telecommunications, memory, and many others. Because this is such a broad field, the variety of devices that fall under optoelectronics is vast. In this, PhD thesis, I am particularly interested in solution processed colloidal nanomaterials that can allow light-matter interaction. To begin, I first focused on colloidal synthesis. The work on this part yields two different types of colloidal nanocrystals: (1) Er³⁺-doped NaYF₄ nanocrystals, capable to absorb and up-convert short-wave infrared photons such as those with $\lambda = 1.5 \mu\text{m}$ to visible photons; (2) carbon quantum dots (CQDs) with nitrogen-doping, capable to absorb UV photons and down-shift them into visible fluorescence. Upon obtaining the desired colloidal nanocrystals with suitable optical properties, I subsequently applied them into two type of optoelectronic devices: Photoconductive switches, which allow optical control over the magnitude and phase of microwave signals to be transmitted. To achieve microwave photoconductive switches functional at $\lambda = 1.55 \mu\text{m}$ illumination, the above-mentioned Er³⁺-doped NaYF₄ upconversion nanocrystals were deposited directly onto low-temperature-grown gallium arsenide (LT-GaAs) to achieve photoconductive switches. The properties of these devices were then characterized. Thanks to the photon upconversion properties of these nanocrystals, the hybrid photoconductive switch exhibits an ON/OFF ratio more than 2-fold higher in decibels than the control device without nanocrystals applied. (ii) Field-effect transistor (FET)-based optoelectronic memories. In this field, the charge storage medium plays a critical role to the memory's performance. In this part, I harnessed the unique charge-trapping and charge-retention properties of the above-mentioned colloidal nitrogen-doped (N-doped) CQDs to achieve functional optoelectronic memories programmable by UV illumination and with a multilevel writing possibility. In particular, a long-lasting memory function can be achieved thanks to the vast hole trapping sites provided by these CQDs and the resultant photo-gating effect exercised on the graphene FET, while memory erasing can be achieved via a positive gate bias that provides sufficient carriers for charge recombination. The result of this PhD thesis highlights the engineering and chemical controls to obtain high-performance optoelectronic devices such as microwave photoconductive switches and all-carbon non-volatile FET-based optoelectronic memories through manipulating and harvesting the optical and electronic properties of colloidal nanomaterials.

KEYWORDS

Photoconductive switches, microwave switching, upconversion, colloidal nanocrystals, non-volatile memories, Carbon dots, charge storage.